

# STM and RAIRS on thermal activation of mesityl-porphyrins deposited on corrugated copper

Thesis submitted in accordance with the requirements of the University of Liverpool  
for the degree of Doctor in Philosophy by

Gerardus Emanuel in 't Veld, M.Sc.

August 16, 2010

;

*“for my grandparents”*



## Abstract

The properties and functions of both living and anthropogenic systems are defined within the first level of organisation of atoms and molecules and therefore holds many promise for fundamentally new applications. Examples of this are chemical manufacturing using designed molecular assemblies, molecular memories and processing of information using photons or electron spin and molecular sensors. By means of the complementary surface science techniques STM and RAIRS adsorption of organic molecules on a metal substrate was investigated. 2,4,6-trimethyl-5,10,15,20-tetraphenyl-porphyrin (TM-TPP) and its cobalt metallated equivalent (TM-Co-TPP) independently deposited on corrugated Cu(110) exhibit an exceptional interplay with the substrate. The adsorption process at 298 K consists of multiple stages. Both molecules adsorb via a precursor gas phase achiral planar geometry, and reconfigure to an achiral saddled shape upon surface contact. Small self-assembled chiral domains build by mesitylic  $\pi$ - $\pi$  interactions exist for TM-Co-TPP. The four trimethyl-phenyl groups act as molecular shovels inducing substrate rearrangements dependent on the initial surface temperature and coverage. At elevated temperatures copper absorption yields chiral TM-Cu-TPP for TM-TPP, and porphyrinic pyrrole groups react with *ortho* mesitylic methyl groups for both TPPs. The heating range investigated runs from 298 K to 500 K at which decomposition occurs. It shows various phases that ultimately create copper catalysed *para* methyl mediated covalent attachment of multiple molecules to small networks and branched chains. Co-deposition of glucoside methyl- $\alpha$ -D-glucopyranoside (MDG) and TM-TPP at similar substrate conditions result in different nanostructure formation. Not only covalent attachment of MDG molecules to both mesityl *ortho* and *para* methyl groups, but also multiple sugar linkage was observed.

## Acknowledgements

The research presented in this theses was carried out as part of the European Marie Curie CHEXTAN (CHiral EXpression and Transfer At the Nanoscale) Network, that aimed at probing and understanding chiral interactions at the nanoscale. It would not have been possible without the help of many people, therefore I would like to thank everybody who made a valuable contribution. I am, however, specially indebted to a few people. First of all my Professor Rasmita Raval for giving me the opportunity to do a Ph.D. in a very interesting research area. For the useful advice while on the trajectory and the continues support during the tough moments. Furthermore Dr. Sam Haq for his excellent knowledge on UHV systems and RAIRS, Dr. Ning Liu from whom I learned a lot on performing STM experiments. CHEXTAN Project Leader Dr. David Amabilino and Dr. Patrizia Iavicoli from the ICMAB in Barcelona for providing special molecules and Dr. Matthew Dyer for providing theoretical calculations. Moreover I would like to specially thank Dr. Bohlmeijer for very valuable conversations that kept me on track and helped reshape myself during difficult periods. Finally I would like to thank my parents and brother who were always there.

The work was supported by the UK Research Councils(EPSRC, BBSRC), the DGI (Spain), under the project CTQ2006-06333/BQU, the DGR (Catalonia, Project 2005 SGR-00591), and the Marie Curie FP6 Research Training Network CHEXTAN (MRTN-CT-2004-512161).

# Abbreviations

$\chi$	ring torsion
$\delta$	in plane bending
$\nu$	ip skeletal modes
$\phi$	ip modes $\parallel$ with respect to the mesityl- $C_{meso}$ bond
$\pi$	ip modes $\perp$ with respect to the mesityl- $C_{meso}$ bond
$\Psi$	oop modes $\perp$ with respect to the mesityl- $C_{meso}$ bond
$\sigma$	oop modes $\parallel$ with respect to the mesityl- $C_{meso}$ bond
[110]	$[110] \equiv [1\bar{1}0]$
AO	Atomic Orbital
as	asymmetric
b	bend
Bre	breathing
def	deformation
DFT-SQM	Density Functional Theory-Scaled Quantum Mechanical
DMF	dimethylformamide
dom	domed
f	fold
FBP	Free-Base Porphyrin
HB-HPB	hexa- <i>t</i> -butyl-hexaphenylbenzene
HF	Hartree-Fock
HOMO	Highest Occupied Molecular Orbital
hr	half ring

---

HT-STM	High Temperature STM
HtBDC	hexa-tert-butyl-decacyclene
ip	in-plane
LDI-TOF	Laser Desorption–Ionisation Time-Of Flight
LDOS	Local Density Of States
LEED	Low Energy Electron Diffraction
LUMO	Lowest Unoccupied Molecular Orbital
MDG	methyl- $\alpha$ -D-Glucopyranoside
MO	Molecular Orbital
mOH-TPP	4(meta)-hydroxy-5,10,15,20-tetraphenyl-porphyrin
MP	metal-porphyrin
MP2	Møller-Plesset second-order perturbation
oop	out-of-plane
P	Porphyrin
Pc	Phthalocyanine
Ph	phenyl
pOH-TPP	3(para)-hydroxy-5,10,15,20-tetraphenyl-porphyrin
Pro	propellering
Py	pyrrole
QCISD	Quadratic CI method with single and double substitutions
qr	quarter ring
RAIRS	Reflection Absorption Infra Red Spectroscopy
Rot	rotating
RT	2.5kJmol <sup>-1</sup> (Room Temperature)
ruf	ruffled
s	symmetric

sad	saddled
sh	shoulder
SOMO	Single Occupied Molecular Orbital
STM	Scanning Tunneling Microscopy
Str	stretching
TB	tertiary butyl
TBA	3,3',5,5'-tetra-tert-butyl-azobenzene
TBPP	tetra-3,5-di-t-butyl-phenyl porphyrin
TC	Thermocouple
TDDFT	Time Dependent Density Functional theory
TM-TPP	2,4,6-trimethyl-5,10,15,20-tetraphenyl-porphyrin
Trn	translation
TS	Transition State
TSP	Titanium Sublimation Pump
UHV	Ultra High Vacuum
var	variable
VASP	Vienna Ab-initio Simulation Package
VdW	Van der Waals
wav	waved
ZPVE	Zero-Point Vibrational Energies



**Figure 1.** – Colourcode STM images. The top colourbar can be applied to all STM images except Figure 5.1a, Figure 5.14, Figure 5.15, Figure 5.16, Figure 7.2 and Figure 7.1 for which the bottom colourbar needs to be applied. Figure 5.12a was obtained with a special tip state and Figure 6.2b is an image overlay.



# Contents

<b>Abbreviations</b>	<b>v</b>
<b>1. Introduction</b>	<b>4</b>
1.1. Porphyrins: electronic structure . . . . .	8
1.2. Porphyrin conformation, <i>meso</i> -phenyl-core coupling . . . . .	14
<b>2. Gas Adsorption on Solid Surfaces</b>	<b>19</b>
2.1. Adsorption Types . . . . .	19
2.2. Adsorbate surface mobility . . . . .	21
2.3. Lateral interactions . . . . .	24
2.4. Adsorption kinetics . . . . .	25
2.5. Temperature programmed desorption . . . . .	27
<b>3. Experimental techniques</b>	<b>29</b>
3.1. Scanning Tunneling Microscopy . . . . .	29
3.2. STM - History of Development . . . . .	37
3.2.1. Tubular Scanners . . . . .	39
3.3. InfraRed Spectroscopy . . . . .	42
3.4. Reflection Absorption Infra Red Spectrometry . . . . .	45
3.5. RAIRS - History of Development . . . . .	49
3.6. Experimental Setup . . . . .	53
3.6.1. Doser Setup, Sample, Crystal and Crystal Preparation . . . . .	57
<b>4. Adsorption of TM-TPP on Cu(110) at 298K</b>	<b>59</b>
4.1. RAIRS . . . . .	61
4.2. STM . . . . .	69
<b>5. Thermal activation of TM-TPP on Cu(110)</b>	<b>72</b>
5.1. Intermediate Activation: STM . . . . .	73
5.2. Intermediate: substrate-molecule interaction . . . . .	81

---

5.3. Maximised activation: STM . . . . .	83
5.4. Maximised activation: RAIRS . . . . .	91
5.5. Model of covalently linked TM-Cu-TPP on Cu(110) . . . . .	94
<b>6. Adsorption of TM-Co-TPP on Cu(110) at 298K</b>	<b>96</b>
6.1. STM . . . . .	96
6.2. RAIRS . . . . .	104
6.3. Model of TM-Co-TPP on Cu(110) . . . . .	105
<b>7. Thermal activation of TM-Co-TPP on Cu(110)</b>	<b>108</b>
7.1. Intermediate activation: STM . . . . .	108
7.2. Maximised activation: STM . . . . .	113
7.3. Model of covalently linked TM-Co-TPP on Cu(110) . . . . .	115
<b>8. Co-deposition of methyl-<math>\alpha</math>-D-Glucopyranoside and TM-TPP</b>	<b>117</b>
<b>9. Conclusions</b>	<b>120</b>
<b>A. Saddled TM-TPP Orbital configuration</b>	<b>122</b>
<b>B. Local coordinates skeletal modes of (metallo)porhyrins</b>	<b>124</b>
<b>C. RAIRS mesitylene</b>	<b>125</b>
<b>D. LDI-TOF MS TM-TPP in positive mode</b>	<b>127</b>
<b>E. VASP-DFT Molecular Orbitals TM-(Cu)-TPP</b>	<b>129</b>
<b>F. VASP-DFT Molecular Orbitals TM-(Co)-TPP minority spins</b>	<b>131</b>
<b>G. VASP-DFT Molecular Orbitals TM-(Co)-TPP majority spins</b>	<b>133</b>
<b>Bibliography</b>	<b>135</b>

# Chapter 1.

## Introduction

*“The only reason for time is so that everything doesn’t happen at once.”*

— Albert Einstein

Surface Science studies the processes that occur at surfaces at the nanoscale i.e. at the atomic and molecular level.<sup>[1]</sup> Therefore it is classified within Nanotechnology, which is defined by<sup>[2]</sup> the ability to understand, control, and manipulate matter at the level of individual atoms, molecules and clusters of molecules (supramolecular) in the range from 0.1 to 100nm. The properties and functions of both living and anthropogenic systems are defined within the first level of organisation of atoms and molecules and therefore holds many promise for fundamentally new applications. Examples of this are chemical manufacturing using designed molecular assemblies, molecular memories and processing of information using photons or electron spin, molecular sensors, detection and treatment of chronic illness by subcellular interventions, regenerating tissue and nerves, enhancing learning and other cognitive processes. Therefore the control of matter at nanoscale surfaces is of much wider relevance.

Traditionally surface science was based on understanding heterogeneous catalytic reactions. One of the most successful examples is the Haber-Bosch process in which an alkali-metal-promoted iron catalyst is used to adsorb  $N_2$ . It was found that (111) and (211) surface structures increase the rate for the synthesis of ammonia by a factor 500 over the (110) surface. A more recent contribution is the three-way catalyst based on Pt, Pd, and Rh to convert the noxious ( $NO_x$ , CO) exhaust gases created by every vehicle.<sup>[3]</sup>



Whereas initially surface science studies concentrated on relatively small molecules comprised of two to three atoms, more recently the understanding of adsorption of complex organic molecules at metal surfaces has found interest. An example of this is the introduction of chirality to a metal surface, and hence the creation of a selectivity function. Adsorption and self-assembly of tartaric acid, which is chiral, controls the handedness of the substrate, which makes it possible to create active sites for heterogeneous enantioselective reactions.<sup>[4]</sup> It, however, also serves a fundamental understanding of self-assembling processes that are observed frequently when more complex organic molecules interact with metal substrates i.e. molecule-molecule and surface-molecule interactions.

Also heterogeneous phenomena in atmospheric and interstellar chemistry are in the domain of surface science. The most abundant molecule in the universe, molecular hydrogen, is thought to have been formed on the surfaces of grains and dust particles. In addition to this many other molecules<sup>[5]</sup> have been detected in outer space.

The universe and life are emerged in chirality. From spiral galaxies, to the chiral amino-acids that are the building blocks of life on Earth. Other molecules of biological importance are the nucleotides that can be obtained from RNA or DNA, which all contain 2-deoxy-D-ribose as the sugar component and purines (Adenine, Guanine) or pyrimidines (Cytosine, Thymine, Uracil) as their heterocyclic bases.<sup>[6]</sup> In addition to this life could not have emerged without tetrapyrroles or porphyrins. Without these oxygen transport (haem), electron transport (cytochrome C) and photosynthesis (Chlorophyll a/b) would be non-existent.<sup>[7]</sup> The adsorption properties of specially selected molecules (Figure 1.1b) from the last group are the main subject in this thesis. Finally co-deposition of a glucoside (methyl- $\alpha$ -D-Glucopyranoside) is discussed.

The existence of these special pigments was already known at the start of 1800 when Pelletier and Caventou<sup>[9]</sup> called the pigment responsible for the green color of leaves: chlorophyll (Greek: chloros  $\rightarrow$  green and phyllon  $\rightarrow$  leaf). In 1844 Mulder executed mass determinations and perceived color differences on chlorophyll and proposed that it should be ranked amongst the indigo type compounds.<sup>[10]</sup> Later in 1896 Nencki established that porphyrins consist of pyrrole nuclei and he also proposed that the similar chemical properties of hemin and chlorophyll denote a common origin of flora and fauna. This provides insight into chemical and organismal evolution.<sup>[11]</sup> Part of the structure of chlorophyll was solved in 1913 when Küster proposed a correct formula for the ring system of porphyrins (Figure 1.1a).<sup>[12]</sup> The complete structure of chlorophyll a and haem

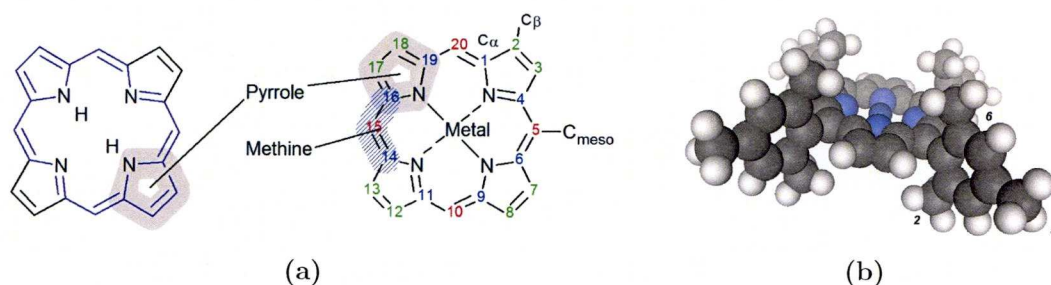


**Figure 1.1.** – a) The most simple porphyrin. On the left a free-base porphine that consists of four pyrrole rings that are linked together by four methine bridges to form a macrocycle, generally porphyrins are substituted on the eight  $\beta$  and/or the four meso positions. The two inner hydrogens alternate between the nitrogens, in which the trans conformation has a higher preference above the cis.<sup>[8]</sup> On the right a metal-porphine in which the hydrogens are substituted by a transition metal e.g. Fe, Cu, Co. b) space-filled model of planar 2,4,6-trimethyl-5,10,15,20-tetraphenyl(-Cobalt)-porphyrin

were worked out by Fischer and his coworkers<sup>[13]</sup>, who also were capable of synthesising porphines in the late 1920s.<sup>[14]</sup>

Due to the enormous importance of porphyrins in life and their potential applications in artificial devices<sup>[15–17]</sup>, these type of molecules have found an ever growing interest in different research areas. Many research groups have studied the interaction of different porphyrins on surfaces of which tetraphenylporphyrins (TPP) have been most widely studied. Substituted derivatives of TPP first found interest in 1996, when Jung *et al.*<sup>[18]</sup> performed controlled room-temperature positioning of individual porphyrin molecules on Cu(100). These Cu-TBPP molecules contain bulky tertiary butyl groups at the phenyl meta-positions. By deposition on a surface these groups separate the porphyrin core from the surface i.e. the surface is electronically decoupled. This was the start of the ongoing interest in the behaviour of relatively big molecules on different surfaces. In 1997 Gimzewski *et al.*<sup>[19–21]</sup>, who was also one of the researchers in the first study of TBPP, reported four different conformations of Cu-TBPP on three different substrates, Au(110), Ag(110) and Cu(100).

Three years later Mashiko *et al.* continued the analysis of this molecule by STM induced photo-emission<sup>[22]</sup> on the same surface and extended this by investigating the influence of different groups (carboxy, vinyl and cyano) replacing selected TB-groups on free base-TBP.<sup>[23–34]</sup> In parallel and in cooperation with Mashiko *et al.*, Dong *et al.* performed light emission by STM<sup>[35]</sup> and tunneling electron induced luminescence<sup>[36]</sup> from the model molecule-surface generated by Jung, Gimzewski *et al.* a few years later



in 2003. In addition to this Suzuki *et al.*<sup>[37]</sup> created a self assembling dynamic monolayer of Cu-TBPP on Ag(001).

Another route was taken by Moresco *et al.* who developed a molecular switch by the rotation of a single TBP-group on different Cu surfaces and created a model system for molecular electronics.<sup>[38–43]</sup>

At the start of this century the group of Hipps carried out Orbital-Mediated STM on Cu-,Co- and Ni-TPPs deposited on Au(111)<sup>[44–46]</sup>. Very recently Co-TPP deposition on respectively Cu(110)<sup>[47,48]</sup> and Cu(111)<sup>[49]</sup> were performed, respectively resulting in self assembled chiral domains and achiral domains aligned with the main copper-axes. The free-base version has been analysed on Cu(110).<sup>[47]</sup> No self-assembly was observed.

Studies that focussed on the behaviour of diverse phthalocyanines<sup>[50]</sup>, a similar molecule, have also been carried out parallel in the 1990s.<sup>[51–54]</sup> Phthalocyanines are extensively used as pigments and dyes, and serve as models for biologically important species such as porphyrins. Presently phthalocyanines are still subject of research and are specially interesting in comparison studies with porphyrins.<sup>[55,56]</sup>

Whereas the porphyrins in the studies mentioned above are either free base or metallised before deposition, Marbach *et al.*, developed a method of in situ metallation of TPP with cobalt,zinc<sup>[57]</sup> and iron<sup>[58,59]</sup> by separate deposition of metal atoms after creation of a porphyrinic monolayer. Apart from this they also found existence of TBPP polymorphism on the Ag(111) surface. The second method of in situ metallation is by surface ad-atom capturing, which has been described by Auwärter *et al.*<sup>[60]</sup> who analysed the adsorption of tetrapyrrolyl-porphyrin molecules on Cu(111) and Ag(111). Metallation was observed only in the first case.

Recently the TBPP model system has been extended by Guo *et al.*<sup>[61]</sup> who characterised pre-metallated Zn-TBPP and Pt-TBPP on Cu(100) and free-base TBPP on Au(100) on which STM induced photo-emission was performed. Another very recent development is the creation of supra-molecular nano-architectures.<sup>[62,63]</sup> And the surface catalysed dehydrogenation of flat coronenes into hemispheres.<sup>[64]</sup>

The molecule of subject in this thesis, TM-TPP, could serve as a model system for other possible studies. TM-TPP is achiral and the specific selected replacement of CH<sub>3</sub> groups with p,o,(-chiral) groups might lead to different interactions or even chirality. Furthermore the free-base version opens the possibility to add either a metal in situ or ex situ, via which interesting other properties e.g. magnetic properties and the influence on

the surface conformation can be analysed. Not only the molecule can be varied, but also the surface. The choice for Cu(110) has been made considering the surface corrugation and the possible interactions due to the increased surface energy with respect to other surfaces.

Moreover it fits exactly in between the most studied porphyrins: TPP that lacks phenyl substituents and TBPP that has eight bulky groups attached to the phenyl rings. TM-TPP contains one group per phenyl more, however the individual methyl-groups are relatively smaller and are expected to show different interactions. This is also favoured by the fact that the TB groups are situated at the 3,5 positions and the methyl groups at the 2,4,6 positions.

After a brief introduction on the general electronic properties of porphyrin molecules without any substituents, this chapter continues with a description of the effect that meso-phenyl-substituents generate on the core (phenyl-core coupling).

## 1.1. Porphyrins: electronic structure

Porphyrin is derived from the latin word: *porfura* → purple. This purple colour can be explained by the electronic absorption spectrum, which consists of a strong transition to the second excited state, a Soret or B-Band accompanied by a low intensity N-band, that is closely related and at  $\approx 400$  nm, and a weak transition to the first excited state at  $\approx 550$  nm (Q-band). The B and Q band both arise from  $\pi - \pi^*$  transitions. The visible absorption spectrum of FBP (Free-Base Porphyrin) is four banded, whereas MP (Metal Porphyrin) only shows 2 bands. This difference is based on the absence of the protons that are present in FPB, hence the conjugated ring symmetry changes from rectangle to square i.e. from  $D_{2h}$  to  $D_{4h}$ .<sup>[65]</sup>

The first and successful but, at present date, oversimplified mechanism to understand the absorption spectrum of porphyrins was described by Gouterman in 1959.<sup>[66]</sup> He proposed a “four-orbital” model, that consisted of two HOMOs  $\pi$  and two LUMOs  $\pi^*$  orbitals based on naphthacene.<sup>[67]</sup> The porphyrin macrocycle consists of 22  $\pi$ -electrons, however due to tautomerisation there are six possible delocalisation pathways, of which one is shown in Figure 1.1. Only 18  $\pi$  electrons participate. This is consistent with Hückels rule of aromaticity ( $4n+2$ ). It is this conjugation that causes the Soret band to appear in the visible region as the molecular orbital energies show smaller separation.<sup>[68]</sup>

Modifications of the peripheral double bonds of porphyrins induce changes in the absorption spectra and hence color differences in porphyrins, varying from the purple colour of natural porphyrin to the sea-green appearance of reduced forms as long as the delocalisation pathway remains.<sup>[69]</sup> It has also been argued that there are other pathways possible using a 16-membered ring or 20-24 membered rings.<sup>[70]</sup> In synchronisation with the symmetry, the Q and B-band of MP consist of a degenerate electronic transition and two separate transitions for FBP are known to exist.

The most recent and detailed approach of the explanation of the free base electronic properties has been given by Baerends *et al.*<sup>[70]</sup> who used DFT/TDDFT (Density Functional Theory/Time-Dependent DFT) calculations. They have generated this by considering the individual properties of the Pyrrole rings, which subsequently are combined with the methine bridges. This resulted in the following MO-model (Figure 1.2).

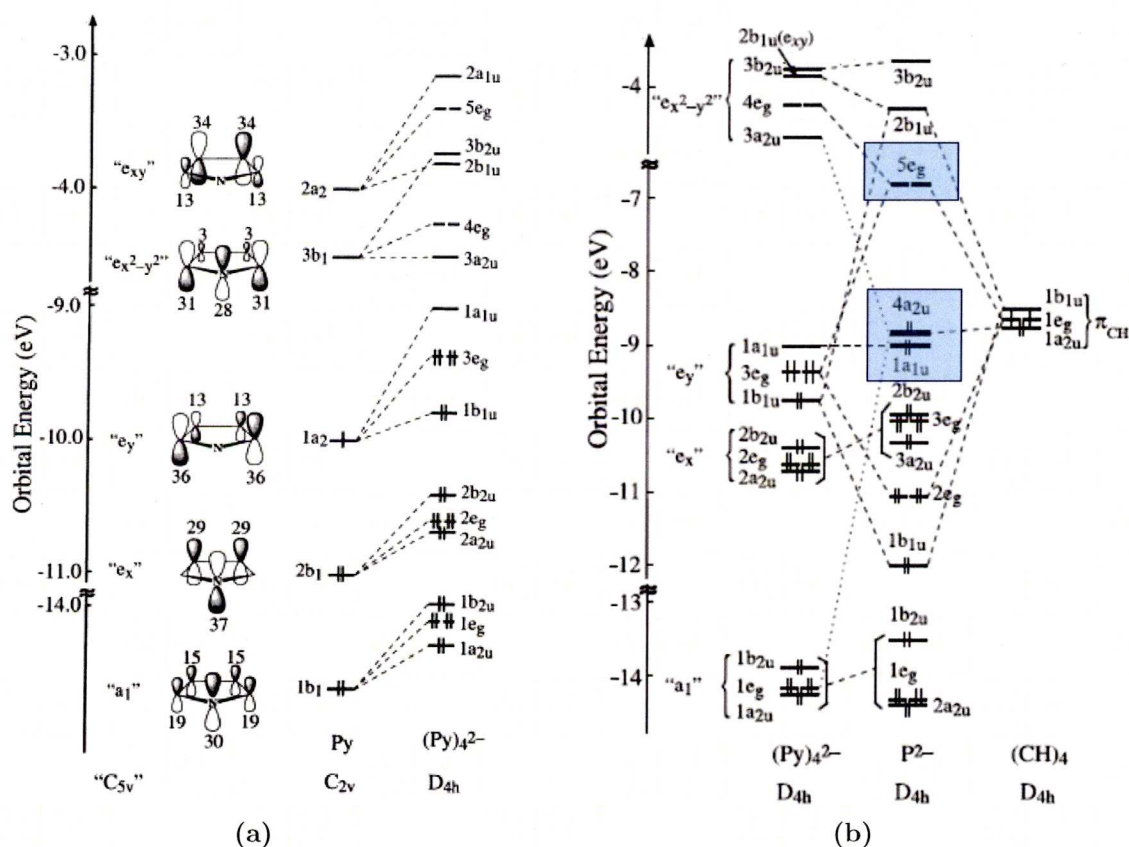


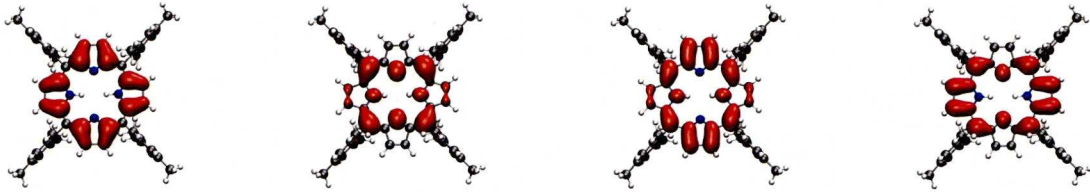
**Figure 1.2.** – (a) Orbital energy diagram of the pyrrolic ring system. The relative contributions of the individual C and N  $p_z$  AOs to MOs is indicated. (b) Orbital pyrrole-methine interaction diagram. Gouterman's orbitals are highlighted (g=gerade, u=ungerade).<sup>[70]</sup>



The pyrrolic  $\pi$ -system is characterized by an  $A_1$  combination ( $a_1$ ), with a large weight on the more electronegative N-atom. Furthermore non-degenerate  $E_1$  ( $e_x, e_y$ ) orbital sets exist. The more stable  $e_x$  configuration with amplitude on the  $C_\beta$  and the N-atoms is 1.12 eV lower in energy compared to the  $e_y$  configuration, where the biggest amplitudes are located on the  $C_\alpha$ -atoms. In contrast to the  $e_x$  orbital, where the nodal plane is located on the  $C_\alpha$ -atoms, the interaction with the methine bridges will be significant in the case of the  $e_y$  orbital. The  $E_2$  orbitals ( $e_{x^2-y^2}, e_{xy}$ ) are split by the N-perturbation too, with an energy difference of 0.55 eV. The  $e_{x^2-y^2}$  has a relatively large amplitude on the  $C_\alpha$ -atoms as well and is, therefore, expected to participate in the bonding with the methine bridges. The MOs of the four Py-rings combined without bridges form symmetric combinations as indicated in the figure. The high  $C_\alpha$  amplitudes of the  $E_2$  orbitals generate significantly more overlap and energy dispersion.

The interaction of the  $\text{Py}_4$  cage with the methine bridges is based on 20  $\pi$  electrons: the neutral rings supplemented with two electrons, which generates a fully occupied  $3e_g$  level and it gives the full porphyrin a  $2^-$  charge. In FBP this is counterbalanced by addition of two inplane protons in the core and in MP by insertion of a  $2^+$  charged metal. As expected and visualised in the right part of Figure 1.2 the  $e_x$  orbitals are transported to the porphyrin almost unperturbed by their lack of interaction with the methine bridges resulting in small energy gaps, whereas the  $e_y$  orbitals do show strong interaction with orbitals of matching symmetry in the set of  $\text{CH}_4$   $\pi$ -orbitals. The anti-bonding  $5e_g$  (degenerate LUMO, see Figure 1.3) and  $2b_{1u}$  orbitals are stabilised by and almost energy-equivalent to the  $E_2$  type orbitals. The also almost energy equivalent HOMO and HOMO-1, which are similar to the Gouterman orbitals, are derived from the  $e_y$  orbitals and the  $\pi_{CH}$  orbitals are non-bonding orbitals. The nodal planes in  $1a_{1u}$  (HOMO-1) through the CH-bridges show a lack of amplitude at the bridges and is virtually 100% Pyrrole- $e_y$ .

The  $4a_{2u}$  orbital is an in-phase combination of CH bridge C-atoms  $\pi$ -orbitals. It has admixture of  $3a_{2u}$  and  $1a_{2u}(\text{Py}_4)$  orbitals which in turn mix with the  $1a_{2u}-(\text{CH})_4$ , which shows that the amplitudes on the pyrrolic N-atoms are reinforced, in contrast to the  $C_\alpha$  which undergo destructive interference. The calculation shows that the HOMO in fact does have a strong amplitude at the methine bridges and amplitude with reversed sign at the  $N_p$ . Furthermore the  $5e_g$  a degenerate LUMO consists of anti-bonding combinations of the  $(\text{Py})'_4 e'_y - 3e_g$  with the  $(\text{CH})_4 1e_g$  and is stabilised by the  $(\text{Py})_4 e_{x^2-y^2} - 4e_g$ . The  $e_y - 3e_g$  and  $e_{x^2-y^2} - 4e_g$  are located on different sets of pyrrole rings i.e.  $e_{g,xz}$  combinations are formed with  $e_y$  orbitals on the y-axes and  $e_{x^2-y^2}$  on the x-axes and the other way



(a) HOMO-1 -0.35 eV      (b) HOMO 0.00 eV      (c) LUMO 1.77 eV      (d) LUMO+1 1.79 eV

**Figure 1.3.** – The frontier orbitals of TM-TPP are similar to the orbital configuration of porphine,<sup>[70,71]</sup> with the requirement that the phenyl rings are perpendicular to the core minimizing wave-function overlap (VASP DFT<sup>[72]</sup> contour value of  $\pm 0.01$  a.u.<sup>3</sup>).

around for  $e_{yz}$  combinations. Hence admixture of  $e_{x^2-y^2} - 4e_g$  creates amplitude on the  $N_p$  and  $C_\alpha$  atoms of two pyrrole rings that do not show amplitude in the other case.

The two HOMOs and the LUMOs are the four orbitals that are important for the UV-Vis absorption. The Q and B band consist of transitions which involve orbitals originated by the  $e_y$  set and the  $\pi_{CH}$  orbitals. Due to the fact that excitations find their source in non-bonding orbitals to anti-bonding orbitals, transition energies are low. The proximity of both HOMOs cause the near-degenerate  $1a_{1u} \rightarrow 5e_g$  and  $4a_{2u} \rightarrow 5e_g$  to lead to  $E_u$  excited states.<sup>[70]</sup> Degeneracy or near degeneracy with a small coupling matrix element induce strong 50/50 mixing. Ignoring spin, the electrons are singlet coupled. Hence  $1e_{u,y} = 1a_{1u}5e_{g,xz}$  and  $2e_{u,y} = 4a_{2u}5e_{g,yz}$ . This leads to the following transition dipole matrices  $\langle 1a_{1u} | y | 5e_{g,xz} \rangle$  ( $=3.30$  a.u. FBP, both  $e_y$  origin) and  $\langle 4a_{2u} | y | 5e_{g,yz} \rangle$  ( $2.72$  a.u. FBP, both  $\pi_{CH}$  origin). The intensities are high since the transition dipole matrices are large. Multiplication with  $y$  certifies not only that the signs are such that constructive interference is created but also the introduction of a multiplication factor of 7 a.u., which is the distance of the origin to the pyrrolic centroid. The low energy combination, that occurs in the  $1^1E_u$  state and which is responsible for the Q-band has low intensity (oscillator strength  $f=0.0052$ ), whereas the high energy combination,  $2^1E_u$  state and forming the B-band has high intensity (oscillator strength  $f=1.0214$ ). This is respectively due to opposite and parallel transition dipoles.

The dipole matrices that are generated from excitations that have their origin in  $e_x$  derived orbitals do not lead to high intensity of the Gouterman transitions. There is no overlap between the  $e_y$  orbitals that create the  $5e_g$ . Due to symmetry reasons



$\langle 3e_g | y | 5e_g \rangle = 0$ , the other two are non-zero, but significantly smaller than the Gouterman transitions.

Similar MO-models can be made for MP (Figure 1.4). MP are particularly interesting because of their spectroscopic, magnetic and electrochemical properties. The most recent DFT-SQM calculations<sup>[71,73]</sup> show that many of the electronic properties of metal porphyrins are insensitive to phenyl group presence and hence it is required that only small deviations from planarity are maintained ( $D_{4h}$ ). Moreover peripheral attachments at other than the  $C_{meso}$  drastically alter these properties. Therefore the outer MO level position and ordering in MP and MTPP are the same. Four phenyl groups change the ionization potentials by  $\approx 0.4$  eV, the electron affinity is changed by  $\approx 0.2$  eV and non-planarity induces energy differences of only 0.05 eV. The N-M bond length is  $\approx 2.0 \pm 0.05$  Å for the five metals. As can be concluded by comparison of Figure 1.2 with Figure 1.4 the electronic configuration of FBP and FBTPP in the frontier orbitals is similar. The main differences are that phenyl orbital bands are formed at relatively low energy, in this case  $\approx -6.5$  eV. Also the two protons in the core are ignored, resulting in other HOMO, LUMO, and orbital separation, which are stabilized by metal addition. Metal addition also shifts the  $a_{1u}$  orbital towards the  $a_{2u}$  creating near degeneracy. This is similar to the FBP. The energy however is insensitive to the nature of the metal. Addition of the two missing electrons gives the former HOMO and LUMO situation. The calculated electronic configurations will only be discussed for CoTPP and CuTPP as these are relevant for the next chapters in this thesis.

The metal 3d orbitals are represented by  $a_{1g}, b_{1g}, e_g$  and  $b_{2g}$ , which are respectively  $d_{z^2}$ ,  $d_{x^2-y^2}$ ,  $d\pi$  ( $d_{xz} + d_{yz}$ ) and  $d_{xy}$ . Furthermore, the energies of the d-metal orbitals drop with respect to the  $d_{x^2-y^2}$ ,  $d\pi$  and  $d_{xy}$ . The fractional contribution of the first decrease is due to orbital mixing as the energy of the metal orbital falls into the range of the porphyrin MO. In contrast to hydrogen, all the metals do not show a profound influence on the  $a_{1u}$ , hence the interaction between metal  $\pi$  and porphyrin  $\pi$  orbitals is limited.

Typical for both CoTPP and CuTPP is that the first oxidation is calculated to take place on the porphyrin orbitals ( $a_{2u}$ ) resulting in  $\text{Co}^{II}\text{TPP}^+$  and  $\text{Cu}^{II}\text{TPP}^+$  radicals. Then subsequently the metal donates an electron to the porphine ( $\text{M}^{II}$  to  $\text{M}^{III}$ ). Reduction for CoTPP takes place as expected in the  $d_{z^2}$  orbital, which is already half filled. In contrast CuTPP shows a different behaviour. Reduction does not take place as expected and calculated by previous studies in the  $b_{1g}$  level, which would lead to a  $d^{10}$  configuration, but in the  $2e_g$  orbital, which is  $d^9$ . This is attributed to d-d repulsion



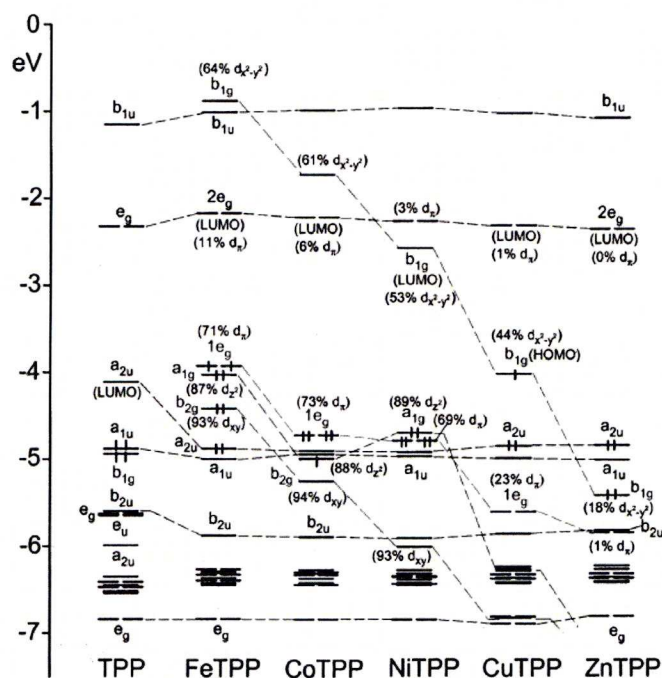


**Figure 1.4.** – a) Frontier Orbital level diagram for various (M)-TPP (deprotonated)<sup>[71]</sup>

energy involved in pairing  $b_{1g}$  electrons. However reduction of NiTPP, with an empty  $b_{1g}$  LUMO takes place in the  $2e_g$  as well, shifting the LUMO above the latter. Unmentioned, but possible: a similar situation could occur for CuTPP, in which the odd electron occupying the HOMO, shifts to the  $2e_g$  level upon the first reduction. It then is energetically favourable to  $b_{1g}$ . Moreover both degenerate  $2e_g$  levels are then half filled (Hund's rule). Indication of this is given because the third reduction is said to occur in either of these levels, due to near degeneracy. The fourth reduction only takes place in the  $b_{1g}$  level (Figure 1.4).

The calculated energy gaps between the HOMO and the LUMO of uncharged CoTPP and CuTPP are respectively: 2.50 and 1.71 eV, numbers that are very similar to the MP versions of these molecules viz: 2.55 and 1.75 eV. This confirms that the phenyl substituents do not heavily influence this. In contrast ionization of the metal does. Electron donating substituents e.g. phenyl, reduce the IP (0.5 eV), whereas electron withdrawing atoms (F,Cl) increase the IP (0.5-1.0 eV). The binding energies are 10.8 eV and 7.63 eV for CoTPP and CuTPP respectively. For the MP analogues these values are increased by 0.2, which leads to the conclusion that the peripheral phenyl rings cause a small reduction of the metal bonding. The relatively high thermal and high chemical stability of metal-porphyrin is related to the strong interactions. Both Co and Cu show negative electron affinities, -2.13 and -1.57 (-0.2 eV for MP). The difference is

ascribed to the differences in electronic configuration as outlined. Finally it has been calculated that highly electron withdrawing groups attached to the core weaken the metal-porphyrin interaction, and the effect is bigger with  $C_{meso}$ -substitution instead of  $C_\beta$  connection and vice versa for the electron affinity.

## 1.2. Porphyrin conformation, *meso*-phenyl-core coupling

Apart from free base porphyrins many types of metalloporphyrins are known.<sup>[74]</sup> Studies<sup>[75–77]</sup> were devoted to clarify the metal dependence of the non-planarity of porphyrins in both crystals and solution. In particular Shelnutt *et al.*<sup>[78–84]</sup> have proposed porphyrin model systems. They show that six out-of-plane normal modes and six in-plane normal modes are usually sufficient to describe the distortions of (metal)porphyrins (Figure 1.5). Their findings are confirmed by and based on extensive X-ray data and hence it may be assumed that porphyrin conformations found on surfaces will adopt one of these conformations even though the porphyrin-substrate is a 2D crystal interaction.

The saddle (*sad*) and ruffled (*ruf*) distortions are most common. The second involves twisting about the M-N bond, whereas the first is based on simultaneous displacement of opposite pyrrole rings below and above the mean plane. Non-planar vibrational deformations of square planar symmetry that occur in the two lowest frequency normal modes of the macrocycle do not deviate much from the  $B_{1u}$  and  $B_{2u}$  distortions. As  $88 < 206$  ( $k_b T$ ) $\text{cm}^{-1}$  perturbations of only small energies ( $9.1$  and  $16.5$   $\text{kJmol}^{-1}$   $\text{\AA}^{-1}$ ) can easily cause these distortions. The total energy along each normal deformation  $\hat{D}_m^\Gamma$  from equilibrium is given by:

$$E_{tot} = 2\pi^2 c^2 \sum_{\Gamma, m} (\tilde{v}_m^\Gamma)^2 (Q_m^\Gamma)^2 = \sum_{\Gamma, m} K_m^\Gamma (d_m^\Gamma)^2 \quad (1.1)$$

with the vibrational frequency  $\tilde{v}_m^\Gamma$  ( $\text{cm}^{-1}$ ) of the  $m^{th}$  normal mode of symmetry  $\Gamma$  and the speed of light ( $c$ ).  $Q$  are the normal mode coordinates,  $K$  the energy in  $\text{kJ mol}^{-1}$  and  $d = 1$   $\text{\AA}$ . Hence the deformation energy is proportional to the square of vibrational frequencies and therefore displacements along the lowest-frequency normal modes are less energy consuming. Distortions that are also observed are domed (*dom*) and the less frequently occurring degenerate waved (*wav*). The first is characterized by displacement of the metal out of the mean plane. The other is describing the creation of a sloped core

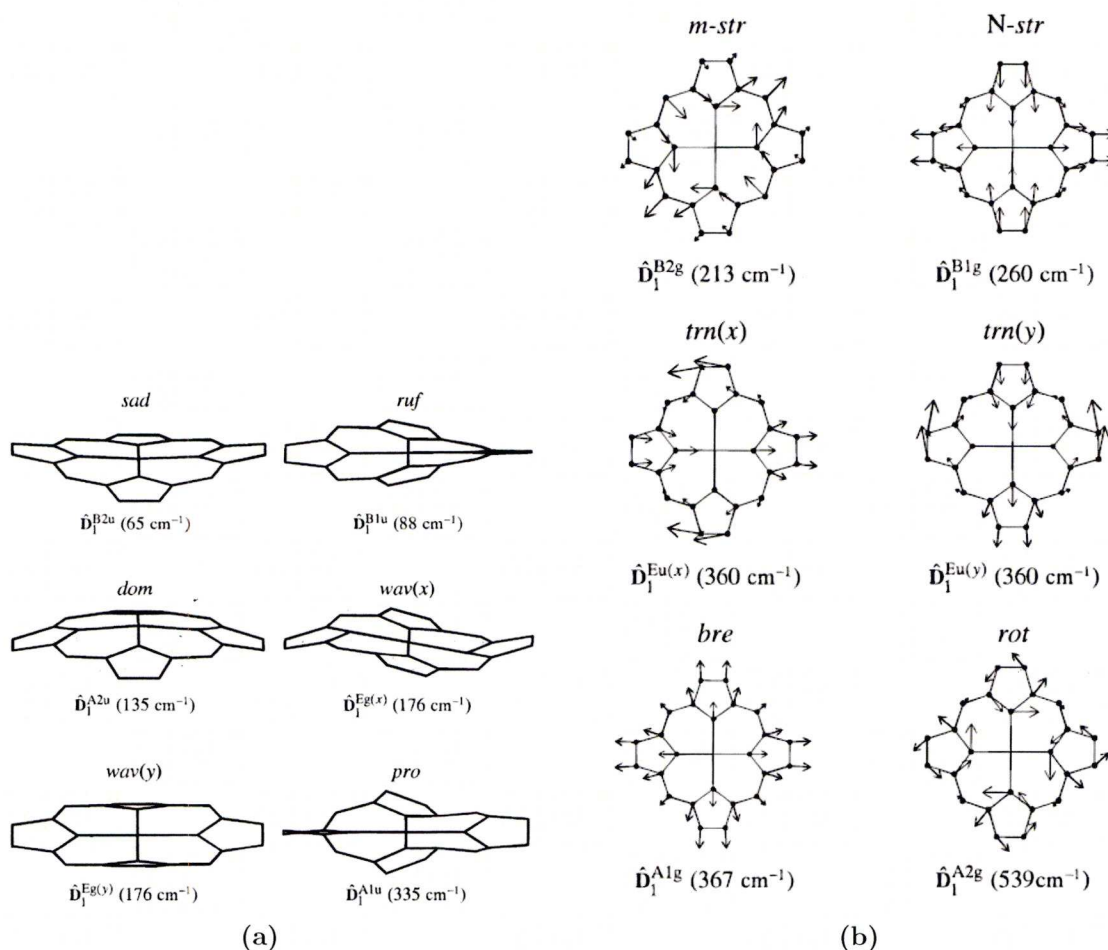


**Figure 1.5.** – Apart from the  $D_{4h}$  planar porphyrin there are six possible normal deformations. The lowest-frequency in (b) and out-of-plane (a) eigenvectors are shown. The atomic displacements shown are magnified by a factor five.<sup>[81]</sup>

by displacing half of the porphyrin upwards with respect to the mean plane and the other half downwards except for the two  $C_\beta$ - $C_\beta$  bonds that do not participate in the slope and that are folded in the opposite directions. The energy costs for these deviations from planarity are respectively 41.4 and 67.3  $\text{kJmol}^{-1}\text{\AA}^{-2}$ . The *pro* deformation is practically absent, it requires energetically large perturbations (238.4  $\text{kJmol}^{-1}\text{\AA}^{-2}$ ). Combinations could also occur: an example of this is the *gab* (gabled) conformer, which is an addition of *ruf* and *dom* displacements leading to a tunnel shape in which half of all the pyrrole units are below the mean plane and half above together with the metal and two of the opposite methine bridges. This is in case of 50/50 mixing, however, any proportion is allowed by symmetry. Another, at generally higher frequency, is the *wav(+)*, which combines both x and y *wav* modes.



According to the out-of-plane (oop) modes a description of the in-plane (ip) modes can also be given. The stretching deformations *m(eso)-str* and *N-str* respectively deform the porphyrin along opposite methine bridges and pyrrole rings. The translation (*trn*) deformation is degenerate and the displacement vectors resemble translational deformations in x and y directions. The *bre* deformation is a breathing mode of the porphyrin ring and the in-phase rotation of each pyrrole ring is described by the *rot* deformation. The accompanying distortion energies are: 100.1, 147.8, 280.5, 293.8 and 652.9 kJ.mol<sup>-1</sup>Å<sup>-2</sup>. This makes the *str* the most probable mode. The presence of the *sad* deformation usually is accompanied with a *m-str* mode of the C<sub>meso</sub> atoms.

It was found that peripherally symmetric substitution have a minor influence on the lowest-frequency macrocyclic normal modes and that the distortion energy is independent of the nature of the attached substituents.<sup>[79]</sup>

With respect to TPP, the first theoretical studies of surface interaction and aryl-ring rotation about the C<sub>meso</sub>-Ph bond has been studied by Mashiko *et al.*<sup>[29,32]</sup> who were interested in the discrepancy between experimental observations and theoretical calculations. Experimentally rotation occurs at room temperature, whereas theoretically steric hindrance does not permit this. Their main conclusion is that oop deformation of the porphyrin ring is essential for the rotation. This is in contrast to other studies<sup>[85]</sup>, that give a stronger preference for ip distortions. Moreover different groups show that strong interactions between the adsorbate and surface results in the four aryl ring rotation and forces the conformation to be altered, which is also dependent on substituent group differences.<sup>[25,28,86,87]</sup> Also the lowest energy conformations show close resemblance to a saddled and ruffled core. The other conformations found are different than above, which is attributed to surface-adsorbate interactions.

In 1997 the correlation between the saddling distortion of the porphyrin core and the tilting of the meso-aryl substituents was explained via molecular mechanics by Cheng *et al.*<sup>[88]</sup>, and attributed to environmental effects e.g. packing forces in crystals. However the computational method was limited. Recently this distortion was extensively studied by Rosa *et al.*<sup>[89]</sup>, who were able to show using DFT that synergy between porphyrin-core saddling and the twisting of meso-aryl substituents in the gas phase exist. Their calculations show that the environment only plays a minor role and that the mechanism is entirely governed by intrinsic electronic factors. A schematic representation indicating the different conformational angles for a TPP molecule is given in Figure 1.6.

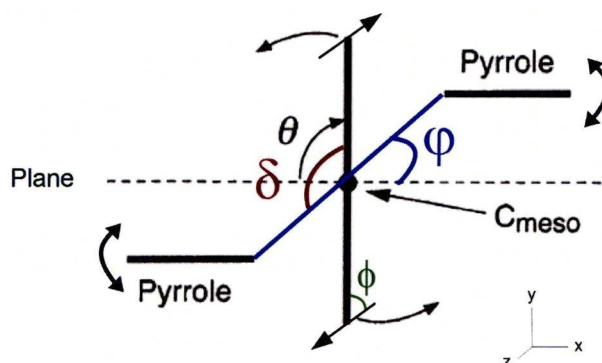


**Figure 1.6.** – The various angles present in a saddled TPP molecule:  $\varphi$  (saddling angle),  $\delta$  (dihedral angle),  $\theta$  (meso-aryl rotation twist angle),  $\phi$  (meso-aryl rotation tilt angle). Side view i.e. drawing  $\perp$  to the porphyrin plane and the  $C_{meso}$  bond. Modified<sup>[89]</sup>

Again it was found that meso-substitution has very little effect on the saddling motion of the porphyrin in the gas phase. Furthermore the saddling distortion demands energy ( $20 \text{ kcal.mol}^{-1}$ , TPP is planar). Hence TPP does not distort, however as the coupled motion is very soft only a small additional driving force e.g. surface or diacid formation can alter this. As can be derived from Figure 1.7 the lowest energy conformation is  $\phi = 10^\circ$  and  $\theta = 60^\circ$ . In case of planar TPP this minimum is broad, which means that the phenyl rings have a rotation regime in which the energy does not change much. This suggest that with increasing bulkiness of the groups attached to the phenyl this regime is compressed and that in the gas phase the substituents are forced closer to perpendicularity than with just a phenyl group.

The coupled mechanism results in a considerable stabilization, which means that the phenyl rotation is an energetically favourable process. This is fully attributed to orbital interaction. If the  $C_m\pi$  orbital is tilted to smaller angles than  $90^\circ$  it implicates that the phenyl has to rotate considerably to bring its  $C_1\pi$  orbital in significant overlap. The calculations show that these interactions are already of influence from  $\theta \leq 60^\circ$  to the molecule being planar. In the saddled version  $\varphi \leq 30^\circ$  these angles are smaller due to the fact that saddling already tilts the  $C_m$  orbital.  $\Pi$  conjugation can counteract the energy cost of saddling starting from the angles mentioned and hence this is a very plausible explanation of the observance of numerous (metal)porphyrins exploiting a saddled conformation with relatively small dihedral angles.

The conjugation mechanism does not lead to a totally flat porphyrin, which is attributed to a steric component (Pauli Repulsion,  $H_{ortho}$  vs.  $H_{beta}$ ). The plot in Figure 1.7 for a saddled system is shifted due to different interaction between the upper and lower

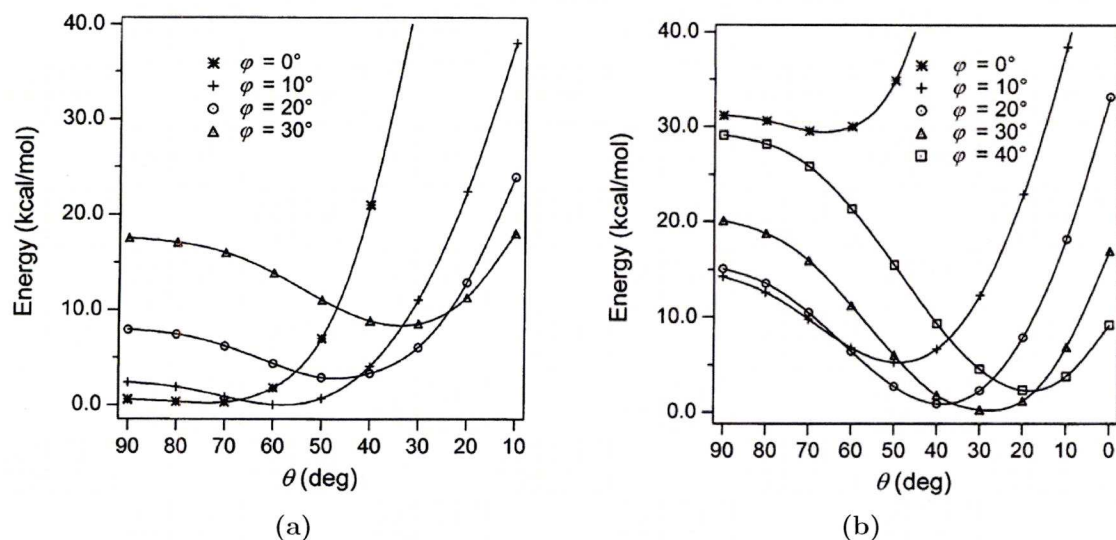


**Figure 1.7.** – a) Potential energy as function of the tilting angle for various saddled conformations of  $H_2TPP$  and b)  $H_4TPP^{2+}$  [89]

pyrrole rings. It has a broad minimum; The explanation for this is the much weaker steric repulsion for the saddled structure. This allows the phenyl ring to rotate to smaller angles before repulsive interactions appear. Concerning the double protonated TM-TPP; steric bulk prevents a dihedral angle smaller than  $50^\circ$  and hence the synergy mechanism is limited. The  $C_\beta$  displacement factor is  $\approx 0.3 \text{ \AA}$  smaller than in a similar version of TPP.

Another important consequence of saddling is the symmetry allowance of other modes e.g. for saddled porphyrins the metal  $d_{x^2-y^2}$ -porphyrin HOMO interaction will be enabled. DFT calculations show that upon saddling this overlap increases, whereas the overlap with the nitrogen lone pairs decreases. [90]



## Chapter 2.

# Gas Adsorption on Solid Surfaces

In the second half of the nineteenth century Faraday carried out many electrochemical experiments with metal electrodes.<sup>[91]</sup> He was the first to suggest that a surface catalysed reaction would be governed by the sticking of reactant molecules to a surface.<sup>[92]</sup> From 1916 to 1918 Langmuir<sup>[93–95]</sup> investigated adsorption and reflection of molecules on surfaces. Later his theory was more refined and made applicable not only to monolayers but also to multi-layers, via the BET-isotherm by Brunauer, Emmet and Teller in 1938.<sup>[96]</sup> Twenty years later Feynman showed that there are not just ‘some’ possibilities at the nano-scale, but ‘plenty’! In 1959 he already suggested the possible future use of nanoscale devices in all sorts of fields e.g. computer hardware, medicinal applications and storing (writing) information atom-wise.<sup>[97]</sup> Due to the invention of other experimental techniques a better insight into these molecular dynamical processes at surfaces was first given by field-ion microscopic studies in the late sixties of the former century. In 1994 an extensive review based on this technique of single-atom surface diffusion and cluster nucleation on metal surfaces was written by Kellogg.<sup>[98]</sup> Meanwhile STM-systems were continuously improved and the subsequent higher resolutions obtainable assist in the understanding of molecule, atom and substrate interactions. In recent years, various kinds of developments have been executed, from the creation of a nano-car<sup>[99]</sup> to creation of atomic-scale words and images at surfaces.<sup>[38,100,101]</sup>

### 2.1. Adsorption Types

When a molecule approaches a surface it experiences an attractive potential. Two types of adsorption are known: physisorption and chemisorption. Both were proposed by

Langmuir in 1915<sup>[102]</sup>, and first modelled by Lennard-Jones in 1932.<sup>[103]</sup> The model assumes that the substrate binding site is only of one type and neither the angle nor the orientation of the adsorbate with respect to the surface is important.

Physisorption is limited by the relatively weak Van der Waals (VdW) or dipole-dipole forces<sup>[104]</sup> that determine the interactions between substrate and adsorbate. The substrate-adsorbate bond strength is typically  $<20 \text{ kJmol}^{-1}$  (cf  $40\text{-}500 \text{ kJmol}^{-1}$  for chemisorption). The strength of the chemisorption bond depends on the position of the hybrid orbitals with respect to the Fermi energy ( $E_F$ ).<sup>[3]</sup> A molecule that chemisorbs to a surface can be initially found in a physisorbed state.<sup>[104]</sup>

A theoretical description of physisorption was given by Zaremba and Kohn in 1976.<sup>[105]</sup> They proposed that the total physisorption potential ( $V_{ph}$ ) between a single atom and a metal surface consists of a short-range repulsive potential ( $V_r(z)$ ) and a long-range VdW attraction ( $V_a(z)$ ):

$$V_{ph}(z) = V_r(z) + V_a(z) \quad (2.1)$$

The repulsive term is created by the overlap of filled atomic orbitals with the electronic states of the surface. A Pauli repulsion is experienced by the adsorbate when the surface interacts with the filled atomic orbitals.  $V_r(z)$  can be approximated by a Hartree-Fock treatment.<sup>[3]</sup> In the non-chemisorption range, i.e the overlap of metal and atom wave-functions is small, the attraction term  $V_a(z)$  is given by the Lifshitz potential:

$$V_a(z) = \frac{C}{z - z_0^3} + O(z^{-5}) \quad (2.2)$$

with  $O(z^{-5})$  the energy due to multipole and higher order perturbations which are normally neglected.<sup>[105]</sup> As previously stated the interaction of an instantaneous dipole on the atom with an induced charge fluctuation in the metal gives rise to VdW interactions and hence  $C$  is a constant which is related to the polarizability ( $\alpha(\omega)$ ).

$$C = \frac{1}{4\pi} \int_0^\infty \alpha(i\omega) \frac{\epsilon(i\omega) - 1}{\epsilon(i\omega) + 1} d\omega \quad (2.3)$$

with  $\epsilon(\omega)$  the dielectric function and  $i = \sqrt{-1}$ . The position to which the Lifshitz potential is referenced and found from the weighted average of the centroid of the induced



surface charge ( $\bar{z}(i\omega)$ ) is  $z_0$ :

$$z_0 = \frac{1}{2\pi C} \int_0^\infty \alpha(i\omega) \bar{z}(i\omega) \frac{\epsilon(i\omega) - 1}{\epsilon(i\omega) + 1} d\omega \quad (2.4)$$

The last equation shows that the reference plane position not only depends on the charge distribution but also on the dynamic screening properties of the surface. The bonding in a near-surface region is strongly influenced by the lattice truncation due to the many-body surface.<sup>[106]</sup> A physisorption interaction decays slower ( $z^{-3}$ ) than a VdW interaction between two isolated atoms ( $z^{-6}$ ). Since the adsorbate-surface interaction is relatively weak and less site specific, lateral interactions are important and can be of equal strength.

There is no distinct line between both physisorption or chemisorption. The latter, however, corresponds to the formation of a chemical bond between adsorbate and surface. Which can be split into non-dissociative chemisorption and dissociative chemisorption processes. The Anderson-Grimsley-News approach<sup>[3]</sup> gave the first limited description of local atomic adsorption at surfaces. Only the adsorbate nearest neighbours interaction is taken into account. The main conclusion was that the electronic states existing after chemisorption not only depend on the electronic structure of the substrate and the adsorbate but also on the coupling strength of both. A strong and weak coupling limit are proposed. Where respectively the adsorbate level interacts strongly with a narrow d-band or weakly with a broad s-band of a transition metal for which the orbital interaction with the adsorbate is minimal. The first results in orbital splitting, bonding and anti-bonding combinations. Typically, the electronic states of a molecule approaching the surface interact with metal electronic states. Especially since metals usually do not exhibit band gaps. The adsorbate molecular orbitals are broadened and change in energy by interaction with the surface electrons of similar energy. Core levels, that are usually situated below the substrate valence band, show little interaction and degenerate gas phase orbitals may not exist at the substrate.

## 2.2. Adsorbate surface mobility

Diffusion on surfaces was first described by Burton, Carbrera and Frank<sup>[107]</sup>, who developed the BCF-model for surface-mobility and the rate of steps in 1950. This model is based on an equidistant parallel ordered array of steps.

Under atmospheric circumstances the creation of crystals is mainly determined by volume-transport (grown from liquid), followed by area diffusion. In contrast UHV conditions create crystal growth from the gas phase and hence the latter automatically determines the growth rate. The transport of particles on a surface can be described by a 2D implementation of Fick's laws.<sup>[108]</sup>

$$J(x, y, t) = -D\nabla c(x, y, t) \quad (2.5)$$

and

$$\frac{\partial c(x, y, t)}{\partial t} = D\nabla^2 c(x, y, t) \quad (2.6)$$

with  $J$  the flux,  $c$  the adsorbate unit concentration,  $D$  the diffusion coefficients, which are assumed to be isotropic (the BCF model is limited for most crystal surfaces are anisotropic). The model assumes that step supply on a limited length  $\Delta x$  is established by both vertical (gas-phase adsorption) and horizontal flux. Discharge occurs only horizontal i.e. no desorption. Hence the increase of adsorbed species ( $N$ ) per unit time ( $t$ ) is:

$$\frac{\Delta N}{\Delta t} = l(J_{in} - J_{out}) + lJ_v\Delta x \quad (2.7)$$

with  $l$  the length. The resulting change in concentration is:

$$\frac{\Delta c}{\Delta t} = \frac{l}{l\Delta(x)} \frac{\Delta N}{\Delta t} \equiv \frac{\Delta J}{\Delta x} + J_v \quad (2.8)$$

with  $J_v$  the vertical flux. When  $\lim_{\Delta t, \Delta x \rightarrow 0}$  and the system is static then

$$\frac{dc}{dt} = 0 = \frac{dJ_h(x)}{dx} + J_v(x) = 0 \quad (2.9)$$

with  $J_h$  the horizontal flux. As a result of Fick's law

$$J_h(x) = -D \frac{dc(x)}{dx} \quad (2.10)$$

$J_v$  is place-independent and mainly determined by pressure.

$$J_v = J_v \downarrow(x) + J_v \uparrow(x) = \frac{c_\infty}{\tau} - \frac{c(x)}{\tau} \quad (2.11)$$

with:

$$\tau = \frac{k_B T}{h} e^{\frac{-\phi}{k_B T}} \quad (2.12)$$

with  $k_B$  the Boltzmann constant,  $\phi$  the binding energy,  $\tau$  the residence time. At infinite distance of a step the  $(c(x \rightarrow \infty) = c_\infty)$  at the same time  $J_h c(x \rightarrow \infty) = 0$  and therefore:

$$-D \frac{d^2 c(x)}{dx^2} + \frac{c_\infty - c(x)}{\tau} \quad (2.13)$$

Einstein showed that the average distance of a random travelling particle from its starting point is equal to the squareroot of the total distance<sup>[109]</sup>:  $\chi_s = \sqrt{\tau D}$ . Substitution of this in equation (2.13) gives the Burton-Carbrera-Frank (BCF) equation.

$$-\chi_s^2 \frac{d^2 \Psi(x)}{dx^2} + \Psi(x) = 0 \quad (2.14)$$

The solutions of this differential equation show that the concentration is low at the steps, which creates a flux towards these steps. This simulates that the electronic structure from steps differ from that of terraces.

At surfaces different binding sites exist that are separated by energetic barriers. The diffusion barriers are represented by the separation of these binding sites. For a uniform potential diffusion is governed by the following Arrhenius type equation:

$$D = D_0 e^{\frac{E_{diff}}{RT}} \quad (2.15)$$

$$D = \frac{v d^2}{2b} \quad (2.16)$$

where  $D$  is the diffusion coefficient,  $D_0$  the diffusion prefactor,  $E_{diff}$  the activation energy (which at anisotropic substrates depends on the diffusion direction). The effective diffusion barrier experienced by the adsorbate is larger when the corrugation in the adsorbate/surface potential is greater.  $D$  is related to the hopping frequency ( $v$ ), the mean square hopping length ( $d^2$ ) and the diffusion dimensionality. The root mean square distance travelled by an adsorbate with  $b=2$  (2D surface) results in:

$$\langle \sqrt{x^2} \rangle = \sqrt{4Dt} \quad (2.17)$$



Chemisorbed molecules show higher diffusion barriers than do physisorbates.  $D$  is constant in the absence of lateral interactions or defects. In contrast to molecules, ad-atoms that strongly interact with the substrate show an exchange mechanism of diffusion.<sup>[3]</sup>

## 2.3. Lateral interactions

A number of adsorbate-adsorbate interactions<sup>[110]</sup> are present when molecules are deposited on surfaces and some are outlined below. First direct interactions e.g. covalent or metallic interactions can be created between adsorbates as long as each possesses a partially filled valence orbital. These bond-types are dominant for adsorbates that exhibit a similar electronegativity to the substrate.

Furthermore a second type of attractive interactions that in contrast to the first are non-covalent: electrostatic interactions, dipole-dipole<sup>[111]</sup> and Van der Waals (VdW) forces.<sup>[3]</sup> These interactions are the driving force behind self-assembling or self-organising monolayers. A dipole moment is induced within a neighbouring molecule, which can originate from instantaneous distortions in the electron clouds of atoms and molecules. Large VdW interactions are exhibited by molecules with a high molecular weight and are dominant in ad-layers of large non-polar adsorbates.

The third type of interactions are direct Coulombic interactions, which occur for ad-atoms that have undergone charge transfer with the substrate or, alternatively, include strongly electropositive or electronegative atoms within a molecular adsorbate. Both repulsion as well as attracting Coulombic forces are known to exist. The first lead to a situation where adsorbates maximise their average separation by forming a two dimensional dispersed phase in order to decrease the interaction energy (equation (2.18)). This results in the formation of densely packed two-dimensional structures.

$$E = - \int_{r=\infty}^r F dr = \frac{-1(\delta^+)^2}{4\pi\epsilon} \int_{\infty}^r dr = \frac{|\delta^+|^2}{4\pi\epsilon r} \quad (2.18)$$

with  $\delta$  the charge,  $r$  the radius,  $F$  the Coulombic force and  $\epsilon$  the vacuum permittivity.<sup>[68]</sup>

The fourth and last type are indirect substrate mediated forces by the electrons in the substrate. The d-states of neighbouring transition metal atoms are shifted downwards when an adsorbate is bound. A weaker metal-atom-adsorbate interaction for subsequent adsorbates is induced.<sup>[3]</sup>

The arrangement of adsorbed atoms and molecules within the island relative to the underlying substrate is usually called incommensurate, when there is no common periodicity between the overlayer and the surface mesh, i.e. substrate-adsorbate interactions are of similar or smaller magnitude to the lateral interactions. In contrast a commensurate overlayer possesses a simple coincidence with the underlying surface mesh and arises if the substrate-adsorbate interactions dominate. Detailed information of adsorbate-adsorbate interactions in chemisorption systems can be found in<sup>[112]</sup>. A quantified determination has been given by Besenbacher *et al*<sup>[113]</sup>.

## 2.4. Adsorption kinetics

Adsorption is an exothermic process and thus  $\Delta H_{ads} < 0 \text{ kJmol}^{-1}$ . Adsorption that occurs only at very low temperatures possess  $\Delta H_{ads}$  in the range of: 4-8  $\text{kJmol}^{-1}$ , whereas adsorption that survives at elevated temperatures possess  $\Delta H_{ads}$  of 40-120  $\text{kJmol}^{-1}$  or even higher.<sup>[103]</sup> Langmuir<sup>[102]</sup> derived the simplest expression describing the dependence of surface coverage on the pressure of the gas above a surface at a fixed temperature. He assumed that:

- Adsorbed molecules do not interact with each other and only occupy one of the available equivalent sites.
- The molecules are localised once adsorbed and  $\Delta H_{ads}$  is constant, coverage independent.
- A dynamic equilibrium exists between the gas and the adsorbed layer at constant temperatures.
- Adsorbate molecules from the gas phase are continually colliding with the surface. In case of a vacant adsorption site they stick, while for a filled site, they are reflected back. The rate of surface collision ( $Z$ ) by a gas of molecules with a surface is proportional to its number density and to the average molecular velocity and is given by the Hertz-Knudsen equation:<sup>[3,92]</sup>

$$Z = \frac{P}{\sqrt{2\pi m k_B T}} \quad (2.19)$$

with  $k_B$  the Boltzmann constant,  $T$  temperature,  $P$  the pressure,  $m$  the mass. The rate of adsorption is.

$$R_{ads} = Z s_0 (1 - \theta) e^{-E_{ads}/RT} \quad (2.20)$$

with  $v_{ads}$  the adsorption rate, which includes an initial coverage  $\theta$ , an activation coefficient to overcome the adsorption barrier and  $s_0$  is the initial sticking coefficient.

This lead to the next formula for associative adsorption:  $A(g) + S(s) \rightleftharpoons A-S(s)$ . At equilibrium  $R_a = R_d$ :

$$k_a Z (1 - \theta) e^{-E_a/RT} = k_d \theta e^{-E_d/RT} \quad (2.21)$$

with  $k_a$  and  $k_d$  the rate constants for respectively adsorption and desorption, and

$$P = \sqrt{2\pi m k_B T} \frac{k_a}{k_d} \frac{\theta e^{(E_a - E_d)/RT}}{(1 - \theta)} \quad (2.22)$$

now,  $\Delta H_{ads} = E_a - E_d$  rearranging gives:

$$P = \frac{\theta}{b(1 - \theta)} \quad \theta = \frac{bP}{1 + bP} \quad (2.23)$$

where

$$\frac{1}{b} = \sqrt{2\pi m k_B T} \frac{k_d}{k_a} e^{\Delta H_a/RT} \quad (2.24)$$

Equation (2.24) is the Langmuir adsorption isotherm for associative adsorption. Analogous to this the Langmuir isotherm for dissociated adsorption of a diatomic molecule can be derived.<sup>[3,92]</sup>

These isotherms are only applicable to a monolayer and do not apply to multi-layers, for which the BET isotherm has been developed.<sup>[96,114]</sup> The BET isotherm is also based on several assumptions:

- Adsorption of the first layer takes place on an array of uniform surface site energy.
- Adsorption of the second layer can only take place on top of the first, the third on the second etc.



- When the number of adsorbed layers exceeds unity, the equilibrium constants are equal and  $\Delta H_{ads} = -\Delta H_{vap}$
- The rate of condensation is equal to the rate of vaporisation at equilibrium.

As can be concluded from the last assumption, the BET isotherm has been derived from the Langmuir isotherm, and can be written as:

$$\frac{P}{V(P_0 - P)} = \frac{z - 1}{V_m z} \frac{P}{P_0} + \frac{1}{V_m z} \quad (2.25)$$

If  $P/P_0$  is relatively small a concave curve exists with respect to the pressure axes and for higher values the curve is convex. At very low pressures that correspond to a maximum of a complete monolayer the curve is linear. An important factor is the lack of adsorbate-adsorbate interactions<sup>[115]</sup> in both the Langmuir and the BET-isotherm. It assumes layer by layer growth, which is not always the case. Other less common isotherms can be found in the literature.<sup>[116]</sup> These are among others based on linear (Tempkin) and logarithmic (Freundlich) changes of  $\Delta H$  with respect to pressure. It can be concluded that a single isotherm is not sufficient to account for the whole pressure and coverage range.

## 2.5. Temperature programmed desorption

Temperature programmed desorption (TPD) measurements were first carried out in 1958 and 1961<sup>[117,118]</sup> and theoretically refined by Redhead.<sup>[119]</sup> A temperature ramp is applied in TPD and the desorption rate  $N(t)$  followed by monitoring the amount of adsorbate desorbed into the gas phase as a function of temperature, usually via Quadrupole Mass Spectrometry.<sup>[110]</sup> The desorption rate is described by the Polanyi-Wigner equation:<sup>[3]</sup>

$$N(t) = -\frac{d\theta}{dt} = v_n \theta^n e^{-E/RT} \quad (2.26)$$

with  $t$  the time,  $n$  the desorption reaction order,  $\theta$  the surface coverage,  $v_n$  the rate constant and  $E$  the desorption activation energy in  $\text{kJmol}^{-1}$ . If one assumes that the last is coverage independent and during desorption the sample temperature changes linearly with time i.e:

$$T = T_0 + \beta t \quad (2.27)$$

with  $\beta = dT/dt$ , and when equation (2.26) is differentiated ( $d^2N/dT^2 = 0$ ) to find the maximum desorption rate temperature ( $T_p$ ) it results in:

$$\frac{E}{RT_p^2} = n\theta_p^{n-1}\frac{v_n}{\beta}e^{-E/RT_p} \quad (2.28)$$

with  $\theta_p$  surface coverage at  $T = T_p$ . The last equation shows that a first order desorption is independent of the coverage and thus  $E$  can be found directly from  $T_p$  measurement as long as  $v_1$  is known. When  $10^{13} > v_1/\beta > 10^8$  an estimation can be made via:

$$E = RT_p(\ln \frac{v_n T_p}{\beta} - 3.46) \quad (2.29)$$

By increasing coverage, the desorption peak maximum remains at a constant temperature and increases in intensity. The initial surface coverage can be obtained by measuring the area under  $N(t)$  since:

$$\theta_0 = \int_0^\infty N dt \quad (2.30)$$

By consideration of the variation in the desorption peak shape and maximum as function of the temperature the order of desorption can be ascertained for adsorbate systems that do not exhibit lateral interactions. Coverage-dependent lateral adsorbate interactions or the presence of more than one distinct binding site with differing activation energies for desorption may lead to the existence of multiple desorption peaks and coverage dependent shifts in peak maxima.<sup>[112]</sup> Hence TPD is also used to monitor (decomposition) reaction mechanisms. When an adsorbate reacts on a surface it may decompose in products of different masses, which could indicate reaction limited desorption.<sup>[110]</sup> A method of determining whether lateral interactions are significant was developed by Falconer and Madix.<sup>[120]</sup>

In contrast to multi-layer desorption kinetics, mono-layers that are chemisorbed generally exhibit first- or second-order desorption kinetics, while the former is based on zero-order kinetics. The bonding in multi-layers resembles that of a condensed solid of the pure adsorbate and the surface influence is almost non-existent. This results in a lower desorption temperature in relation to the monolayer.



## Chapter 3.

# Experimental techniques

It has always been a dream of many scientists to ‘see’ molecules and atoms. The invention of Quantum Mechanics (QM) and the new ideas on how Newton’s Classical Mechanics (CM) of the macroscopic world are confined and inapplicable to the subatomic world created an increased curiosity. It was not possible until the time that Binnig, Rohrer, Gerber, and Weibel proved the fantastic capability of the STM (Scanning Tunneling Microscope)<sup>[121–123]</sup> by resolving the structure of Si(111)–( $7 \times 7$ ) in 1983. Since this first discovery, for which Binnig and Rohrer received the Nobel Prize in 1986, the instrument has proved to be an extremely powerful tool for many disciplines in condensed-matter physics, chemistry, and biology. Local electronic structures at an atomic scale can be resolved on literally every kind of conducting surface.

Another important experimental probe for studying atomic and molecular structures is the interaction of electromagnetic radiation with atoms and molecules i.e. spectroscopy. The transition between vibrational levels accompanied by transitions between rotational energy levels is generally caused by the absorption of infrared (IR) radiation. The energy of IR is insufficient to excite electronic transitions. Infrared spectroscopy provides specific information on the types of bonds present in a molecule. It is non-destructive and does not require UHV. This property has made it a highly versatile investigation technique.<sup>[110,124]</sup>

### 3.1. Scanning Tunneling Microscopy

The concepts of physics were revolutionised<sup>[92]</sup> by experiments that concerned the radiation given off by heated black bodies, which is an idealisation for any radiating material

emitting and absorbing all energies. Although at low frequencies the experimental and theoretical data corresponded, at high frequencies a match could not be created. Max Planck was the first to offer a correct explanation for black body radiation in 1900. Planck made the revolutionary assumption that the oscillator energies were discrete and had to be proportional to an integral multiple of the frequency (equation (3.1)). This results in a quantisation of energy:

$$E = nh\nu \quad (3.1)$$

with the oscillator energy ( $E$ ),  $n$  an integer, Planck's constant ( $h = 6.6260755 \times 10^{-34} Js$ ) and the frequency ( $\nu$ ). Until then it was widely believed that the energies of electronic oscillators could have any value.

In 1905 Albert Einstein obtained the same value of  $h$ , but in a different experiment. He explained the photoelectric effect, which is the ejection of electrons from a metal surface by radiation. Planck's hypothesis was used and extended. Whereas Planck believed that once light was emitted, it behaved like a classical wave, the proposal of Einstein was that the radiation itself existed as small packets of energy. By using the conservation of energy argument the famous scientist showed:

$$E_k = \frac{1}{2}mv^2 = h\nu - h\nu_0 \quad (3.2)$$

with  $h\nu_0 = \phi$ ,  $m = \text{mass}$ ,  $v = \text{velocity}$  and  $\phi$  the work function of the metal, which is analogous to the ionisation energy of an isolated atom. This equation cannot be negative and thus the minimum frequency that will eject an electron, is the frequency to overcome the workfunction of the metal. This results in a threshold frequency  $\nu_0$ .  $\phi$  is usually expressed in electron volts (eV).

Sometimes light appears wave-like and particle-like (stream of photons) in some other instances. This is often referred to the *wave-particle duality of light*. In 1924 Louis de Broglie argued that if the behaviour of light is dual, the behaviour of matter could be dual too. He postulated, using results of Einstein's theory of relativity equation (3.3), that material particles should exhibit wave-like properties, like radiation possess particle-like properties. According to De Broglie both light and matter obey this equation.

$$\lambda = \frac{h}{p} \quad (3.3)$$

$$\lambda_{DeBroglie} = \frac{h}{mv} \quad (3.4)$$

with  $p$  and  $mv$  the momentum of, respectively, light and a particle. A similar situation arose when Werner Heisenberg formulated the Uncertainty Principle<sup>[125]</sup>, which states that location of a particle, within a distance  $\Delta x$ , e.g. electron, automatically an uncertainty in the momentum of the same particle is introduced. This was not consistent with Bohr's atom theory. The uncertainty is given in the following equation:

$$\Delta x \Delta p \geq h \quad (3.5)$$

If matter does possess wavelike properties, then that must be governed by a wave-equation subsequently. As a result of this hypothesis Erwin Schrödinger and Heisenberg independently formulated a quantum theory in 1925. Most of the times this theory is presented according to the method of Schrödinger, i.e. as a partial differential equation known as the Schrödinger equation. To find the wave function of a particle one needs to solve the Schrödinger equation. To derive the most simple version of this equation, one has to start with the classical 1D wave equation:

$$\frac{\partial^2 u}{\partial x^2} = \frac{1}{v^2} \frac{\partial^2 u}{\partial t^2} \quad (3.6)$$

with  $u$  the amplitude of the vibration at position  $x$  and the time  $t$  and  $v$  the speed at which a disturbance moves along the string. It can be solved via separation of variables and when  $u(x,t)$  is written as the product of a function of  $x$  and a harmonic function of time the following equation is obtained:

$$u(x,t) = \Psi(x) \cos(\omega t) \quad (3.7)$$

$\Psi(x)$  is the spatial amplitude of  $u(x,t)$ . When equation (3.7) is substituted in equation (3.6) the expression for the spatial amplitude is:

$$\frac{\partial^2 \Psi}{\partial x^2} + \frac{\omega^2}{v^2} \Psi(x) = 0 \quad (3.8)$$

with  $\omega = 2\pi\nu$  and  $\nu\lambda = v$  it gives:

$$\frac{\partial^2 \Psi}{\partial x^2} + \frac{4\pi^2}{\lambda^2} \Psi(x) = 0 \quad (3.9)$$



Now the matter waves of De Broglie are introduced. The kinetic energy plus the potential energy create the total energy of a particle:

$$E = \frac{p^2}{2m} + U(x) \quad (3.10)$$

with  $U(x)$  the potential energy. If equation (3.10) is solved for  $p = \sqrt{2m[E - U(x)]}$  then:

$$\lambda = \frac{h}{p} = \frac{h}{\sqrt{2m[E - U(x)]}} \quad (3.11)$$

Substitute the last equation in equation (3.9) and the result is the famous Schrödinger equation.

$$\frac{\partial^2 \Psi}{\partial x^2} + \frac{2m}{\hbar^2} [E - U(x)] \Psi(x) = 0 \quad (3.12)$$

with  $\hbar = h/2\pi$ . The solution of this equation,  $\Psi(x)$ , describes a particle of mass  $m$  moving in a potential field  $U(x)$ . It is a measure of the amplitude of the matter wave: the wave function of the particle. This form of the equation does not contain time and therefore it is called the *time independent Schrödinger equation*. The wave-functions obtained are called stationary wave functions. After rearranging the left side of equation (3.12) the Schrödinger equation can be formulated as an eigenvalue problem with the operator  $\hat{H} = -\frac{\hbar^2}{2m} \frac{d^2}{dx^2} + U(x)$ , which can be formulated as:

$$\hat{H}\Psi(x) = E\Psi(x) \quad (3.13)$$

Separation of variables are used to solve this differential equation, which gives the following general results ( $d_n = \text{constant}$ ):

$$\Psi(x) = d_1 e^{ikx} + d_2 e^{-ikx} \quad (3.14)$$

The above equation can also be expressed in a real function i.e. in absence of a magnetic field:

$$\Psi(x) = d_3 \cos(kx) + d_4 \sin(kx) \quad (3.15)$$

with wavevector:

$$k = \frac{\sqrt{2m(E - U)}}{\hbar} \quad (3.16)$$

In classical mechanics, an electron with energy  $E$  moving in a potential  $U(x)$  is described by equation (3.10) with  $m$  the electron mass  $9.1093897 \times 10^{-31}$  kg. In regions where  $E > U(x)$ , the electron has a nonzero momentum  $P_x$ . The electron cannot penetrate into any region with  $E < U(x)$ . This is the potential barrier. As mentioned before the state of the same electron is described by a wave-function  $\Psi(x)$ , this wave-function satisfies the Schrödinger equation. In case of a piecewise-constant potential  $E > U$  the solutions are given by equation (3.14). Hence the electron has a constant momentum  $P_x = \hbar k = [2m(E - U)]^{1/2}$  or a constant velocity  $v_x = p_x/m$  and is moving in a positive or negative direction. In the classical case this is similar. The following solutions in the classically forbidden region are obtained:

$$\Psi(x) = \Psi(0)e^{\pm\kappa x} \quad (3.17)$$

with the decay constant ( $E < U(x)$ ):

$$\kappa = \frac{\sqrt{2m(U - E)}}{\hbar} \quad (3.18)$$

This gives a description of the electron decaying in the  $\pm x$  direction. Observing an electron near a point  $+x$  is proportional to the following probability density:  $|\Psi(0)|^2 e^{-2\kappa x}$ . In the barrier region the value is nonzero and therefore there is a nonzero probability to penetrate a barrier. This elementary model<sup>[122]</sup> can be used to give an explanation of the basics of metal-vacuum-metal tunneling (Figure 3.1).

The minimum energy that is required to remove an electron from the bulk to the vacuum level is defined as the work function  $\phi$  of a metal surface. Generally this function not only depends on the material, but also on the crystallographic orientation of the surface. If thermal excitation is neglected the upper limit of the occupied states in a metal is the Fermi level ( $E_F$ ).  $E_F = -\phi$ . Further simplification requires assumption of equal work functions of both the tip and the sample. Tunneling is possible from tip to sample and vice versa. By applying a bias voltage a net tunneling current  $I$  occurs. A sample state  $\Psi_n$  with energy level  $E_n$  lying between  $E_F - eV$  and  $E_F$  has a chance to tunnel into the tip. When the work function value is much bigger than the bias

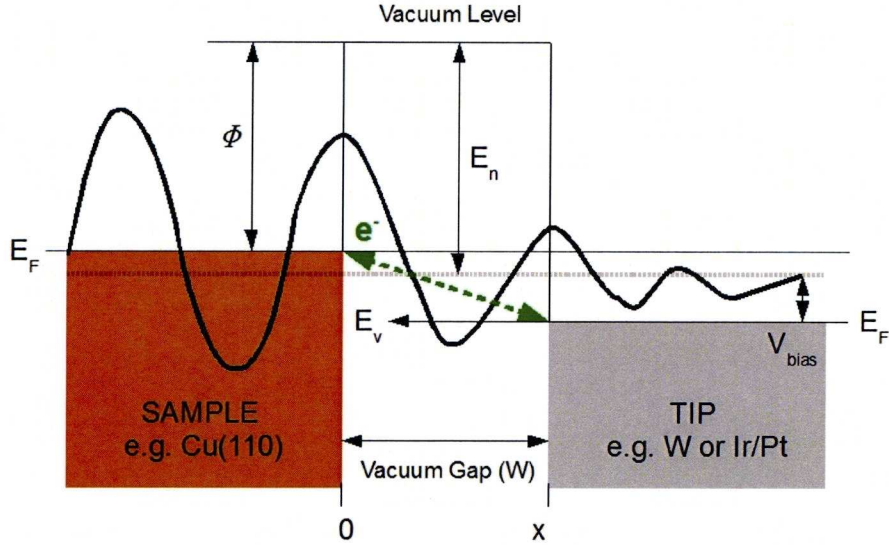


**Figure 3.1.** – Energy level diagram showing electron tunneling<sup>[110,122]</sup> (modified).

( $eV \ll \phi$ ) then all the sample state energy levels of interest are very close to the Fermi level  $E_n \approx -\phi$ . And thus the probability  $w$  to find an electron in the  $n^{th}$  sample state at the tip surface ( $x = W$ ) is:

$$w \propto |\Psi_n(0)|^2 e^{-2\kappa W} \quad (3.19)$$

with  $\Psi_n(0)$  indicating the value of the  $n^{th}$  sample state at the sample surface and:

$$\kappa = \frac{\sqrt{2m\phi}}{\hbar} = 0.51\sqrt{\phi} \quad (3.20)$$

with [ $\text{\AA}^{-1}$ ] as the unit of  $\kappa$ : the decay constant of a sample state near the Fermi level in the barrier region and [ $eV$ ] the work function unit.

The condition of the tip is usually invariable. The electrons flow with a constant velocity from the surface to the tip ( $x = W$ ). The tunneling current and the number of states on the sample surface within the energy interval [ $eV$ ] are directly proportional. This number depends on the local nature of the sample surface e.g for semiconductors and insulators this number is relatively small or zero. For metals it is finite and for semi-metals in between. By taking the energy interval [ $eV$ ] including all the sample



states the tunneling current is:

$$I \propto \sum_{E_n=E_F-[eV]}^{E_f} |\Psi(0)|^2 e^{-2\kappa W} \quad (3.21)$$

The sum in equation (3.21) can be written in terms of the local density of states (LDOS) at the Fermi level when  $V$  is small enough that the density of electronic states do not vary significantly within it. The LDOS is defined as the number of electrons per unit volume energy, at a given point in space and at a given energy. At energy  $E$ , the LDOS  $\rho_s(x, E)$ , for a sufficiently small  $\epsilon$  (voltage related), of the sample is defined according to:

$$\rho_s(x, E) \sim \frac{1}{\epsilon} \sum_{E_n=E-\epsilon}^E |\Psi_n(x)|^2 \quad (3.22)$$

The probability density for a specific state  $|\Psi_n|^2$  depends on the normalisation condition i.e. the integral over the entire space should be 1. The probability density of a single state decreases when the volume increases, but the number of states per unit energy increases, with a constant LDOS. Whether a surface is metallic or an insulator depends on the value of the LDOS near the Fermi level. The tunneling current can be expressed in the LDOS of the sample:

$$I \propto V \rho_s(0, E_F) e^{-2\kappa W} \approx V \rho_s(0, E_F) e^{-1.025\sqrt{\phi}W} \quad (3.23)$$

The typical value of decay constant  $\kappa$  is  $\approx 1.14 \text{ \AA}^{-1}$  for the typical value of  $\phi \approx 5 \text{ eV}$ . Therefore the current decays approximately 9.78 times per  $\text{\AA}$  (equation (3.24)).

$$T \equiv \frac{I(z)}{I(0)} = e^{-2\kappa z} \quad (3.24)$$

with  $T$  the transmission coefficient. The dependence of the tunneling current natural logarithm with respect to distance is a measure of the work function i.e. the tunneling barrier height.

$$\phi = \frac{\hbar^2}{8m} \left( \frac{d \ln I}{dW} \right)^2 \propto 0.95 \left( \frac{d \ln I}{dW} \right)^2 \quad (3.25)$$

An AC-voltage is used to vary the tip-sample distance through the  $z$ -piezo, the apparent barrier height can be measured experimentally by doing this. When applying

equation (3.17) at  $x = W$ , the sample wave-function becomes  $\Psi(W) = \Psi(0)e^{-\kappa W}$ . Then using equation (3.22) and the righthand-side of equation (3.21), which is proportional to the Fermi level LDOS of the sample at the tip surface it follows that:

$$\sum_{E_F-[eV]}^{E_F} |\Psi(0)|^2 e^{-2\kappa W} \equiv \rho_s(W, E_F)[eV] \quad (3.26)$$

And thus in this 1D case the tunneling current can be expressed as follows: equation (3.27), which should be approximately accurate if the lateral dimension of the tip end is much larger than the characteristic wavelength related to the decay constant i.e.  $2\pi/\kappa \approx 6\text{\AA}$ .

$$I \approx \rho_s(W, E_F)V \quad (3.27)$$

The current lines are almost perpendicular when the tip end radius is much bigger than than the distance between the tip and the sample surface. Assuming that the formula for the one-dimensional case (equation (3.23)) is followed by the tunneling current density then the lateral current distribution is:

$$I(\Delta x) = I_0 e^{\left(-2\kappa \frac{\Delta x^2}{2R}\right)} \quad (3.28)$$

The current concentrates in a small circle of radius  $14\text{\AA}$ , for  $R \approx 100\text{\AA}$  hence a relatively high lateral resolution is expected. In reality a spatial resolution of  $2\text{\AA}$ , is observed. Moreover, real space manipulation and control of individual atoms is possible via an active role played by tip-sample interactions.<sup>[122]</sup>

In STM tunneling there are roughly four regimes of interactions to be distinguished between tip and sample. Large ( $x_0 > 100\text{\AA}$ ). When applying an electrical field it is possible to induce field emission. Intermediate ( $10 < x_0 < 100\text{\AA}$ ). Wave functions on both the tip and the sample are distorted by attraction and a VdW-interaction is present. Short ( $3 < x_0 < 10\text{\AA}$ ). In this case electron transfer could occur. This exchange gives an attractive interaction and tunneling currents can be generated if a bias is applied. Extremely short ( $x_0 < 3\text{\AA}$ ). Short range repulsive forces dominate the scene, and if the tip is pushed even more towards the surface, tip and sample will show deformations.

The tunneling current can be calculated a few Ångströms from the outermost nuclei of the tip and the sample. The wave-functions of the bulk do not contribute to this, in contrast to the surface wave-functions of solids. Near the Fermi-level, surface states

usually dominate the surface charge density, they also have a strong influence on the tip and often prevail in the tunneling current. Tip material is often W or Pt/Ir that are d-band metals. These *d*-like tip states contribute to more than 90% of the tunneling current at low bias' situations. It has been observed that s and d-states dominate the DOS of the W-surface near the Fermi-level, while p-states could arise from an adsorbed foreign atom.

Shortly after the invention of STM it was noted that semiconductor-surface images depended significantly on the polarity and magnitude of the applied bias. A negative bias probes the LDOS occupied regions and thus the unoccupied regions are reflected by a positive bias. The density of states at bias energy and tip position,  $\rho_s(x, E)$ , are seen at constant current STM. Moreover STM provides surface site dependent spectroscopy i.e.  $dI/dV$  curves are proportional to the LDOS. The spatially averages spectrum approximates the density of states for the entire surface.<sup>[123]</sup>

The HOMO (highest occupied molecular orbital) is the molecular orbital, that according to the building-up principle is occupied last, whereas the LUMO (lowest occupied molecular orbital) is the next higher molecular orbital. These two orbitals jointly form the two frontier orbitals of a molecule and are of importance for many chemical and spectroscopic properties.<sup>[126]</sup>

## 3.2. STM - History of Development

The Topographiner, invented in 1972, is the precursor of the STM. It was the first successful attempt to create a metal-vacuum-metal tunneling<sup>[127]</sup> with a controllable gap.<sup>[128,129]</sup> This instrument is constructed of a W-tip. Presently, the most used tip-materials are W and Pt<sub>80</sub>/Ir<sub>20</sub>, the latter is relatively easy to prepare by cutting it with a well built clean sharp scissor under an acute angle while moving the scissors away from the wire. However, etching methods have been proposed too for W-<sup>[130]</sup>, Pt-<sup>[131]</sup>, Re-<sup>[132]</sup> and Au-tips<sup>[133]</sup>. The tip is spot-welded to a filament and subsequently attached to a mounting block. This block is fixed to *x* and *y* piezos<sup>1</sup>(lead-zirconate titanium ceramics), that drive a raster scan. Driven by the feedback circuit the sample is attached to the *z*-piezo. The distance between tip and sample surface is  $\approx 1300$  Å. A few +kV is applied on the sample and electrons flow to the sample surface i.e. field emission, which was explained in terms of quantum mechanics by Fowler and Nordheim in 1928.<sup>[122]</sup>

<sup>1</sup> The Curie-brothers discovered the Piezoelectric effect in 1880<sup>[122]</sup>



Topographic images of the sample surface were obtained using the field-emission current intensity as a feedback signal. The field emitter (tip) radius was typically  $1 \times 10^4 \text{ \AA}$ , corresponding to  $4 \times 10^3 \text{ \AA}$  in-plane first order resolution (emitter radius  $2 \times 10^3 \text{ \AA}$ ). Perpendicular to the surface a resolution of  $30 \text{ \AA}$  was achieved, with an inherent noise of  $3 \text{ \AA}$ . The topographic resolution is comparable to that of the Scanning Electron Microscope (SEM,  $1.5 \times 10^5 \text{ \AA}^2$ ). The main conclusion from experiments conducted with this equipment was, without doubt, that excellent mechanical decoupling of the tunneling unit from its surroundings is inevitable.

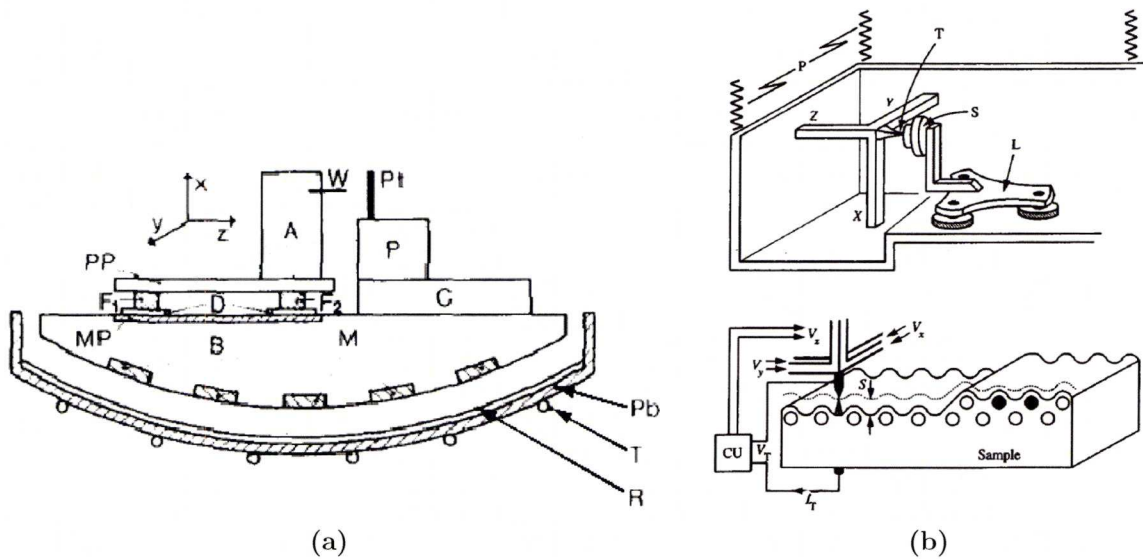


**Figure 3.2.** – (a) Schematic representation of the first STM.<sup>[134]</sup> (b) Mechanism scheme of a standard tripod STM. **Top:** Louse (L), tip (T), Vibrational suspension (P). **Bottom:** Constant current mode. A voltage  $V_z$  is applied to the  $z$ -piezoelectric element via a control unit (CU), while  $V_x$  and  $V_y$  are altered. The tip-trace ( $dz$ -scan) resembles the surface topography of sample S. In the other mode: constant height i.e. keeping  $dz$  constant, a  $dI_T$  scan is obtained to resemble the topography (in fact changes in  $W(\phi)$  by protrusions). Two surface atoms have a negative charge excess.<sup>[110,135]</sup>

Binnig, Rohrer, Gerber and Weibel used static magnetic levitation to achieve the decoupling.<sup>[134,136]</sup> Figure 3.2 represents a schematic representation. They mounted the unit on strong permanent magnets (M) levitating on a super-conducting bowl of Pb (super-insulated). Liquid He was used for cooling and circulates in tubes (T). An efficient eddy-current damper was made by a normal conducting sheet (R) between the lead and the magnets. In later versions viton dampers were used.<sup>[135]</sup> The tunneling unit consists of a platinum (Pt) plate with tungsten (W) tip, which is fixed to a support (A) and in turn can semi-continuously travel in any direction on the bench (B). The driving mechanism is a piezo-plate (PP) that sits on metal feet (F) attached to a metal plate

(MP). Insulation is achieved via a high dielectric-constant material (D). The coarse approach, the so called ‘Louse’ (L) is realised via piezo contraction or elongation with an appropriate clamping sequence (100 to 1000 V) of the feet, which moves A in steps down to 100 Å. Fine control ( $dz, dx, dy$ ) is realised via piezo-drive (P) with movements up to a few thousands Å with 3 Å/V sensitivity. Tip and plate were separated 10 Å from each other and could be stabilised within 0.2 Å.<sup>[137]</sup> This results in a relatively high resolution of  $1 \times 10^3 \text{ Å}^2$ . Apart from 0.06 mm diameter electrical leads all mechanical contact is avoided, which ensures thermal decoupling too. The device operated at  $T_{room}$ .

A higher degree of vacuum logically generated a more clean tip and plate and hence a better resemblance of the work function with the theoretical one (3.2 eV vs 5.0 eV). The first results were obtained from (110) surfaces of CaIrSn<sub>4</sub> and Au<sup>[137]</sup>, and a year later they showed the  $(7 \times 7)$  reconstruction of Si(111).<sup>[138]</sup> The work function, which is contamination sensitive, remained constant for a period of ten minutes. Repeated tip cleaning by applying 10 V at 10 kHz stabilised  $\phi$ . Nowadays many other cleaning methods are used to create a tip-apex’ capable of delivering atomic resolution. These are: direct resistive annealing, annealing by electron bombardment, self-sputtering with noble gas ions, by field emission<sup>[139,140]</sup> or controlled collision.<sup>[122]</sup>

### 3.2.1. Tubular Scanners

As can be concluded from the previous section, the first STM systems developed used a tripod ( $dx, dy, dz$ ) for fine-positioning of the tip. Although stability problems still existed these STM-systems were very sophisticated in comparison to the Topografiner. The tip-to-sample distance, which occurs at the sub-Ångström scale is the reason for this destabilisation, for the STM is build with elements in the centimetre range. This discrepancy in the order-of-magnitude cause the complete system to be relatively susceptible to vibrations and thermal drift. In order to achieve an even more stable STM, the next step was the development of a single tubular piezo scanner by Binnig and Smith in 1986.<sup>[141]</sup> This single tubular piezo is split into four equal outside segments and an inner segment. When a piezo polarisation dependent voltage is applied on a single outside electrode, the segment expands accordingly i.e. perpendicular to the electric field. As a result the tube bends. Applying a voltage to the single inside electrode gives uniform expansion,  $z$ -motion. Orthogonal  $x, y$ -motion is generated by controlling voltages on two electrodes that are  $\pi/2$  rad separated (Figure 3.3a). By applying a high DC-voltage, a large amplitude offset can be generated with the aid of the remaining electrodes oth-

erwise they can be grounded. The displacement of the piezo is given in the following equation:

$$\Delta_{x(1),y(2),z(3)} = d_{31}V\frac{L}{h} \quad (3.29)$$

when the directions  $x, y$  and  $z$  are labelled as 1, 2 and 3 respectively and with the piezocoefficient (pm/V) defining the ratio of the strain component versus field intensity:

$$d_{31} \equiv \frac{S_1}{E_3} \quad (3.30)$$

which consists of the straintensor (S) and the field intensity (E)

$$S_1 \equiv \frac{\delta x}{x} \quad E_3 = \frac{V}{z} \quad (3.31)$$

with  $V$  the applied voltage,  $L$  the length and  $h$  the thickness of the piezo. The Piezo-constant is proportional to  $L/h$  and the resonance frequency to  $h/L^2$ . This shows that length reduction of the piezo will increase the resonance frequency, with the depolarising field of the material as the limiting factor. The special properties of the piezo ceramics are generated by a polarisation process and if a strong field generated in another direction is then applied, the piezoelectricity is lost.<sup>[122]</sup>

Tubular scanners are preferred above tripod scanners. They have a greater range and a higher resonance frequency parallel to the tube axes (5 kHz vs. 40 kHz, stretching mode) and hence perpendicular to the sample surface. It results in faster scanning speeds and better vibrational resistance. The small size and hence a small volume of the whole cylinder ( $\approx 250 \text{ mm}^3$ ) decreases the order of magnitude discrepancy, which subsequently gives a smaller noise transfer via the system. Also  $x, y$ -thermal drift is avoided due to the symmetry of the tube, with the requirement that the tip is mounted symmetrically too.

In 1988 the single tubular scanner was further refined by Flemming Besenbacher, Erik Laegsgaard and Ivan Stensgaard who developed the next generation of the compact STM: the double-tubular scanner.<sup>[142,145]</sup> The present state of the art double tubular STM-scanner designed by Besenbacher *et al.* is shown in Figure 3.3. The inner tube resonance frequencies are 100 kHz (stretching mode) and 60 kHz (bending mode), which are due to the relatively small size ( $\approx 83 \text{ mm}^3$ ). Tip-motion in the  $x, y, z$ -directions



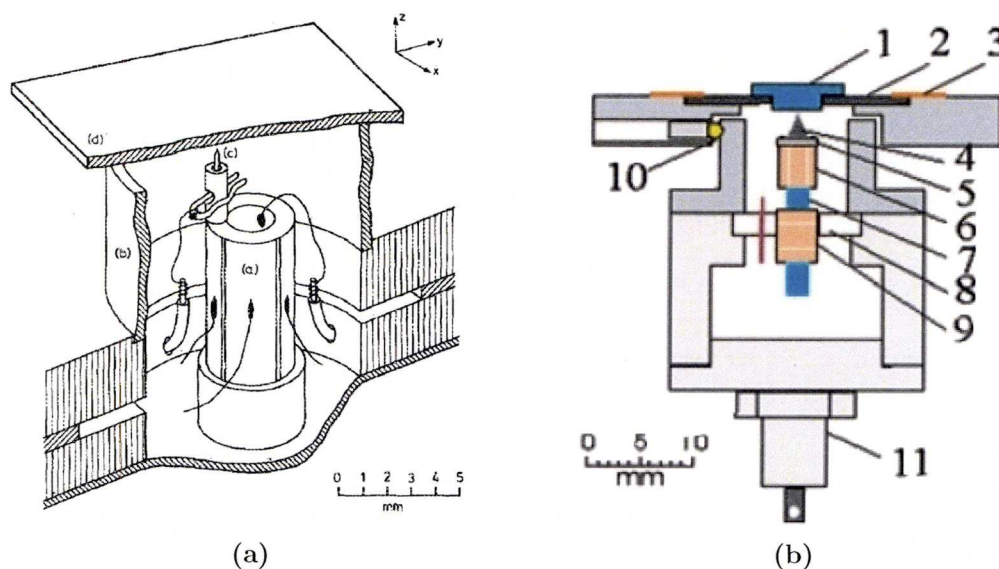


**Figure 3.3.** – (a) Schematic representation of a double tubular scanner: (a) inner piezo, split into four segments. (b) outer piezo, (c) W-tip (d) target placed on the outer tube.<sup>[142]</sup> (b) 2D schematics of the variable temperature (90-400K) Specs STM 150 Aarhus scanner head: (1) sample (2) sample holder (3) clamps (4) tip (5) tip holder (6) scanner tube (7) approach motor rod (8) motor mount (9) approach motor (10) quartz balls (electrically and thermal insulation (11) zener diode (used for counterheating the STM body during cooling)).<sup>[143–145]</sup>

is generated via this tube ( $dz \approx 1.6$  nm/V and  $dx, dy \approx 4.0$  nm/V). The resonance frequency for the other tube supporting the sample is 95 kHz. The properties implicate high scan rates. The sample is placed in a Ta-holder. A ceramic (macor) holder, which is glued to the top of the scanner, fixes the tip. A rod together with a segmented piezo-tube (Inchworm®) is glued (epoxy) to the scanner tube, which forms a small motor for coarse approach.

The Inchworm®, which was first patented by K.Hsu in 1966<sup>[146]</sup>, is the most successful successor of the Louse. An alumina shaft is slid inside a piezo, which has three sections. Sequential section activation result in axial motion in small steps down to 2 Å. After the birth of the STM primitive screws were used for the coarse approach. Nowadays this is performed automatically and the feedback loop needs to be inactivated and activated subsequently. Explanation for this is the following: The current needs to be amplified for the tunneling current in STM is relatively small (10 pA to 50 nA). After first amplification the output of a logarithmic amplifier is compared with a reference voltage and a set point for the tunneling current is set after which the error signal is processed by the feedback circuit. Subsequently the output sends a voltage to the z-piezo. If the tunneling current is larger/smaller than the preset current, the z-piezo

voltage retracts the tip from the sample or respectively approaches it. This is a negative feedback sequence. During the approach the feedback loop needs to be inactivated to make it possible to retract the  $z$ -piezo to the limit and to use the coarse approacher to take a step. Then activation of the loop results in either a tunneling current and stabilisation of the tip or no signal at all. In the latter case the automatic approach loop is repeated until tunneling occurs.<sup>[122]</sup> Subsequently, bias ( $\pm 2\text{mV} < V_{\text{bias}} < \pm 2\text{V}$ ) dependent tunneling can be established, which result in electron transfer from tip to sample( $+_{\text{bias}}$ ) and vice versa( $-_{\text{bias}}$ ).<sup>[145]</sup> The feedback loop results in an equilibrium  $z$ -position. When the tip scans parallel to the plane of the sample ( $dx$ ), the contour height  $z$  changes with time too.

### 3.3. InfraRed Spectroscopy

Infrared rays were discovered by Herschel in 1800.<sup>[147]</sup> Ångström and Julius<sup>[148–150]</sup> were the first to obtain absorption spectra of organic compounds in the period 1889 to 1892. Both used a bolometer and rock salt prism and lenses. A few years later in 1895, Merritt also did pioneering work on the infrared absorption of crystals dependent on the plane of polarization of the incident waves.<sup>[151]</sup> An schematic of his experimental setup is shown in Figure 3.4. After the development of quantum mechanics, Herzberg applied this to the spectroscopic world.<sup>[152]</sup> The German became the founder of modern molecular spectroscopy and was awarded the Nobel Prize in Chemistry in 1971. Herzberg and his coworkers spectroscopically determined the C-C bond distance from the infrared spectrum of the polyatomic molecule methylacetylene in 1936.<sup>[153]</sup> More than twenty years later IR studies of CO chemisorption on different metal surfaces were performed<sup>[154,155]</sup> and the first foundations of Reflection Absorption Infra Red Spectroscopy(RAIRS) were created.

The vibration of a molecule appears as  $N_{\text{vib}}$  independent harmonic oscillators (HO), with each its own characteristic frequency ( $\nu$ ) without degeneracies. The HO accounts for the infrared spectrum (respectively rotational and vibrational part) of a diatomic system. Therefore it gives a good representation of a vibrating linear diatomic molecule ( $N_{\text{vib}} = 1$ ) at  $T_{\text{room}}$ . The accompanying Schrödinger equation for a HO is:

$$-\frac{\hbar^2}{2\mu} \frac{d^2\Psi}{dx^2} + V(x)\Psi(x) = E\Psi(x) \quad (3.32)$$

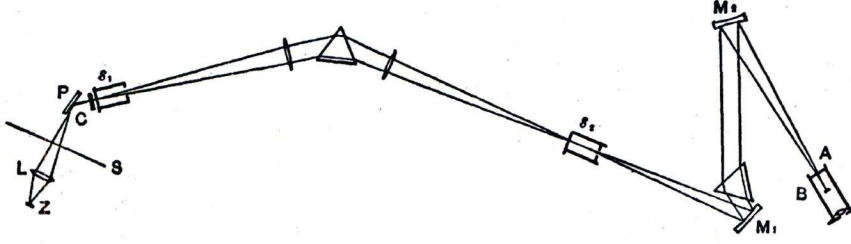


**Figure 3.4.** – A zirconium lamp ( $Z$ ) produces rays that fall upon a rock salt lens ( $L$ ), and after reflection at polariser ( $P$ ) were brought to focus at the slit of the first spectrometer ( $S_1$ ). Subsequently the obtained spectrum falls on the next spectrometer ( $S_2$ ) via a fluorite prism and two other lenses.  $M_1$  and  $M_2$  are concave mirrors. A linear bolometer ( $B$ ) was mounted at the crosshair of the observing telescope, which together form the analyser ( $A$ ). The crystal was placed in front of the first slit and after screen ( $S$ ), that was used to observe the throw of a galvanometer.<sup>[151]</sup>

with the reduced mass  $\mu = (m_1 m_2) / (m_1 + m_2)$  and  $V(x) = \frac{1}{2} k x^2$ , with force constant  $k$  and energy levels:

$$E_v = \hbar \sqrt{\frac{k}{\mu}} \left( v + \frac{1}{2} \right) = h \nu \left( v + \frac{1}{2} \right) \quad (3.33)$$

with  $v=0,1,2,\dots$  and  $\Delta E = h \nu_{\text{observed}}$ . Only transitions between adjacent energy states are allowed, which implicate the following selection rule:  $\Delta v = \pm 1$ . Absorption occurs when  $\Delta v = +1$  and hence:

$$\Delta E = E_{v+1} - E_v = \hbar \sqrt{\frac{k}{\mu}} \quad (3.34)$$

with frequency:

$$\tilde{\nu}_{\text{observed}} = \frac{1}{2\pi c} \sqrt{\frac{k}{\mu}} \quad (3.35)$$

now a vibrational term  $G(v)$  can be introduced, with  $c$  the speed of light and  $\tilde{\nu}$  in wavenumbers [ $\text{cm}^{-1}$ ].

$$G(v) = \tilde{\nu} \left( v + \frac{1}{2} \right) - \tilde{X}_e \tilde{\nu} \left( v + \frac{1}{2} \right)^2 + \dots \quad (3.36)$$



$\Delta E$  is similar for all allowed transitions and hence the IR-spectrum consists of one line, which is called the fundamental vibrational frequency. The energy of the ground state is  $\frac{1}{2}h\nu$ , which is a direct result of the uncertainty principle.<sup>[92]</sup> The above equations do not consider the overtones that also arise in a vibrating diatomic molecule. This requires a more refined equation and insertion of the anharmonicity constant  $\tilde{X}_e$ <sup>[92]</sup> for which the  $\Delta v$  selection rule can have any integral value.

If  $N_{vib} > 1$  the Schrödinger equation becomes extremely complex to solve. This can be circumvented by the use of normal coordinates or normal modes  $(F_p, Q_p)$ , with  $p$  the energy level, resulting in the following Hamiltonian:

$$\hat{H} = \hat{H}_{vib,p} = \sum_{p=1}^{N_{vib}} \frac{-\hbar^2}{2\mu_p} \frac{d^2}{Q_p^2} + \frac{1}{2} F_p Q_p^2 \quad (3.37)$$

with  $v_p=0,1,2,\dots$  and the energies:

$$E_{vib} = \sum_{p=1}^{N_{vib}} h\nu_p \left(v_p + \frac{1}{2}\right) \quad (3.38)$$

Apart from the above mentioned selection rule in  $\Delta v$ , to be IR-active during vibration the diatomic molecule must have a permanent dipole moment too. This selection rule is based on the transition dipole moment ( $\eta$ ). Suppose the dipole moment of a diatomic molecule is created by two partial charges  $\pm\delta q$  separated by a distance  $R = R_e + x$  ( $R_e$  is the equilibrium-radius at the minimum of the potential curve), then the variation with displacement from the equilibrium separation can be written as:

$$\eta = R\delta q = R_e\delta q + x\delta q = \eta_0 + x\delta q \quad (3.39)$$

$\eta_0$  the electric dipole moment operator in equilibrium separation of the nuclei and when  $p \neq p+1$ , this results in the following bracket notation:

$$\langle v_p | \eta | v_{p+1} \rangle = \eta_0 \langle v_p | v_{p+1} \rangle + \delta q \langle v_p | x | v_{p+1} \rangle \quad (3.40)$$

since the term  $\eta_0 = 0$  (states with different values of  $v$  are orthogonal) and  $\delta q = d\eta/dx$  it gives:

$$\langle v_p | \eta | v_{p+1} \rangle = \langle v_p | x | v_{p+1} \rangle \left( \frac{d\eta}{dx} \right) \quad (3.41)$$

From this last equation it can be concluded that the right part is zero unless the dipole moment varies with displacement i.e. the gross selection rule for vibrational spectroscopy. Further examination of  $\langle v_p | x | v_{p+1} \rangle$  with the assistance of Hermite polynomials ( $N, H$ ) and with  $x = \alpha y$ ,  $\alpha = (\hbar^2 / \eta \omega^2 \mu)^{1/4}$  results in the specific selection rule ( $\Delta v = \pm 1$ ). In short: during the normal mode motion the dipole moment of the molecule must vary. And a normal mode is an independent, synchronous composite motion of simultaneous stretching and bending of atom(s)(groups) bonds that may be excited without leading to any other normal mode excitation. And each normal mode behaves like an independent harmonic oscillator.<sup>[68]</sup>

Generally the vibrational transition is accompanied by a rotational transition when a molecule absorbs infrared radiation; pure rotational transitions occur in the microwave regime.

### 3.4. Reflection Absorption Infra Red Spectrometry

Although the first attempts to perform RAIRS were already made in the years 1956<sup>[154]</sup> and 1959<sup>[155]</sup>, these experiments suffered from inadequate absorption intensity, even with multiple reflections. A decade later Greenler<sup>[156,157]</sup> and McIntyre and Aspnes<sup>[158]</sup> independently proposed a more sophisticated method of acquiring the correct intensity by using the following model (Figure 3.5), whose fundamentals had been created by Francis and Ellison.<sup>[159]</sup>

Surface coverage, film thickness, wavelength and the dielectric constants of the ambient (vacuum), adsorbate layer (film) and substrate phases relate to the reflectivity change that is produced by the formation of an adsorbate layer on a substrate surface. Calculation of metal reflectivity covered by a thin adsorbing layer is a boundary value method problem, which can be solved by commencing with the wave equation solution that describes the propagation of a plane electromagnetic wave<sup>2</sup> through a medium.

$$E(r, t) = E_n e^{i\omega t - \kappa r} \quad (3.42)$$

with  $(t)$  and  $(r)$  respectively time and the position vector  $(r)$  referring to an arbitrary coordinate system and  $\kappa$  the wave-vector,  $\omega$  the angular frequency. The ratio of two

---

<sup>2</sup> A beam of monochromatic, plane polarised radiation or transverse wave, called p-polarised ( $\parallel$ ) when the electric field is parallel to the surface and s-polarised ( $\perp$ ) when it is perpendicular

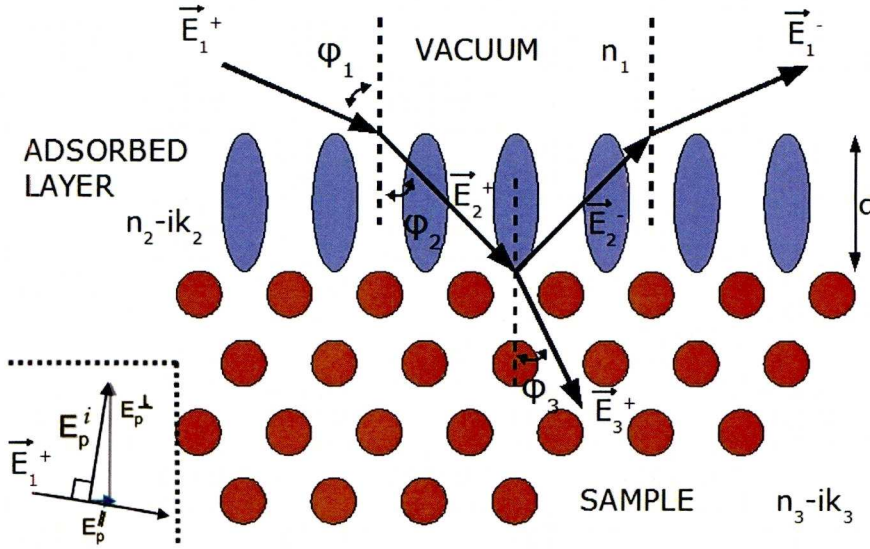


**Figure 3.5.** – Three-phase boundary value problem model.  $E_n^\pm (n = 1, 2, \dots)$  is the electromagnetic wave (sum of all the multi-reflected waves in that layer).  $d$  is the adsorbate layer thickness.  $\varphi_n$  the angle of incidence (+) or reflection (-).<sup>[156]</sup> (modified) Inset: the magnitude of the p-component of the electric field vector.<sup>[47]</sup>

contiguous phases complex amplitudes of the reflected and incident wave electric-field vectors are described by the Fresnel reflection coefficient. This is a function of incident beam polarisation and angle of incidence. The angular-dependent quantity  $\xi_j$  is defined by:

$$\xi_j = \hat{n}_j \cos \varphi_j = \sqrt{\hat{n}_j^2 - n_1^2 \sin^2 \varphi_1} \quad (3.43)$$

with  $\varphi_1$  and  $n_1$  the real angle of incidence, respectively real refractive index of the transparent ambient phase. Whereas  $\hat{n}_j$  and  $\varphi_j$  are respectively the complex refractive index of phase  $j$  and the complex angle.  $\hat{n}_j$  on its turn can be divided in a real and complex part too. If time dependency is taken as  $e^{+i\omega t}$  and the extinction coefficient  $k_j \geq 0$  then  $\hat{n}_j = n_j - ik_j$ .

The Fresnel coefficients for a interface between two phases  $(j, q)$  for respectively perpendicular and parallel polarised radiation are:

$$r_{\perp jq} = \frac{\mu_q \xi_j - \mu_j \xi_q}{\mu_q \xi_j + \mu_j \xi_q} \quad (3.44)$$

$$r_{\parallel jq} = \frac{\hat{\varepsilon}_q \xi_j - \hat{\varepsilon}_j \xi_q}{\hat{\varepsilon}_q \xi_j + \hat{\varepsilon}_j \xi_q} \quad (3.45)$$



where,  $\varepsilon$  is the dielectric constant and  $\mu$  is the magnetic permeability. If  $\varphi = 0$  (normal incidence) then  $r_{\perp jq} = r_{\parallel jq}$ .

In general, the thickness of the adsorbed layer is much less than the wavelength of the incident radiation i.e.  $d \ll \lambda$ , which makes it possible to use first-order (linear) approximation methods, which ignores phase changes on reflection. From this it is possible to calculate the reflectivities  $R(0)$  of the bare surface and  $R(d)$  of the covered surface and their ratio to give:

$$\frac{R_{\perp}(d)}{R_{\perp}(0)} = 1 + \frac{8\pi dn_1 \cos \varphi_1}{\lambda} \text{Im} \left( \frac{\mu_3 \hat{\varepsilon}_2 \cos^2 \varphi_2 - \mu_2 \hat{\varepsilon}_3 \cos^2 \varphi_3}{\mu_3 \varepsilon_1 \cos^2 \varphi_1 - \mu_1 \hat{\varepsilon}_3 \cos^2 \varphi_3} \right) \quad (3.46)$$

and for parallel polarisation:

$$\frac{R_{\parallel}(d)}{R_{\parallel}(0)} = 1 + \frac{8\pi dn_1 \cos \varphi_1}{\lambda} \text{Im} \left( \frac{\mu_2 \hat{\varepsilon}_3 \cos^2 \varphi_2 - \mu_3 \hat{\varepsilon}_2 \cos^2 \varphi_3}{\mu_1 \hat{\varepsilon}_3 \cos^2 \varphi_1 - \mu_3 \varepsilon_1 \cos^2 \varphi_3} \right) \quad (3.47)$$

These results can be expressed in terms of the normalised reflectivity change which is determined experimentally by the absorption factor ( $A$ ). This is a measure of the depth of an infrared absorption band. In the optical frequency range  $\mu_1 = \mu_2 = \mu_3 = 1$  the following expressions are obtained:

$$A = \frac{\Delta R}{R} = \frac{R(d) - R(0)}{R(0)} \quad (3.48)$$

$$A_{\perp} = \frac{\Delta R_{\perp}}{R_{\perp}} = \frac{8\pi dn_1 \cos \varphi_1}{\lambda} \text{Im} \left( \frac{\hat{\varepsilon}_2 - \hat{\varepsilon}_3}{\varepsilon_1 - \hat{\varepsilon}_3} \right) \quad (3.49)$$

$$A_{\parallel} = \frac{\Delta R_{\parallel}}{R_{\parallel}} = \frac{8\pi dn_1 \cos \varphi_1}{\lambda} \text{Im} \left( \left( \frac{\hat{\varepsilon}_2 - \hat{\varepsilon}_3}{\varepsilon_1 - \hat{\varepsilon}_3} \right) \left[ \frac{1 - (\frac{\varepsilon_1}{\hat{\varepsilon}_2 \hat{\varepsilon}_3})(\hat{\varepsilon}_2 + \hat{\varepsilon}_3) \sin^2 \varphi_1}{1 - (\frac{1}{\hat{\varepsilon}_3})(\varepsilon_1 + \hat{\varepsilon}_3) \sin^2 \varphi_1} \right] \right) \quad (3.50)$$

It can be concluded that the angle at which high absorption intensity and hence high sensitivity can be obtained depends on the optical constants ( $n, k$ ) of the concerning phases and  $d/\lambda$ . Both Greenler and McIntyre found that the greatest sensitivity can be obtained by using p-polarised light at grazing angles viz.  $A_{\perp} \ll A_{\parallel}$  at all angles of incident (Figure 3.5 inset). Grazing incident geometry lead to increased path length's and hence increased sensitivity for the adsorbate layers. Moreover  $\sum \vec{E}_{\parallel}$  (the resultant electric vector for radiation polarised parallel to the plane of incidence) is predominantly

perpendicular to the metal surface. This results in the surface vibrational spectroscopy surface selection rule for metal surfaces:<sup>3</sup>

*Molecular vibrations whose change in electric dipole is parallel to the surface will be less strongly excited or in other words: only molecular vibrations that result in a dynamic dipole moment  $\perp$  surface will be active in IR and show absorption.*<sup>[110,156]</sup>

Apart from the sensitivity, the surface reflection number is also important for maximizing reflection absorption band depth. The reflected radiation background intensity reduced to 37% ( $= 1/e \times 100\%$ ) of its initial value is the optimum number of reflections ( $N$ ).<sup>[157,161]</sup> Assuming that noise is the limiting factor, optimising the signal-to-noise ratio by maximising  $\Delta(R)$ <sup>[162,163]</sup> gives the optimal  $N$  (equation (3.53)).

$$\Delta R = R(0)^N - R(d)^N \quad (3.51)$$

after  $dN/dR = 0$

$$N = \ln \left[ \frac{\ln R(0)}{\ln R(d)} \right] \quad (3.52)$$

in case of weak absorption<sup>[164,165]</sup>  $\lim_{R(d) \rightarrow R(0)} A = 0$  then  $R(0)^N = e^{-1}$  and:

$$N = \frac{-1}{\ln R(0)} \quad (3.53)$$

As can be concluded from Figure 3.6 the optimal number of reflections depend on  $R(0)$ , which in turn depends on the optical constants (which vary with frequency) of the metal substrate. Moreover it also depends on the angle of incidence ( $\varphi$ ). For a good reflector ( $R(0)$  high) a gain can be achieved by using many reflections before the background drops. In contrast in case of a poor reflector (low  $R(0)$ ) few reflections should be used.<sup>[162]</sup> The determination of the number of reflections, which are desirable at different incident angles is fundamental to an instrument of reflection spectroscopy. However, it should be noted that even for a good reflector, 60% of the optimum signal can be obtained with a single reflection, therefore, generally the RAIRS experiment is carried out in single reflection mode.

<sup>3</sup> Although for modes at low frequencies obtained with synchrotron radiation sources there may be exceptions.<sup>[160]</sup>

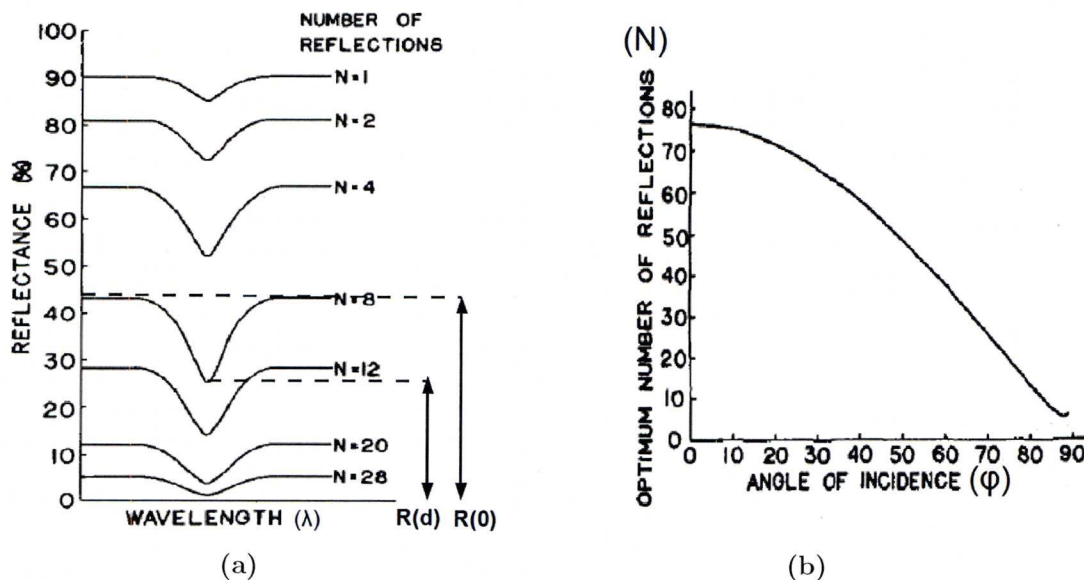


**Figure 3.6.** – **a.** Reflectance values from varying number of reflections numbers from the same surface resulting in hypothetical Reflection-Absorption spectra, for the maximum number of reflections ( $N=8$ ),  $\Delta(R)$ , defined as the depth of an absorption band with respect to the background is presented. Modified<sup>[162]</sup> **b.**  $N$ , the optimum number of reflections at different angles of incidence ( $\varphi$ )  $n_1 = 1.0, n_2 = 1.3$  which represents an adlayer of  $\approx 5\text{\AA}$  thickness with a moderately strong band,  $k_2 = 0.1$  on a metal ( $n_3=3.0, k=30.0$ )  $d/\lambda=0.0001$ <sup>[157]</sup>

### 3.5. RAIRS - History of Development

Until approximately 1985 almost all RAIRS studies were performed with diffraction grating based IR-spectrometers. In the late 1980s these were replaced by commercial FT(Fourier Transform)-IR instruments, that are still used to date. The advantages of FT-IR are best noticed when a high resolution over a wide spectral range is desired.<sup>[166,167]</sup>

Sensitivity problems were always the main issue to improve. And thus there has always been a quest to improve the signal to noise ratio( $S/N$ ) for a RAIRS system, which is very sensitive to noise that can be generated by virtually every part of the setup<sup>[163,165]</sup>. A typical RAIRS setup is shown in (Figure 3.7).

The most important component is the infrared source or thermal emitter i.e. black-body. Generally emitters consist of silicon carbide (SiC) or a mixture of zirconium and yttrium oxides. These are respectively Globars and Nernst Glowers. Popular in RAIRS applications are the more stable Globar glowers that typically operate at  $\approx 1700\text{ K}$ , which is a resistively heated rod ( $4 \times 25\text{ mm}$ ) mounted in a watercooled housing.<sup>[165,169]</sup>



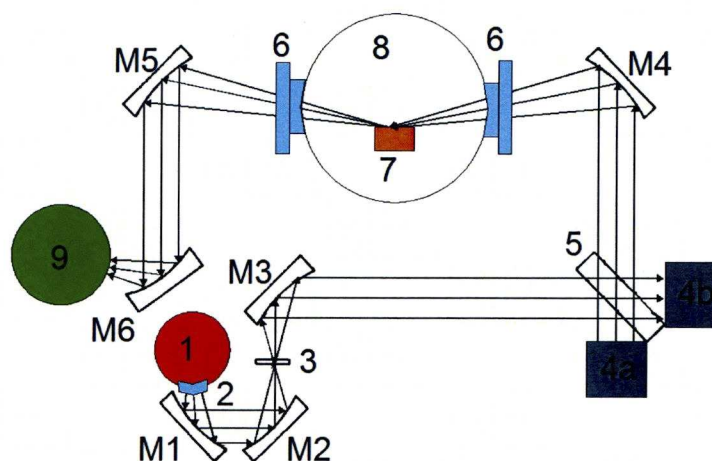


**Figure 3.7.** – A schematic diagram of a typical RAIRS-optics setup. IR-source (1) radiation from an emitter travels through a polariser (2) and is focused by mirrors (M1) and (M2). It continues via a variable iris aperture (3) to mirror (M3) to form a collimated beam, that is directed into an interferometer. This is composed of a KBr-beam-splitter (5) and fixed (4a) and moving (4b) cube corner mirrors. Then the beam travels via an off-axes paraboloidal mirror (M4) and an alkali-halide window (6) onto the sample (7) in the UHV chamber (8). The reflected beam passes via another alkali-halide window and mirror (M6) and is focused onto a detector (9). The spectrometer and detector housing are usually purged with nitrogen gas to minimise the contribution of atmospheric water vapour and carbon dioxide to the spectrum. Taken from<sup>[168]</sup> and modified.

However nowadays also a state of the art high temperature (2300 K) graphite<sup>[170]</sup> and Permaglow®<sup>[171]</sup> sources<sup>4</sup> have been developed. These achieve increased sensitivity, while satisfying all other demands. Other e.g. high temperature (10000 K) Arc sources are available, but these suffer from instability and a lack of total spectrum coverage.

The energy radiated per unit area at a wavelength  $\lambda/\Delta\lambda$  is described by Planck's blackbody radiation formula:<sup>[163,172]</sup>

$$E_{bb}\Delta\lambda = \epsilon(\lambda) \frac{2\pi hc^2}{\lambda^4} \left[ e^{\frac{hc}{\lambda k_B T}} - 1 \right]^{-1} \frac{\Delta\lambda}{\lambda} \quad (3.54)$$

with  $k_B$  the Boltzmann constant,  $\epsilon(\lambda)$  the emissivity, which is unity for an ideal black body. From the above equation it can be concluded that it is essential to use temperatures where the emitted energy is maximised, especially since the magnitude of noise in FT-IR is independent of the magnitude of the signal. Increases in signal improve S/N. Hence it is obvious that the sensitivity of RAIRS can be enhanced by increasing the

<sup>4</sup> Permaglow® is a synthetic super luminescent crystal composed of aluminum oxide, strontium oxide, calcium oxide, europium oxide and boron oxide. U.S. Pat. No. 6177029.

source intensity. Moreover the spectral distribution drops sharply when reaching higher wavelengths, especially by wavenumbers  $<1000\text{cm}^{-1}$ . Different sources are available to circumvent this e.g. IR-lasers are known to operate in the  $300\text{-}3000\text{cm}^{-1}$  region and IR-synchrotron radiation (relatively brighter at  $<1000\text{cm}^{-1}$ , which is already polarised in the plane of the orbit and consist of a small bright source (small divergence)).<sup>[163,169,170,173]</sup>

The second important component that improves S/N is the interferometer. Before the use of FT-IR,<sup>[165]</sup> the IR-spectrum was obtained by using a monochromator (diffraction gratings) with double-beam (two physically separate beams) modulation techniques applied as a suppressor of residual noise.<sup>[169]</sup> The invention of FT-IR made this redundant, unless non-broadband (narrow) spectra are required.<sup>[163]</sup> Radiation containing all wavelengths is split into two beams via a beamsplitter. One beam path is of fixed length, the other of variable length via a movable mirror. A sequence of constructive and destructive interferences is obtained via this i.e. an interferogram which can be converted by Fourier transformation from the time domain into one spectral point on the frequency domain. A full IR-spectrum can be generated by smooth and continuous adjustment of the movable mirror position and all points can be Fourier Transformed simultaneously, which improves the S/N ratio dramatically. In contrast to diffraction gratings the entire radiation range is passed through the sample simultaneously, which allows high throughput plus rapid acquisition. Resolution capabilities are enhanced by the possibility of executing multiple scans ( $D$ ) to enable good S/N spectra to be collected.<sup>[174]</sup> Although noise levels generally are found to be inversely proportional to  $\sqrt{D}$ , for relatively large number of scans the gain flattens out. Moreover at longer acquisition times background gases have more time to interfere. And finally it is inevitable that changes in spectral response may arise.

The third component that is crucial for the optimisation of S/N is the detector, which has to measure absorption changes that are as small as 0.1%. Griffiths and De Haseth<sup>[170]</sup> proposed the following expression for the S/N of an FT-IR, which is only valid for systems when  $N_{\text{detector}} > N(\Sigma_{\text{othersources}})$ :

$$\frac{S}{N} = \frac{U_v(T)\theta\Delta v t^{1/2}\eta}{NEP} \quad (3.55)$$

with  $U_v(T)$  [ $\text{W}/\text{cm}^2\text{ sr cm}^{-1}$ ] the spectral energy density of the source,  $T$  is the operating temperature,  $v$  the wavenumber,  $\theta$  [ $\text{cm}^2\text{ sr}$ ] is the total throughput of the system,  $\Delta v$  the spectral resolution,  $t$  the time in seconds,  $\eta$  the overall efficiency of the system and  $NEP$  [ $\text{W}/\text{Hz}^{1/2}$ ] the Noise Equivalent Power of the detector defined as:  $\sqrt{\langle S_{\text{electric}}^2 \rangle} \simeq$



$\sqrt{\langle N_{\text{detector}}^2 \rangle}$ . The last two are determined by the spectrometer characteristics and are constants. The sample size determines the throughput and should always be maximised.

$$\theta = A_D \Omega \quad \Omega = \frac{A_C \cos \phi}{d^2} \quad (3.56)$$

with  $A_D$  the detector area,  $A_C$  the crystal area,  $d$  the effective focal length of the off-axes paraboloidal mirror,  $\phi$  the incident angle and  $\Omega$  the solid angle viewed by the detector. The number of photons. $\text{cm}^{-2}.\text{s}^{-1}$  can be obtained by:

$$\Upsilon = \int_{v_1}^{v_2} \frac{U_v(T)}{hcv} dv \quad (3.57)$$

Two groups of detectors exist: thermal detectors and quantum detectors. Golay cell, pyroelectric- or semiconductor bolometers are examples of the first group, while cooled (liquid Nitrogen) HgCdTe, InSb and PbSe photoconductors belong to the other class. It is this group that is widely used in RAIRS ( $700\text{--}10000\text{ cm}^{-1}$  for HgCdTe) applications, because the NEP is smaller in relation to thermal detectors. The NEP is  $\approx 10^{-9}\text{W}$  vs.  $\approx 10^{-13}\text{W}$ , while the spectral energy density levels are in the range of  $\approx 10^{-3}\text{W}/\text{cm}^2\text{ sr cm}^{-1}$ .<sup>[165,170]</sup> Semiconductor Bolometers are doped and consist of a small chip cooled with liquid Helium that warms up slightly absorbing the radiation. The consequent change in electrical resistance is recorded as a measure of IR-absorption. These detectors are more common in the far-infrared range.

By varying the composition of HgTe and CdTe mixtures, the band gap (wavelength response) of HgCdTe alloys can be changed. The smaller this gap the worse the detectivity. Previously it was stated that it is best to generate the highest intensity possible, however if the intensity is too high, the detector response becomes nonlinear.

Another possible solution to improve S/N levels is by use of an alternative double-beam method: polarisation modulation. The s-polarized spectrum is used as the reference for the polarised one using a photoelastic modulator, that rapidly switches back and forth between the two polarisations.<sup>[167]</sup> This is specially of concern under reactive conditions or high-pressure ambiances. However there have been reports that enhancements of S/N under these conditions were achieved by filtering the s-polarisation out of the beam.<sup>[171]</sup>

Another modulation method to improve S/N that has been developed in the past<sup>[169]</sup> and that is very effective is wavelength modulation. In this case the derivative of the



intensity ( $I$ ) with respect to  $dI/d\lambda$  is obtained. Experimentally this is performed by an oscillating mirror.

### 3.6. Experimental Setup

This section gives a detailed overview of the experimental setups that were used to acquire the STM and RAIRS data. The basics of the UHV (Ultra High Vacuum) systems will be explained by discussing the least complex UHV apparatus first. However to achieve an ultra high vacuum various components will be found on every system used. Therefore after mentioning these aspects only the differences, that are mainly surface science techniques will be explained for the other systems.

In 1650 Otto von Guericke invented the first air pump to create his famous vacuum system by pumping air from hollow copper hemispheres that were joint together. These are nowadays known as the Magdeburg hemispheres.<sup>[175]</sup> The creation and maintaining of an unnatural environment to mimic the gas-density that only exists in interstellar space requires many additional techniques. First of all a turbo-molecular pump which is usually supported by a rotary pump that creates a rough vacuum, while simultaneously limiting the starting load of the turbo pump, that will decrease the pressure from a low vacuum ( $10^{-3}$  mbar) to high vacuum ( $10^{-7}$  mbar). Then a bake-out ( $120\text{ }^{\circ}\text{C}$ ) and component degassing sequence is necessary to achieve ultra high vacuum ( $10^{-9}$  mbar) in order to remove residual gas traces from the filaments and surroundings. This pressure can be further decreased by the use of titanium sublimation pumps (usually operated at set time intervals as function of the pressure) and ion-getter pumps, which are able to remove light, fast molecules that cannot be pumped by the rotor of the turbo pump.<sup>[176]</sup> Once a leak tight UHV is created the base pressure usually approaches  $10^{-10}$  to  $10^{-11}$  mbar. This makes it possible to switch off the turbo and rotary pump and have the system pumped by the noiseless ion-pump only, for STM experiments demand minimal vibration. On the other hand saturation of the ion-pump should be avoided by switching it off during sample dosing or cleaning via Argon sputtering and annealing or other techniques that can generate strong disturbances of the UHV.

The STM results and accompanying conclusions that are presented in this thesis are based on experiments with two different commercial UHV setups: the Specs Aarhus 150 STM (Figure 3.8) and the more complex Omicron VT STM (Figure 3.10). The Specs UHV system consist of one main chamber for both sample dosing, preparation

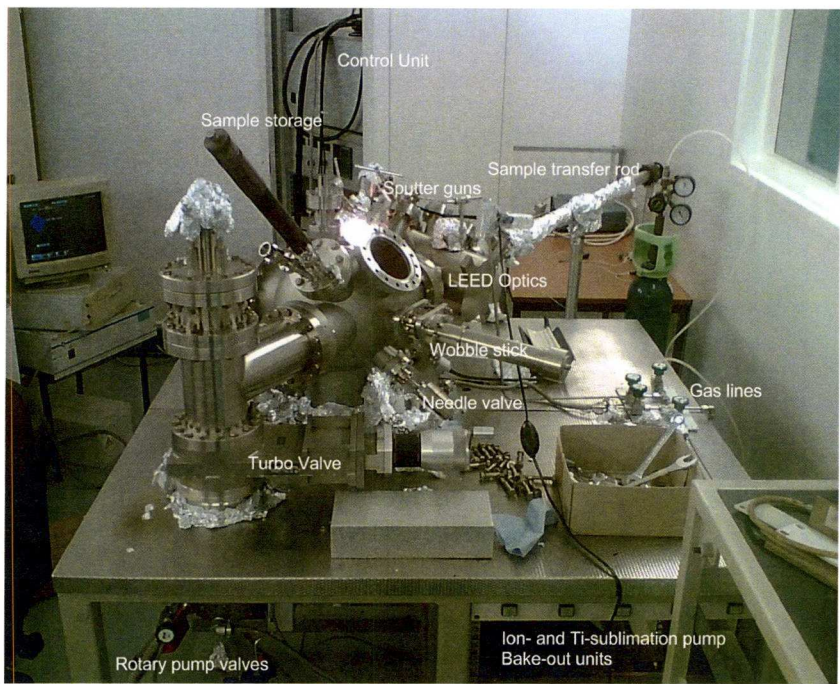


Figure 3.8. – *SPECS Aarhus STM 150*

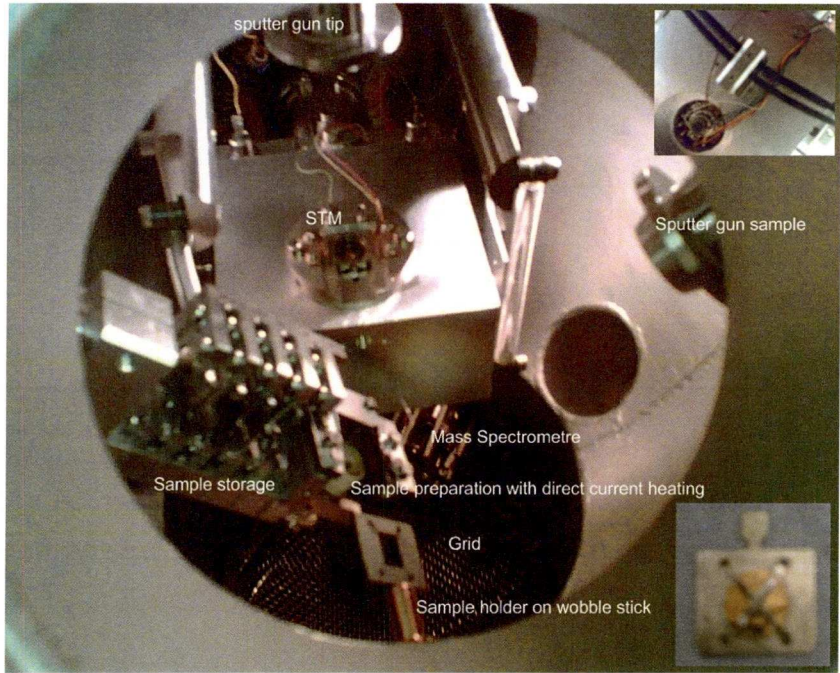
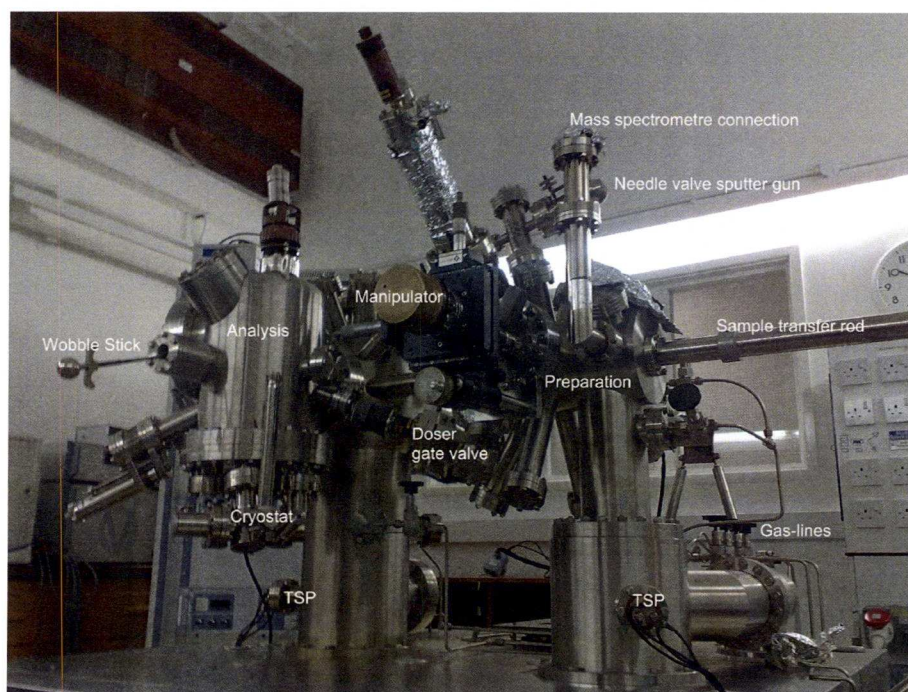


Figure 3.9. – *Interior of the SPECS system, Top inset: damping system under the aluminum block to which the STM is attached. Bottom inset: up side down sample plate with a sample fixed by spot welded tantalum wires.*

and analysing. Furthermore it has all the components described above attached. Apart from the main STM functionality low energy electron diffraction optics (LEED) and



a mass spectrometer are mounted to serve as additional surface characterisation and analysing techniques. Sample transfer from the storage rod to the LEED and dosing position is carried out via a transfer rod, whereas a wobble stick is used to move the sample from the storage rod towards the STM. Stability is not only achieved thanks to an inventive damping system, which can be tuned via de- or attachment of rubber bands, but also via a very small mechanical loop between tip and surface. The temperature range in which the STM operates varies from liquid Nitrogen cooling to 90 K and heating of both tip and sample to 400 K via an aluminum block. A detailed description of the scanner unit can be found in Section 3.2.1. Apart from the excellent stability another main advantage is the possibility of in-situ tip treatment techniques e.g. sputtering or field-emission. This results in a relatively long tip life-cycle compared to other systems. Moreover it limits the need to expose the system to air and disassemble the STM-unit from the UHV system to change tips.



**Figure 3.10.** – *Omicron Variable Temperature STM*

The Omicron Variable Temperature STM (25K-1500K, Figure 3.10) consists of two chambers. A preparation unit that is connected to an analysing unit (STM) and which can be separated by closing a gate valve and hence operate independently of each other once UHV is achieved in both parts. Again all the components earlier described are used to reduce the pressure a factor billion with respect to atmospheric pressures. Typical for this system is that the UHV in the analysing chamber (AC) is kept by a TSP and



an ion-getter pump only i.e. no other pumping devices are attached unless the gate valve to the preparation chamber is open. The AC is extended with LEED/Auger optics and a sample carousel to store unused tips and samples. A wobble stick is used to take samples from the storage place to the STM or manipulator ( $x,y,z,\phi$ ) on which the sample can be resistively heated. A magnetic transfer rod makes it possible to exchange samples between both chambers. The main advantage of two independent chambers is the possibility to leave the UHV in the analysing chamber undisturbed, while carrying out sample preparations that usually cause pressure bursts and the need for UHV recovering.

The PC also contains a manipulator ( $x,y,z,\phi$ ) on which  $e^-$ -beam heating can be applied to the sample. A sputter gun is attached for sample cleaning. Furthermore a mass spectrometer is mounted to perform residual gas analysis. It is possible to insert new samples or freshly prepared tips via a load-lock that can be separated from the PC via a valve and hence ventilated individually. A small transfer rod is used to make the transfer between load-lock and the PC manipulator possible. Usually a doser setup (Section 3.6.1) is attached to this chamber separated by a gate valve. To minimize vibrations both turbo- and rotary pump are shut down, which means that both the PC and AC are kept in UHV by the ion-pumps and TSPs

Figure 3.11a presents a schematic of the main STM components. By releasing the spring suspension (fixed when carrying out non-STM operations) a ring of copper plates is moved in between magnets by the push-pull motion drive, which initiates an eddy current damping system for further minimisation of vibrations while performing STM. Liquid nitrogen or liquid helium can be used to cool the sample via the cryostat but also direct and resistive heating can be applied to the sample. The magnetic tip-holder is placed on the single piezo scanner tube as is visualised in Figure 3.11b via transfer in a tip-holder cage, which makes it possible to exchange tips during an STM experiment.

Also the RAIRS UHV chamber is equipped with LEED optics and a mass spectrometer facility, which is used for the TPD measurements. The auxiliary optics are purged with dry air to prevent  $H_2O$  and  $CO_2$  absorption bands due to the pathway of the IR-beam outside the chamber. The spectrometer used in the experiments is a Mattson instruments 6020 FTIR, with an external Mercury-Cadmium-Telluride detector, which works between 700 and  $4000\text{ cm}^{-1}$ . The IR source is a thermal source, that generally operates at  $4\text{ cm}^{-1}$  resolution and uses on average typically 256 or 400 scans for background and sample, to improve the S/N levels. A detailed explanation of the setup is given on page 50

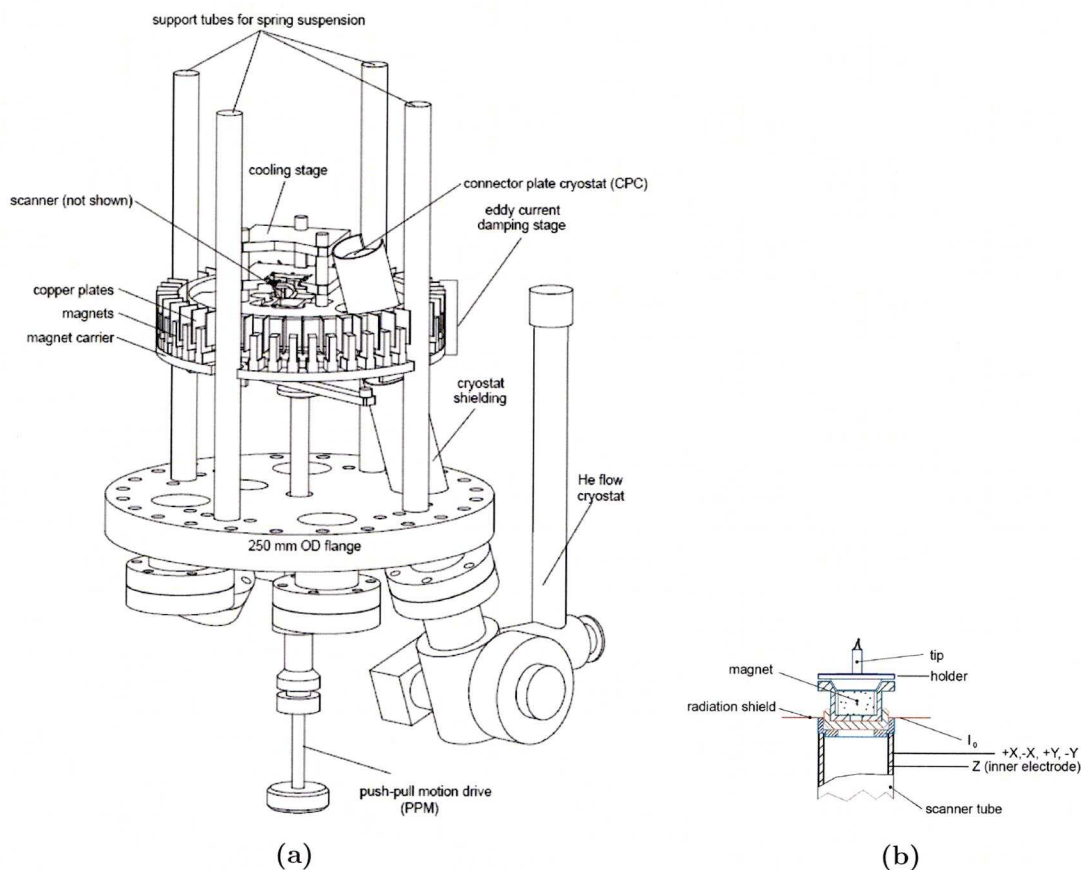


**Figure 3.11.** – a) Schematic drawing of the omicron VT STM unit b) A detailed representation of the scanner unit with tip.<sup>[177]</sup>

### 3.6.1. Doser Setup, Sample, Crystal and Crystal Preparation

Figure 3.12a shows the feedthrough-flange to which the sublimation doser is attached. Furthermore a glass-tube with a tantalum filament helixed around it to resistively heat the sample. A thermocouple (TC) is mounted at the top of the tube by means of a tantalum strip. It is however more accurate to monitor the sublimation via current and pressure control as the TC is not in direct contact with the sample, whereas a sudden increase in pressure usually indicates evaporation. However this is doser dependent e.g. the diameter and size (windings) of the Ta filament and glass-tube diameter and length may differ. TM-TPP was purchased from Frontier Scientific and sublimed from 1.3 to 1.4 A,  $P \approx 5.0 \times 10^{-8}$  in the dosing line. TM-TPP Metallation with Cobalt was carried out by Patrizia Iavicoli from ICMAB, Barcelona.<sup>[178]</sup>

As mentioned before the doser-setup operates as a separate system connected to the PC of a UHV chamber and is pumped by a turbo and rotary pump. Therefore ventilating

the doser line with air does not alter the main chamber UHV properties. Pressures of  $10^{-9}$  mbar in the dosing line are common after a bake out and sample degassing. The distance between crystal and doser may vary per system and hence dosing times (from a few seconds up to a couple of minutes) vary too. Therefore recalibration is necessary after every change of the doser settings.

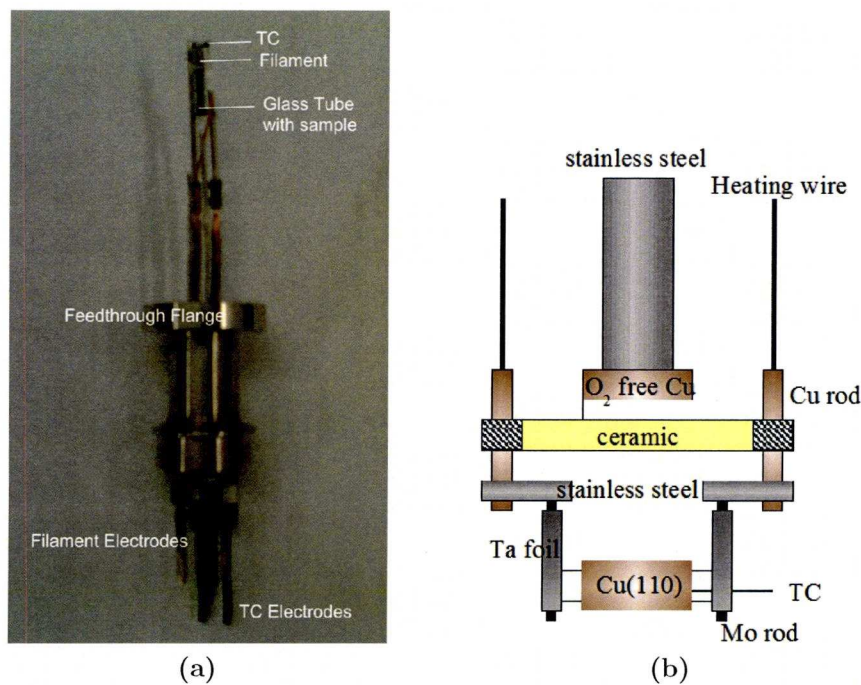


**Figure 3.12.** – a) Sublimation Doser b) RAIRS crystal holder schematic<sup>[179]</sup>

For the SPECS STM measurements a Cu(110) crystal, polished and aligned to  $0.1^\circ$  was purchased from the Surface Preparation Laboratory. The Cu(110) crystal used in the VT-STM and RAIRS are polished and aligned to  $0.5^\circ$ . Repetitive  $\text{Ar}^+$  sputtering and an anneal to  $\approx 823$  K were used to obtain a clean sample with large terraces. LEED was used to check the substrate condition. Crystals used for STM were mounted on a sample plate by spot-welded Ta-wires (Figure 3.9). To prevent contaminating the crystal by sputtering the sample plate simultaneously, the crystal experimental side was chosen not to be below the sample plate but a few mm above. The crystal used for RAIRS measurements was mounted on a manipulator  $(x,y,z,\phi)$  with Ta-wires spark-eroded via two grooves into the two longest edges (Figure 3.12b).



## Chapter 4.

# Adsorption of TM-TPP on Cu(110) at 298K

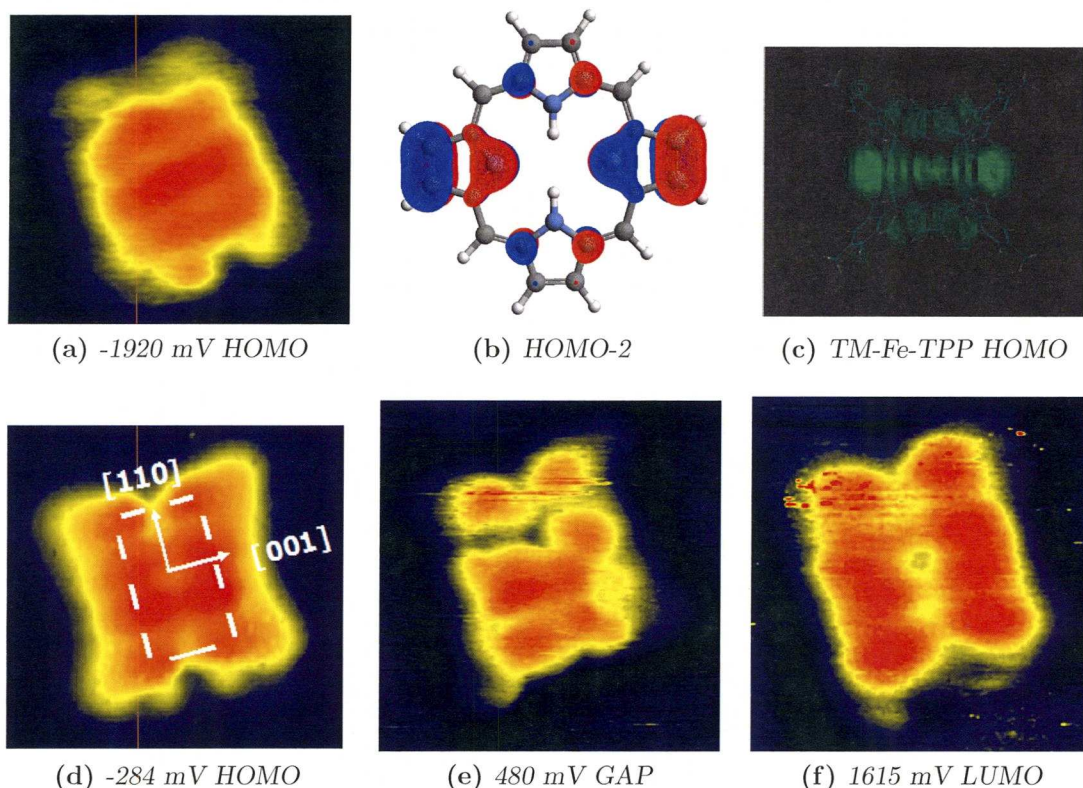
The deposition of TM-TPP on Cu(110) is a complex system.<sup>1</sup> This chapter begins by creating an understanding of the adsorption process at 298 K, which consists of multiple stages. The heating range that spans until  $\approx 450$  K shows various phases that ultimately end in the substrate catalysed covalent attachment of multiple molecules resulting in small networks and branched molecular chains (Chapter 5).

Figure 4.1 shows submolecular resolution images of planar TM-TPP on Cu(110) at different biases. Scanning in the HOMO-LUMO gap makes the original molecule relatively featureless.<sup>[182]</sup> Tunneling into the HOMO or LUMO show a depression in the [110] direction and eight protrusions, four on either side, which sections the molecule in two symmetric parts. The explanation for this effect is saddling (Section 1.2).<sup>[28,33]</sup> The diagonal molecular distance is  $\approx 18$  Å. Moreover opposite pyrrole groups are aligned to both main copper axis.

The area between the outermost protrusions, that originated from the rotated mesityl-groups, is bordered by a rectangle of  $11 \times 6$  Å<sup>2</sup>. This indicates  $D_{2h}$  symmetry and means that interaction with the surface induce conformational change to the low energy  $D_{4h}$  gas phase planar conformation. The mesityl rotation angle ( $\theta$ ) is estimated at  $60^\circ$  degrees based on aspect ratios derived from the STM images. The degree of saddling is assumed to be approximately  $10^\circ$ <sup>[89]</sup>, for this is the lowest energy core conformation

---

<sup>1</sup> Unless otherwise stated all STM images and RAIRS Spectra presented are acquired at constant current (STM),  $T = 298$  K and a base pressure of  $\approx 5.0 \times 10^{-10}$  mbar and  $\approx 2.0 \times 10^{-9}$  mbar while dosing the molecules. Doser settings can be found in Section 3.6.1. Colourcodes on page 1.



**Figure 4.1.** – STM topographical images ( $\approx 26 \times 25 \text{ \AA}^2$ ) of TM-TPP on Cu(110), occupied and unoccupied states,  $I \pm 0.200 \text{ nA}$ . **b)** HOMO-2 orbital configuration of porphine based on Arguslab AM1 calculations<sup>[180]</sup> **c)** Charge density contours at a height of  $2 \text{ \AA}$  above the mean porphyrin plane,  $\theta = 61^\circ$ .<sup>[181]</sup>

accompanying the previous mentioned phenyl angle. This is confirmed by an estimation based on STM images that resulted an angle of approximately  $11.8^\circ$ .

Images obtained over a wide range of negative biases are very similar. In contrast images of the HOMO at relatively lower orbital energies are very different. At higher negative voltages the four central protrusions disappear. Now the brightest protrusion is found at the centre of the molecule, this originates from densities located at two opposite pyrrole rings (Figure 4.1b and c). Both hydrogens are bonded to the remaining opposite pyrrole groups, and therefore parallel to  $[110]$ , pointing upwards. When the porphyrin is adsorbed in the saddled phase hydrogen tautomerism is impossible, due to molecule-substrate interaction or electronic coupling, which could be the reason for the continuum in the central protrusion similar to the LDOS profile of TM-Fe-TPP. Planar phthalocyanines deposited on a NaCl bilayer on Cu(111) do possess tautomerism and hence degeneracy, which can be tuned by tunneling electrons. Decoupling by the



isolated film is essential. When these molecules are deposited on Cu(100) no tautomerism is observed.<sup>[183]</sup> This also suggests copper-molecule interactions.

For both HOMO and LUMO the origin of the four outermost protrusions are the upper *ortho* methyl groups. The other four that are concentrated on the porphyrin core are attributed to LDOS on the methine-bridges for the HOMO. This in contrast to the LUMO for which the electron density is associated with the pyrrole rings. This is in agreement with calculations (Appendix A,  $\theta=51^\circ$ ) performed by Mendoza *et al.*<sup>[181]</sup> It has to be noted that if the protons are aligned with  $\langle 110 \rangle$  rotation of the mesitylene groups is exactly in the opposite direction in comparison to the calculation. It might explain the presence of electron density on the pyrrole groups in the calculations for the HOMO. This is confirmed by the calculated HOMO-1 saddled orbital distribution and the planar orbital configuration (page 11), that have increased symmetry. Therefore it is expected that electron densities that are shown dim on the lower pyrrole rings to which no hydrogens are attached will brighten up when mesityl groups are rotated in the other direction. Calculations for the LUMO, degenerate in the gas-phase, are mesityl rotation independent.

## 4.1. RAIRS

Porphyrin infrared spectra band assignment are readily available in literature.<sup>[46,184–186]</sup> The existence of many different symmetry dependent vibrational modes that are further complicated by substitutional overlap make IR-analysis complex. The most comprehensive approach has been performed by Spiro *et al.*, who developed a DFT-SQM force field for Nickel Porphine.<sup>[187]</sup> A year later, in 2000, they improved this method and applied it to Ni-TPP.<sup>[184]</sup> This is a metal-porphine, which may shift skeletal modes. However, most of the assignments in this chapter are based on their theoretical calculations. The RAIRS data is presented in Figure 4.2, Figure 4.3 and the accompanying Table 4.1.

At initial deposition different spectra are obtained compared to the high coverage phase. This was also observed for FB-TPP on Cu(110).<sup>[47]</sup> After three minutes, dependent on the experimental conditions, the spectrum changes significantly and the number of absorption bands increase. Upon increased deposition times and hence higher coverage the spectrum only increases in strength, the absorption bands remain at their position. This indicates a stable conformation.



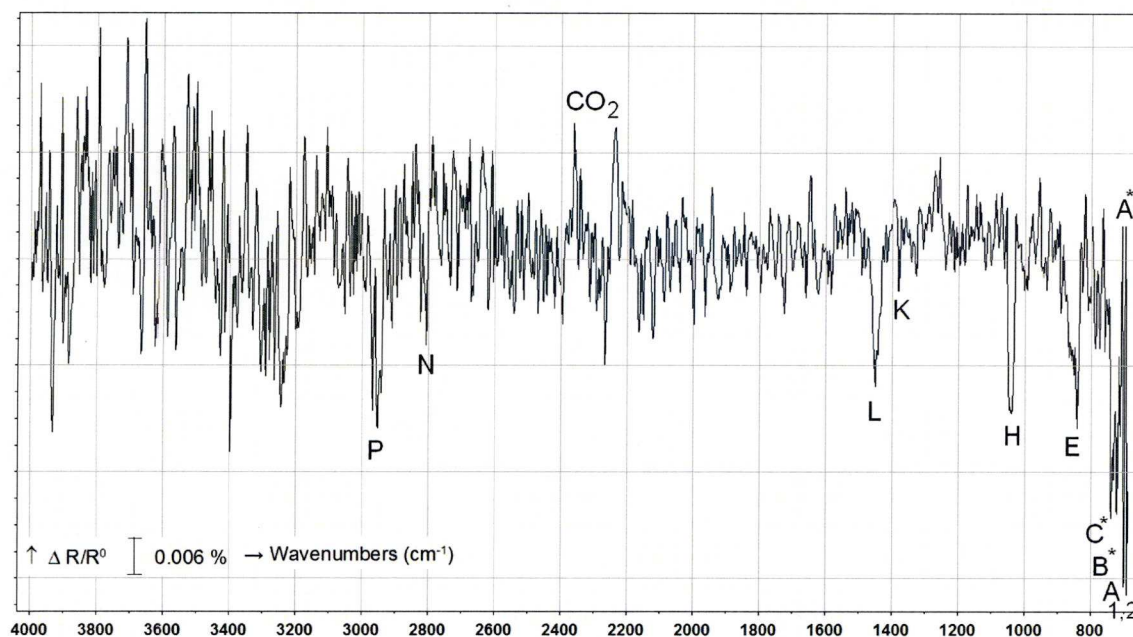


Figure 4.2. – TM-TPP RAIRS spectrum low coverage phase (metastable precursor)

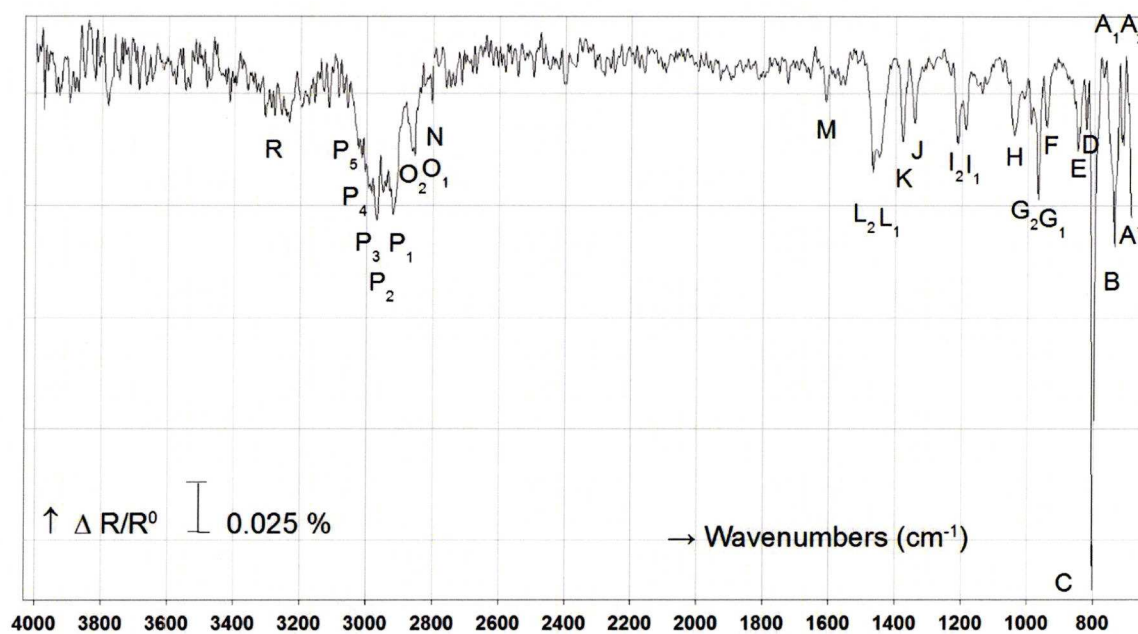


Figure 4.3. – TM-TPP RAIRS spectrum high coverage phase, thermodynamically stable

The differences in conformation could be explained by considering the differences in porphyrin conformation in the gas phase and the conformation at the surface. It is known that TM-TPP molecules in crystals possess non perpendicularity of the mesityl groups and saddling of the core.<sup>[88]</sup> Theoretical calculations for TPP have shown that the lowest energy conformation in the absence of a surface is expected to be planar, with the

four phenyl groups perpendicular to the core (see page 17). However, other gas-phase calculations for TM-TPP<sup>[181]</sup> resulted in a minimum energy saddled conformation, with rotated mesityl groups at an angle of  $\approx 61^\circ$ .

By considering the expected steric hindrance between the  $C_\beta$ -H and the methyl groups it is possible that, similar to TPP, the mesityl groups prefer to be perpendicular in the gas phase. This results in a maximized distance between both i.e. lowest potential energy. Moreover it is assumed that deprotonation of the core has neither occurred during sublimation nor during adsorption on the surface. It has been shown<sup>[89,188,189]</sup> that (de)protonation induces changes in the potential energy curve as a result of conformational changes.

One can propose the following hypothesis: evaporated saddled crystalline molecules change to a more planar orientation, and initially land on the four lowest *ortho* methyl groups. After a certain time spent on the surface the molecules self conform into a low energy saddled phase and rest on the four *para* and the four lowest *ortho* methyl groups due to substrate-molecule interactions.

Another important aspect of planarity and saddling is the difference in symmetry. Whereas saddled porphyrins are known to be  $D_{2d}$ , planar porphyrins are  $D_{4h}$ , which is an increase in symmetry. This is visible in RAIRS spectra via, respectively, degenerate and non-degenerate absorption bands that also decrease in number with increased symmetry.

**Table 4.1a.** – RAIRS TM-TPP low wave-number absorption bands. Normal: Low coverage ( $D_{4h}$ ) **Bold: High coverage** ( $D_{2d}$ )

Peak	$A^*$	$A_1/A_2$	$B^*$	$B$	$C^*$	$C$	$D$
$\bar{\nu}(cm^{-1})$	688	707 / 715	726	739	756	802	
	688	<b>712 / 718</b>		<b>740</b>		<b>803</b>	<b>824</b>
$\frac{\Delta R}{R^0} \times 10^{-2}$	4	4	3		3		
	> 6	<b>4/4</b>		<b>9</b>		<b>24</b>	<b>4</b>
Assignment	ph	oop py $C_\beta$ H as / as f	ip ph	ip ph	CH <sub>3</sub> oop CH b	oop py+ <b>ph</b> s f / <b>CH b</b>	oop ph CH

To maintain clarity the absorption bands will be explained per group. Furthermore analysis is split in two regions: the low and mid wave-number region ( $680\text{-}1200\text{ cm}^{-1}$ )

Table 4.1b. – RAIRS TM-TPP low wave-number absorption bands

Peak	<i>E</i>	<i>F</i>	<i>G</i> <sub>1</sub>	<i>G</i> <sub>2</sub>	<i>H</i>	<i>I</i> <sub>1</sub> / <i>I</i> <sub>2</sub>
$\bar{\nu}(cm^{-1})$	846	943			1039	1196
	<b>850</b>	<b>943</b>	<b>968</b>	<b>990</b>	<b>1040</b>	<b>1188/1213</b>
$\frac{\Delta R}{R^0} \times 10^{-2}$	2				2	
	<b>5</b>	<b>4</b>	<b>4</b>	<b>7</b>	<b>4</b>	<b>4/4</b>
Assignment	oop py/ip ph C <sub>β</sub> H	oop ph	ip ph	ip py hr as	ip ph CH <sub>3</sub> br rock	ip ph+py δ C <sub>β</sub> H as

and the mid and high wave-number (1300-3500 cm<sup>-1</sup>) region. The vibrational modes are shown in Appendix B and explanation of the abbreviations located on (page ix).

The main conclusion obtained from Figure 4.1 is the non-perpendicularity and a-parallelism of the mesityl-groups with respect to the surface. This means that both in-plane (ip) and out-of-plane (oop) modes are infra-red active and hence visible in the spectrum (e.g. *D*). The downshift of the *G*<sub>1</sub> and *G*<sub>2</sub> modes in comparison with the literature is due to the lack of metallation.<sup>[185]</sup> The last vibrational mode in this wave-number region gives a very strong support for the difference in conformation. The peaks *I*<sub>1,2</sub> are attributed to a degenerate band in the high coverage phase, whereas it does not exist in the meta-stable phase, and can be attributed to a change in symmetry (*D*<sub>4h</sub> → *D*<sub>2d</sub>). The *D*<sub>4h</sub> conformation is planar, therefore no intensity is expected in the metastable phase if the vibrational mode is an C<sub>β</sub>H ip py mode. On the other hand theoretical calculations show that in the same region an ip ph mode is situated, which is a more plausible explanation for the presence of a band in this low coverage regime.

The next group are C and F. The in-phase, out-of-plane bending of a ring hydrogen atom is strongly coupled to adjacent hydrogen atoms.<sup>[174]</sup> The position of out-of-plane bending bands is therefore characteristic of the number of adjacent hydrogen atoms on the ring, hence one would expect the 803 cm<sup>-1</sup> mode at a higher wave-number if it originated from a mesityl mode (Appendix C, Table C.2). However Caughey *et al.* found the prominent band around 800 in spectra of a series of porphyrins except etioporphyrin.<sup>[185]</sup> The latter only contains groups at the C<sub>β</sub> of the pyrrole rings, which induce changes to the vibrational properties. They assigned the C<sub>β</sub>-H out-of-plane bending to this band. Following this conclusion it is straightforward to assign band C to an out-of-plane pyrrole mode. However the relatively massive intensity increase with respect to the other absorption bands requires a different approach. This cannot only be attributed to a oop



pyrrole mode. Moreover all the other low region oop py bands  $A_1/A_2$ ,  $B$ ,  $E$  do not show an eightfold increase upon saddling. In addition to this; by analysing the spectra of pOH-TPP<sup>[190]</sup>, it becomes clear that in the saddled phase the majority of the intensity is due to the oop ph CH bending mode. This is also in agreement with the assumption that the mesityl-groups are perpendicular to the core initially, only a tilted and rotated group will induce the C-H bending mode to be infra-red active. The downshift of the absorption band with respect to the same band in mesitylene and tetramethylbenzene (837, 859  $\text{cm}^{-1}$ ) can be attributed to porphine connection, which counterbalances the upshift of this mode by the lack of neighbouring hydrogen atoms (an electron withdrawing or donating effect).<sup>[191]</sup> This increase in wave-number explains the difference in assignment by Spiro *et al.* They give this mode a wave-number of 620  $\text{cm}^{-1}$  as a result of the lack of methyl groups splitting surrounding hydrogens. Therefore it is expected that in the metastable phase this mode is a oop py symmetric fold mode or a limited number of molecules possess a saddle configuration.

The other oop ph band in this group is F. It is visible in both cases, planar and saddled, showing a moderate intensity. Only if the mesityl groups are parallel to the surface this mode is almost non existent in RAIRS (see RAIRS mesitylene Appendix C). Mesitylene is thought to absorb flat and is known to be planar.<sup>[192]</sup> This is supported by Chang *et al.*<sup>[193]</sup> who investigated xylene on Rh(111) and benzene on Cu(110), which also favour a flat orientation in the first layer.<sup>[194]</sup> Moreover the lack of (asymmetric) highly electronegative groups e.g. nitrogen<sup>[195,196]</sup> or oxygen<sup>[197]</sup> causes the  $\pi$ -system to be parallel to the surface, which decreases the total energy and increases the wave-function overlap with the substrate. However according to theoretical calculations the oop ph mode is only visible in  $D_{2d}$  symmetry, which contradicts its presence in the low coverage phase. Therefore it is attributed to a small number of saddled molecules.

The following bands grouped are  $A^*$ ,  $B$ ,  $B^*$  and H. The first vibrational mode ( $A^*$ ) is at 688  $\text{cm}^{-1}$ . This band is also present in the vibrational spectrum of mesitylene. Therefore this absorption band is assigned an aromatic ring torsion ( $\chi$ )<sup>[198]</sup> mode instead of an oop ph mode. After mesityl rotation this mode drops in intensity. In the spectrum of mesityl this mode is strong and assigned at 684  $\text{cm}^{-1}$ , whereas the mode at 697  $\text{cm}^{-1}$  is unknown, but intensity-wise assumed to be an oop mode (presumably the asymmetric out-of-phase coupled  $\text{CH}_3$  vs. H bend).

Based on other porphyrins (mOHTPP and pOHTPP)<sup>[190]</sup>  $B$  and  $B^*$  are assigned in-plane phenyl mode with the vibration perpendicular to the meso bond after rotation this mode disappears for  $B^*$ . The type of vibration is not exactly known. Since these are

$\pi$  modes and others situated at higher wave-number regions  $\phi$  modes containing both C=C stretch and CH stretch vibrations, the most logical assignment is ip aromatic CH bend.

Band H is also attributed to an ip ph mode. However the assignment of this band is not exactly clear. It could be a phenyl breathing mode as it loses some, but not all, intensity upon rotation. In the high coverage phase this band is possibly augmented by both an oop ph  $\Psi''_8$  mode and an ip py mode. It is, however not exactly known what the influence of the methyl groups is.<sup>[191]</sup> Based on the other assignments and the assumption of the planar to saddling change an ip ph mode seems unavoidable. Flat absorbed mesitylene also shows this mode at low intensity, which due to the surface selection rule cannot be attributed to the same ip ph mode. Therefore a CH<sub>3</sub> rocking mode after Lokshin *et al.* is possibly augmented.<sup>[198]</sup>

The last group are oop py modes A<sub>1</sub>/A<sub>2</sub> and E. According to the calculations by Spiro *et al.* the A<sub>1</sub>/A<sub>2</sub> adsorption band should shift down by symmetry change, however no sign of this is observed. A possible explanation of this is that the calculations are based on a ruffled porphyrin, whereas the porphyrin under discussion is saddled. Hence no direct comparison is possible. This mode is probably overlapped by an ip phenyl contribution. In addition the coverage is greater at higher exposures which may counteract intensity loss due to non-planarity.

The remaining band C\* is neither an ph or py mode, but presumably an oop methyl C-H bending mode as it is not present in OH-TTP and disappears upon saddling.

Modes that have not been mentioned, but which are expected are the C-C(H<sub>3</sub>) stretching and bending modes. The first usually occurs in the 800-1200 cm<sup>-1</sup> region but, if active, it is weak and therefore easily overlapped or lost in the noise. The second occurs at far-ir frequencies and is therefore unobserved.<sup>[174,199]</sup>

The mid and high coverage regime are split in four groups. The first group contains band J and M, which are respectively an ip py and an ip ph mode that are both not present in the low coverage spectrum. Peak J the ip py half ring symmetric appears upon saddling. Mode M is an ip ph mode that appears as a weak band in the high coverage spectrum. In OH-TTP this mode is significantly more pronounced similar to the IR spectrum of mesitylene. This implicates that the mesityl group, when compared with the conformation of the phenyl groups in OH-TPP, does not show much resemblance. In TM-TPP one of the *ortho* methyl groups interacts with the surface while in OH-TPP the *para* -O group bind to Cu. Hence this mode is expected an aromatic C=C

stretch influenced by the OH and methyl-groups as well. But to a different extent when compared to the oop C-H bend (Appendix C).

Table 4.1c. – RAIRS TM-TPP mid and high wave-number absorption bands

Peak	<i>J</i>	<i>K</i>	<i>L</i> <sub>1</sub> <i>L</i> <sub>2</sub>	<i>M</i>	<i>N</i>	<i>O</i> <sub>1</sub> / <i>O</i> <sub>2</sub>
$\bar{\nu}(cm^{-1})$		1382	1449 / 1469		2795/2813	2862
	<b>1343</b>	<b>1378</b>	<b>1450/1468</b>	<b>1610</b>	<b>2804</b>	<b>2855/2863</b>
$\frac{\Delta R}{R^0}$		1	2		1	
$\times 10^{-2}$	<b>4</b>	<b>5</b>	<b>6/7</b>	<b>2</b>	<b>3</b>	<b>5/5</b>
Assign- ment	ip py /oop ph hr s	ip CH <sub>3</sub> s b	ip CH3 ph as b	ip ph C=C str	overtone	CH <sub>2</sub> s CH str

Table 4.1d. – RAIRS TM-TPP high wave-number absorption bands

Peak	<i>P</i> <sub>1</sub> - <i>P</i> <sub>2</sub>	<i>P</i> <sub>3</sub>	<i>P</i> <sub>4</sub>   <i>P</i> <sub>5</sub>	<i>Q</i>	<i>R</i>
$\bar{\nu}(cm^{-1})$	2905-2938	2967		3076/3086/3096	
	<b>2921-2950</b>	<b>2969-2995</b>	<b>3005/3016/3025</b>		<b>3300</b>
$\frac{\Delta R}{R^0}$	2				
$\times 10^{-2}$	<b>7</b>	<b>7</b>	<b>6/5/5</b>		<b>3</b>
Assign- ment	CH <sub>2</sub> + CH <sub>3</sub> as str s str	CH <sub>3</sub> C-H as str	oop ar C-H	ip ar CH	N-H s/as str

*L*<sub>1,2</sub>, *K* and *R* are considered next. If the *L* modes would be of ip py nature one would not expect any vibration according to the surface selection rule. Therefore it is justified to assign the two modes present to, respectively, a CH<sub>3</sub> bending an ip ph mode or an *A*<sub>2u</sub> Ψ oop ph mode calculated to exist around 1440 cm<sup>-1</sup>. A weak absorption band is visible for mesitylene that absorbs flat. The computational value of the ip ph mode is ≈1490 cm<sup>-1</sup>. It is expected that this mode increases in intensity upon saddling (*L*<sub>2</sub>). Mode *K* is the in-phase symmetric bending mode of the CH<sub>3</sub>. *R* is the broad N-H str region. This is a weak band and another clear sign of saddling. A C-N stretching mode is expected too. Unfortunately this is also a weak mode and can be found in the previously discussed region around 1300-1500 cm<sup>-1</sup> so if active it probably will be dominated by the stronger modes present.



Finally N, O<sub>1,2</sub>, P<sub>1,2,3,4,5</sub> and Q are grouped together. Band N is a distinct feature that appears in many (aromatic) ring spectra, especially with alkyl groups. Previously it has been assigned to an overtone/combination band.<sup>[200]</sup> These bands are usually weak and most of the times found in thick samples and are not valuable for any conclusion in the analysis of e.g. the substitution pattern.

In contrast band O would classify as a CH<sub>2</sub> symmetric stretching mode. This is remarkable since the molecule has no methylene groups, the band is too strong in the high coverage phase to be an overtone/combination band and its wave-number too low for a CH<sub>3</sub> stretching mode.<sup>[199,201]</sup> In the low coverage phase this mode is not split, whereas at higher coverage (and in the RAIRS of mesitylene) it is. Added to this the fact that phenyl groups are perpendicular, which means that only one methyl group is able to interact with the surface. One can, therefore, put forward the hypothesis that for a saddled molecule all four methyl ‘feet’ interact with the substrate, and hence CH-Cu interactions occur. CH-metal interactions have been documented in a number of surface science studies.<sup>[202,203]</sup> Softening of the CH mode results in occurrence at lower wave-numbers i.e.  $\approx 2760\text{ cm}^{-1}$ . The spectra of mesitylene, that absorbs flat, and therefore has surface interaction with all three methyl-groups shows this mode at the same wave-number. Since it is expected that the methyl-groups lift the phenyl-ring from the surface, interaction of the ring-hydrogens with the substrate is ruled out. This means that the softened CH stretch and CH<sub>2</sub> stretching modes visible in the spectrum originate from the methyl groups. An interacting CH group could be uncoupled and the remaining CH<sub>2</sub> group shows a methylene mode. Also in the high coverage spectrum of TM-TPP three small peaks around  $2760\text{ cm}^{-1}$  are visible, which could be attributed to CH-metal bonds at different adsorption sites. In the low coverage regime, where the mesityl groups are initially in substrate contact with only one methyl group these modes are less distinct.

Vibrations P<sub>1,2,3</sub> consist of both methylene and methyl modes, respectively an asymmetric stretch and a symmetric stretch. Care has to be taken in assigning these bands, for both modes may show shifts due to ring strain. If this is not present the modes do not vary much from what is known in literature. The higher modes P<sub>4,5</sub> and Q are respectively ip and oop aromatic CH stretching modes and appear almost perfectly at the predicted theoretical values by Spiro *et al.*

## 4.2. STM

The most important conclusion from the former sections is the change of conformation and adaptation of TM-TPP to the corrugated substrate. A molecule can adapt itself to any substrate by changing its internal conformation, but also the atoms in the surface plane may show reconstructions to find the optimal adsorption strength.<sup>[204]</sup> Surface reconstructions by molecules are widely documented.<sup>[205–207]</sup> For Lander molecules, that also possess a relatively large  $\pi$ -system to which four t-butyl groups are attached that create electronic isolation from the surface, no reconstruction of the surface steps is observed for  $T < 150$  K<sup>[208]</sup>. Furthermore the process of step restructuring is thermally activated. Schunack *et al.*<sup>[209]</sup> have studied the anchoring of HtBDC on Cu(110). This molecule creates surface reconstruction upon adsorption by forming a trench-like base. The atoms responsible for the vacancies diffuse to steps at 41 K. No clusters are observed. Moreover the temperature dependent conformational changes of Pt-TBPP on Ag(110) were observed.<sup>[210]</sup> Gross *et al.*<sup>[211]</sup> showed that they were able to trap, collect, move and release a copper cluster of six Cu ad-atoms on Cu(111) simultaneously by using a specially designed organic molecule viz. HB-HPB. Full planarity of this molecule is prohibited by phenylic steric hindrance, which is essential for the mechanism in cooperation with the elevation of the molecule by the t-butyl groups. The binding and diffusion of different copper clusters on Cu(111) was already observed at 4–21 K by Repp *et al.*<sup>[212]</sup>.

A series of images that represent a low coverage of TM-TPP on Cu(110) is shown in Figure 4.4. On the right a step edge is visible. The TM-TPP molecules are distributed randomly at the substrate and do not have a preference for agglomeration at energetically more favourable step-edges. This indicates a strong interaction with the substrate. Multi-dimensional atomic chains are visible in the  $\langle 1\bar{1}0 \rangle$  direction. One of these chains migrates to the step edge (arrow). The Cu clusters form (mono-)atomic chains at RT even after porphyrin deposition. Previously it has been shown that addition of atoms forming a Mn and Au chain respectively show a linear behaviour.<sup>[213,214]</sup> Therefore the distance is a measure of the number of atoms residing in the chain, with the limitation that the apparent distance of a single atom is known. Furthermore TM-TPP molecule size differences can be observed. This is attributed to a substrate induced mechanism and is thought to be due to copper atom rearrangement under the molecules.

The combination of RT experiments and TM-TPP must create a special interaction with the substrate and hence to clustered Cu-chains of different lengths rather than step edge growth. Isolated HtBDC molecules on Cu(110) adsorb planar, however, adjacent



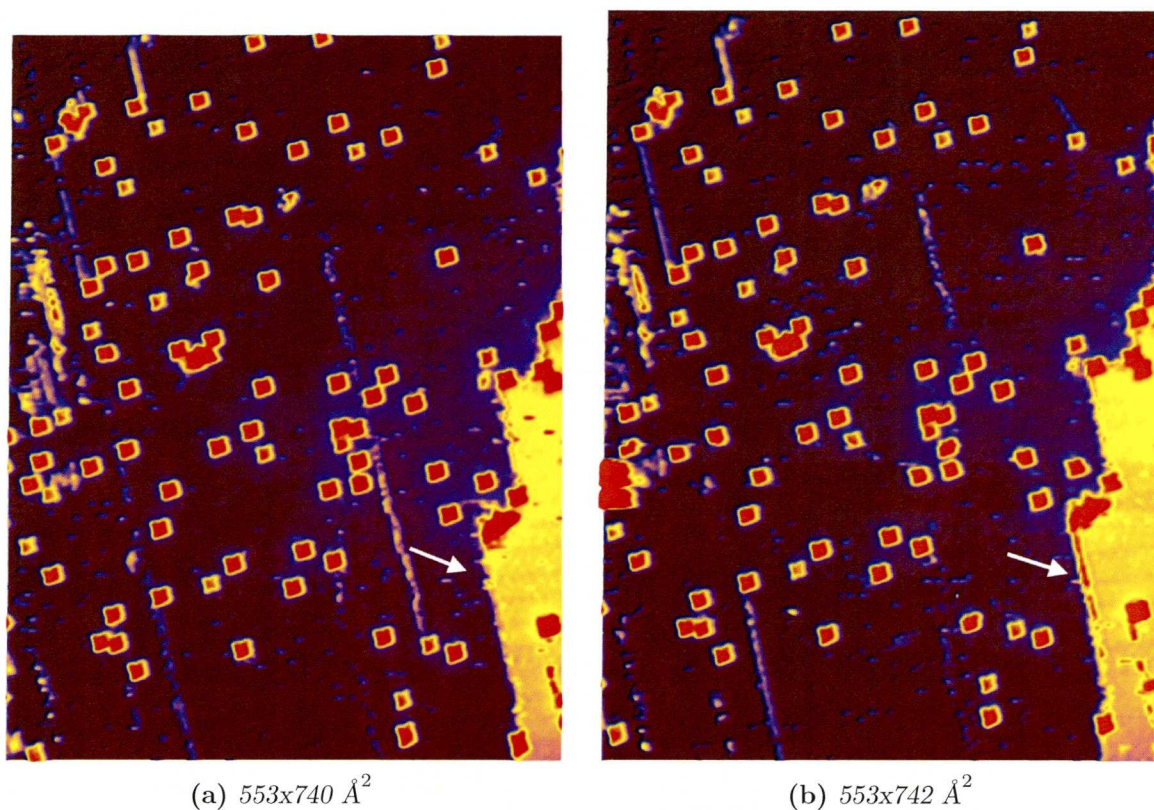


**Figure 4.4.** – Image sequence ( $\delta t=40s$ ) indicating the dynamic substrate behaviour at RT (white arrow),  $V \approx 284$  mV,  $I \approx -0.500$  nA.

molecules that create the trench are tilted. Manual manipulation forming adjacent molecules did not induce conformational changes, which indicate that strong molecule-substrate interactions are required to induce the conformational change. The tilt is only observed when  $T > 250$  K, moreover the creation of the trench is fully attributed to t-butyl groups facing each other. The creation of steps and kink sites underneath the molecules lead to a higher substrate reactivity. Comparison with the results of Schunack *et al.* and Gross *et al.* suggests that the t-butyl- and methyl-groups and the simultaneous separation of the molecular  $\pi$ -system from the substrate are essential for this type of molecule-substrate interactions.

TM-TPP molecules on Cu(110) do not self-assemble at any coverage. A high coverage STM image is shown in Figure 4.5. No short range order is visible. However, molecular alignment to both main copper axis is visible. This implicates that, although no domains of molecules are created, every molecule is fixed. The energy at RT is not sufficient to change rows and hence the lack of self assembly once adsorbed on a copper row in the



[110] direction. This also explains why step-edged agglomeration is limited with respect to terrace adsorption.

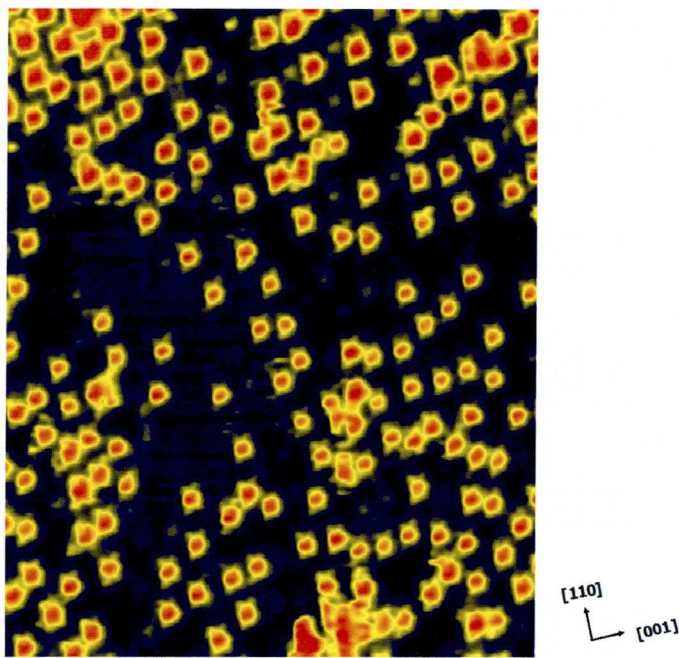


**Figure 4.5.** – High coverage TM-TPP on Cu(110),  $183 \times 222 \text{ \AA}^2$ ,  $V = -311 \text{ mV}$ ,  $I = -0.140 \text{ nA}$ .

Therefore it is proposed that after planar TM-TPP molecules land on the substrate, a conformational change towards a saddled phase may lead to diffusion over the substrate in order to find the minimal adsorption energy. This diffusion is, based on the direction of the copper chains and similar to HtBDC, parallel to the close packed rows. During this process, that requires rotation of the mesityl groups, strong interaction with the surface occurs and copper ad-atom clusters are formed. Once a thermodynamically stable adsorption site is found diffusion stops at these experimental conditions. In the next chapter it will be shown for a special situation that diffusion of saddled TM-TPP molecules can occur at RT and that at elevated temperatures diffusion mainly occurs perpendicular to the [001] directions.

## Chapter 5.

# Thermal activation of TM-TPP on Cu(110)

No self-assembly was observed for the RT phase of TM-TPP on Cu(110).<sup>1</sup> Therefore the thermodynamical equilibrium was changed by the addition of thermal energy, split in an intermediate  $RT < T_s < 450$  K and a highly activated  $450 < T_s < 493$  K (decomposition) region. Low and medium coverages are essential for the resulting molecular properties upon heating. For a better understanding, and in addition to the final remarks of the former chapter, the high coverage intermediate region together with the properties of a medium coverage at elevated temperatures will be discussed first.

A high coverage phase is shown in Figure 5.1a. Small domains of molecules that line up along the main copper axis can be distinguished. However, no self-organisation is observed. The red stripe consists of four molecules adsorbed on top of the first layer.

Figure 5.1b shows HT-STM images created by re-heating a medium covered substrate to 373 K while performing STM. The four molecules indicated in the square tend to self-organise by diffusion along  $\langle 110 \rangle$ . Diffusion in the  $[001]$  direction is less frequently observed. Therefore it appears that, at these temperatures, molecules that are not on the same, but on adjacent copper  $\langle 110 \rangle$  rows, function as ‘stops’ and prevent self-organisation in large domains at elevated temperatures especially at higher coverages when space to diffuse is limited.

---

<sup>1</sup> Unless otherwise stated all STM images and RAIRS Spectra presented are acquired at constant current (STM),  $T = 298$  K and a base pressure of  $\approx 5.0 \times 10^{-10}$  mbar and  $\approx 2.0 \times 10^{-9}$  mbar while dosing the molecules. Doser settings can be found in Section 3.6.1. Colourcodes on page 1.

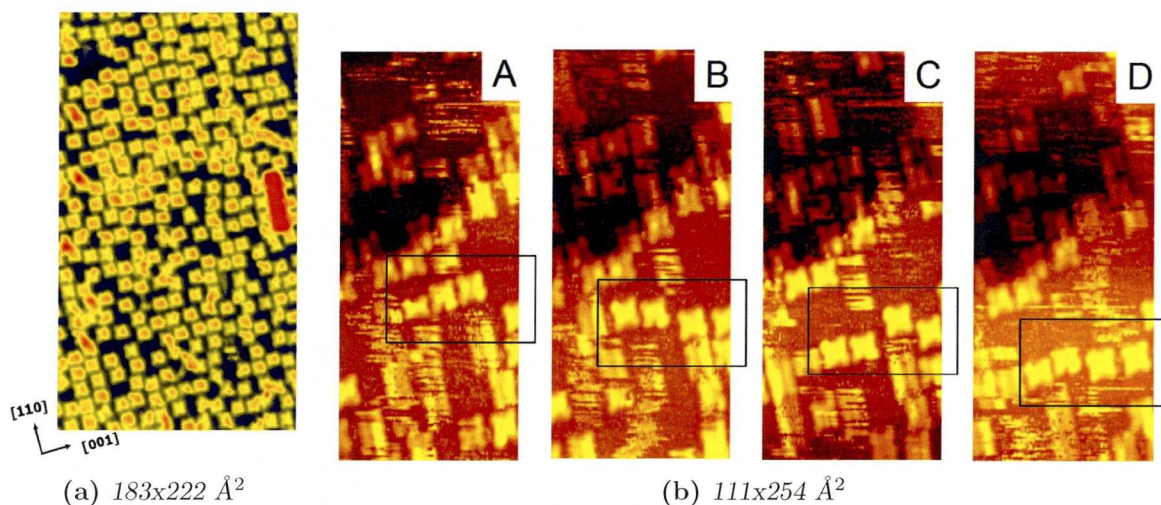


**Figure 5.1.** – a) High coverage intermediate region,  $V_a=222$  mV,  $I=0.200$  nA b) Medium coverage intermediate region. TM-TPP on Cu(110) at 373 K.  $V_b= 883.8$  mV,  $I=0.180$  nA,  $dt=4,2$  and 3 minutes respectively.

## 5.1. Intermediate Activation: STM

The STM images shown in Figure 5.2 are obtained after heating a medium covered substrate ( $\approx 0.28$  ML) and maintaining it at  $\approx 450$  K for thirty minutes. This results in a conformational change. Generally, a molecule without any bright protrusions images with  $D_{4h}$  symmetry, whereas when part of the molecule is distorted it lights up. Molecules can, therefore, be assigned ‘off’ when no bright protrusions are present and ‘on’ when one or more bright spots are seen. In Figure 5.2a the long white arrows indicate both main copper axis and run parallel to the porphyrin located on the left next to the origin. Based on these directions the two green lines that are parallel to the main axis can be drawn, which connect three protrusions located on different molecules. Subsequently the yellow lines that connect two protrusions per line in either direction and that are also parallel to the others can be created. The result is a rectangular grid (short arrow) representing the copper corrugation. The dimensions of each rectangular are  $7.2 \times 5.1 \text{ \AA}^2$ , which is a Cu(2x2) unit cell. A similar situation of lattice adaptation was observed by Suzuki *et al.*, who observed a higher contrast for one of the TB groups in Cu-TBPP. This is attributed to different electronic coupling to the substrate.

Figure 5.2c gives a magnification of the area shown in A (Figure 5.2a). It has to be noted that apart from the single TM-TPP molecules present on the substrate also dimers can be found. This molecular interaction will be discussed in Section 5.3. Furthermore three distortion types can be classified. First a distortion on one of the four quadrants of



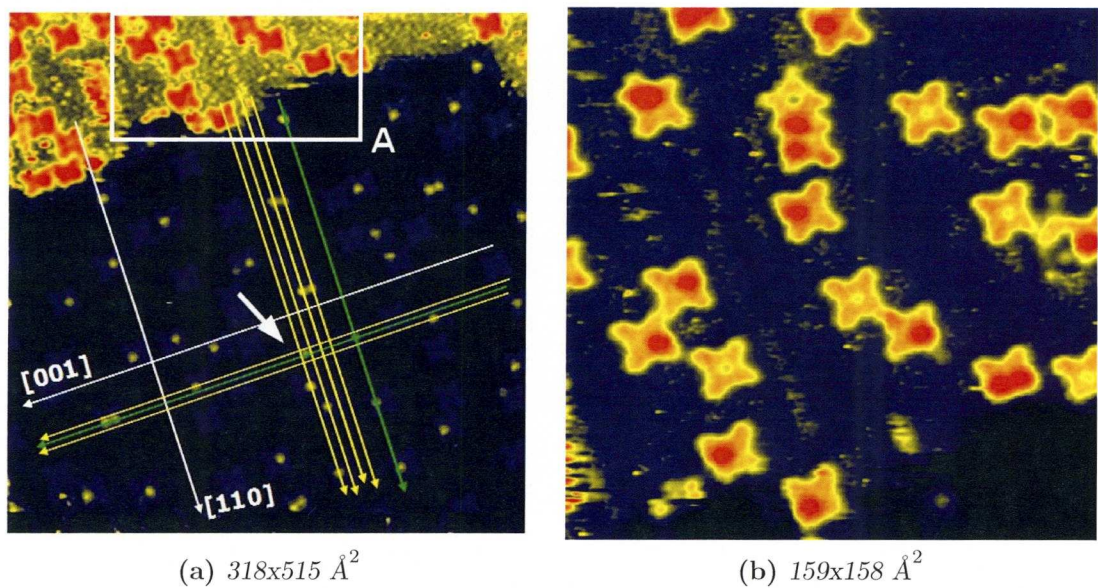


**Figure 5.2.** – a) TM-TPP intermediate on Cu(110),  $V=-551$  mV,  $I=-0.220$  nA. b) Magnification of the terrace (A) shown in image (a).

the porphyrinic core, but also multiple conformational changes that at maximum concern two quadrants. And finally undistorted molecules. Moreover the presence of copper ad-atoms and clusters, identified by the small tracks in the image, show that the substrate has a higher chemical reactivity.<sup>[122]</sup>

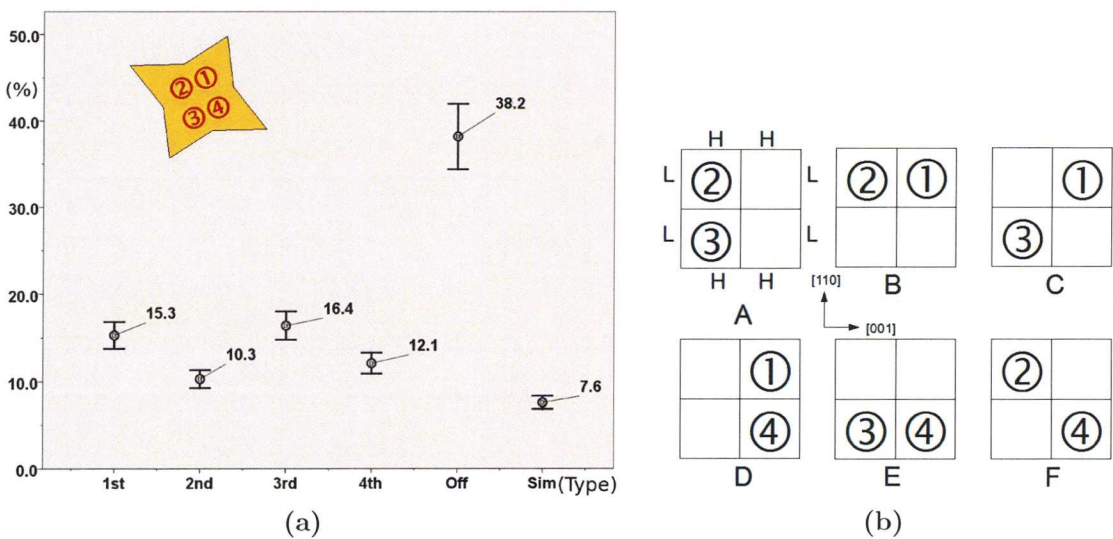


**Figure 5.3.** – a) Statistical analysis presenting the type of lighting up per molecule in percents. The quadrants are indicated in the star-shaped TM-TPP representation. b) Schematic showing the simultaneous lighting up possibilities. The square represents the porphyrinic core, with the up (H) and down (L) ortho methyl group in the saddled conformation.

Analysis of a total number of  $445 \pm 4$  molecules show (Figure 5.3a) that the on/off ratio is approximately 60/40. The number of simultaneous lighting-up events is significantly smaller than the occurrence of a individual protrusion on a single molecule. Six possible combinations can motor a double lighting-up event. All but two combinations (A and D) are observed (Figure 5.3b). These involve both quadrants aligned along  $\langle 110 \rangle$ . Moreover both the first and third porphyrinic quadrants light up significantly more frequent than other regions.

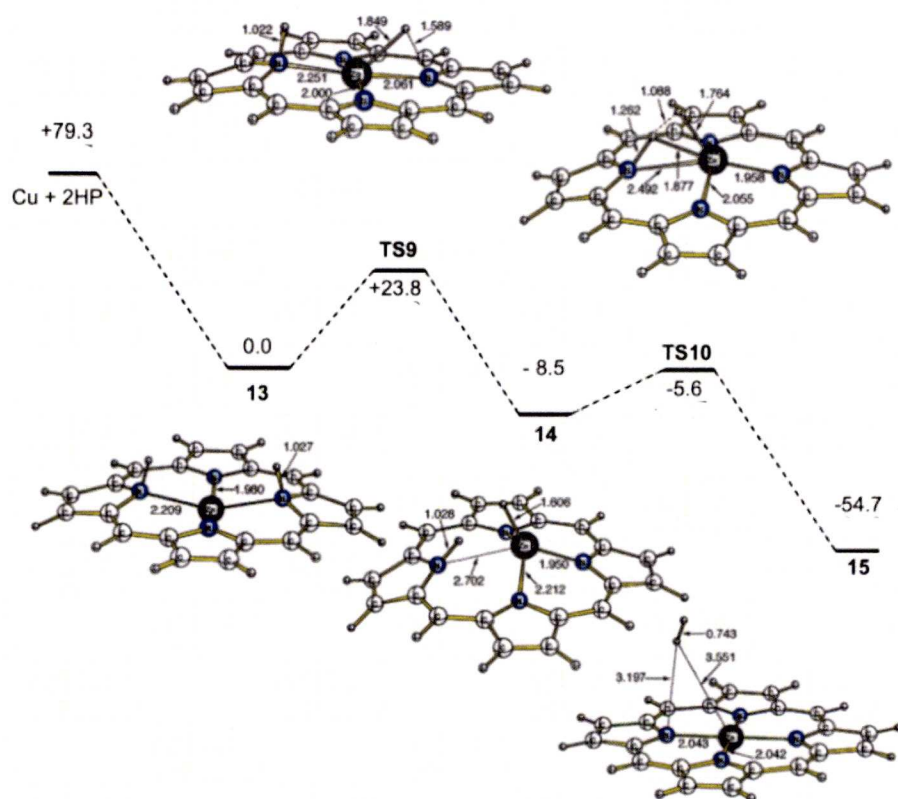


**Figure 5.4.** – Zn (Cu) atom insertion into H<sub>2</sub> Porphyrin and the Cu-energy profile,  $\Delta E + \text{ZPVE}$  in kcal mol<sup>-1</sup>, DFT(B3LYP/6-31G(d)).<sup>[57]</sup>

The saddled TM-TPP molecule at RT serves as a starting point for a better understanding of the distortion and its implications. That conformation suggests that a copper (ad)atom is participating in the electron density contribution of the core. Therefore heating the substrate could deprotonate the core by copper absorption. Figure 5.4 is a reaction scheme for Zn-absorption based on XPS-measurements and DFT calculations.<sup>[57,215]</sup> The mechanism is similar to Cu-absorption for which the energies are indicated instead. Metallation is an activated process i.e. at lower temperatures ( $T < 115$  K) formation of complex 13 is impossible. This complex has a Cu-atom coordinated with the two pyrrolic N-H bonds simultaneously. It is proposed that the rate limiting step of



this reaction is determined by the pyrrolic hydrogen transfer to the metal centre (TS9) and that at 300 K (Zn) formation occurs possibly controlled by the diffusion rate of substrate metal atoms. The reaction completed at 550 K. For Cu an activation energy of  $23.8 \text{ kcal.mol}^{-1}$  was found ( $RT \approx 20 \text{ kcal.mol}^{-1}$ ).

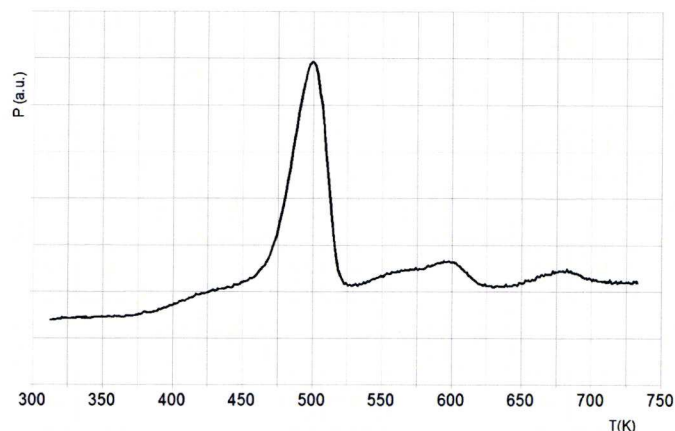


**Figure 5.5.** – TPD profile of TM-TPP on Cu(110) monitoring the evolution of hydrogen into the vacuum,  $dt \approx 400\text{s}$ .

Temperature programmed desorption data (Figure 5.5) is in good agreement with the previously mentioned activation energy. It shows that the total decomposition of the molecule reaches a maximum at 500 K. At  $\approx 375\text{K}$  ( $\approx 23.8 \text{ kcal.mol}^{-1}$ ) to 450 K a relatively small amount of hydrogen desorbs from the surface, which is the result of core-deprotonation and other reactions that will be discussed later and in Section 5.3. The desorption peaks at 600 K and 675 K are attributed to either gas desorption from the sample holder or to more stable decomposition products. It has to be noted that the TPD data describes the properties of individual TM-TPP molecules. This is due to a significantly shorter heating cycle in comparison to the STM and RAIRS data presented, which limits the residence time at elevated temperatures.

Although the optimised Zn-P is planar, absorption of a metal induces conformational changes in the macrocycle. For complex 14 and TS10 a tilt of the pyrrole units is visible, while the deprotonated metallated version (15) is symmetric. It is, therefore, expected that the core of the saddled porphyrin upon Cu absorption converts to planar. Moreover frequently observed planar metallo-porphyrins lack bulky substituents and contain central metals like copper(II) and zinc(II).<sup>[80,84]</sup>

Metallation was also observed for a sample of TM-TPP deposited from chloroform onto a large excess of copper filings in vacuum heated to 353 K, analysed by laser des-



orption-ionisation time-of flight (LDI-TOF, Appendix D). Metal incorporation was increased when stirred in DMF at 373 K with the porphyrin under an inert atmosphere.<sup>[216]</sup>

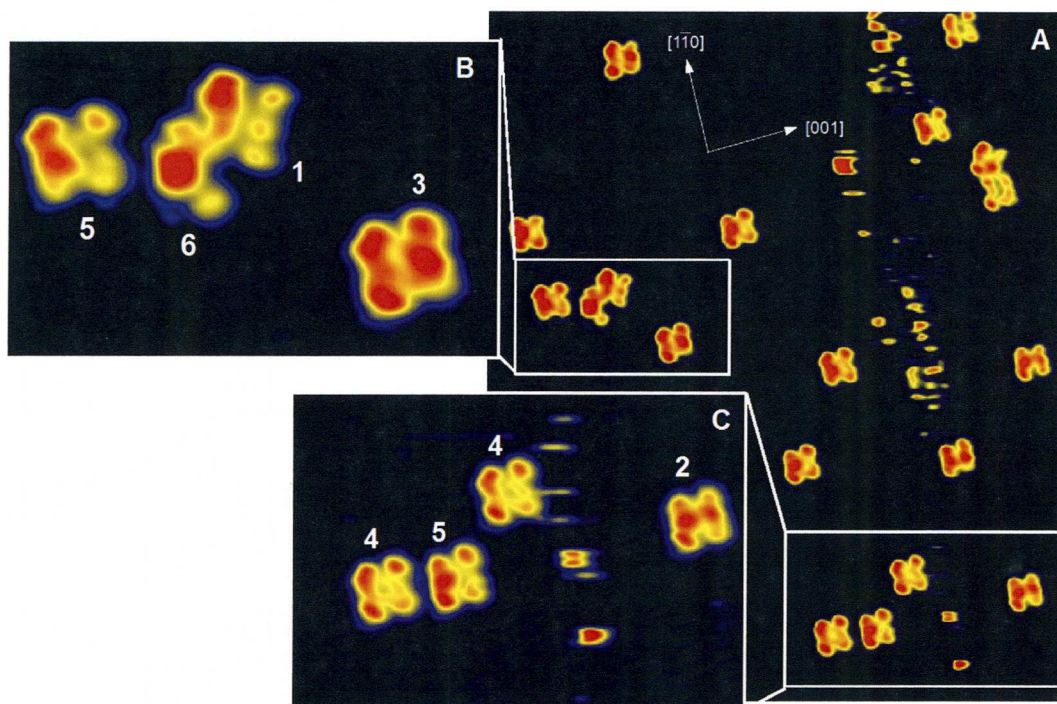


**Figure 5.6.** – A) TM-TPP intermediate at Cu(110),  $281 \times 332 \text{ \AA}^2$ ,  $V = -300 \text{ mV}$ ,  $I = -0.259 \text{ nA}$ . B)  $89 \times 56 \text{ \AA}^2$  C)  $134 \times 93 \text{ \AA}^2$ .

Figure 5.6 shows a submolecular resolution topographical STM image of the intermediate phase. The post-anneal substrate temperature was kept at  $\approx 423 \text{ K}$  for thirty minutes, which is approximately the temperature at the transition state for the conformational change. The majority of the molecules have changed configurations. Some molecules are found in proximity of each other and may show an interaction similar to the dimers in Figure 5.2. Not only the higher resolution but also the limited addition of thermal energy in comparison with that result does invoke the existence of individual molecules at different conformational stages. This confirms that substrate-molecule interactions control the change in conformation otherwise a uniform appearance of every molecule would have been observed. Moreover streaks formed by ad-atoms, and rotation of molecules are observed. The different conformational stages are numbered 1 to 5 in frame B and C, which are magnifications of the regions indicated by a rectangular.

Calculations executed for TM-TPP by Mendoza *et al.* (Appendix A) show orbital density contour values for TM-TPP molecules with  $\theta = 61^\circ$ , and  $51^\circ$ . For the HOMO a strong contribution of upper methyl groups and a weak contribution of the internal pyrrole groups and methine bridges is calculated ( $\theta = 61^\circ$ ). Based on this and Figure 4.1,

where the four methine groups are clearly visible, it is concluded that for molecule 1 and 2 the degree of saddling has increased in comparison to the RT configuration. Not only are the protrusions of the methine bridges replaced by those of the tilted upward pyrrole units, but also the mesityl groups are weakly imaged. The saddling angle for molecule 2 is estimated  $\varphi=20^\circ$  based on STM images, which theoretically (page 18) is expected for  $10^\circ < \varphi < 20^\circ$ . For the diacid  $H_4TM-TPP^{2+}$  the lowest energy conformation was found at  $20^\circ$ , with  $\theta \approx 50^\circ$ .<sup>[89]</sup>

Molecule 3 possesses three bright protrusions associated with the mesityl rings. One of the mesityl groups is not visible. The pyrrole ring contribution changed to only one bright protruded region. Comparison of molecule 2 and 3 educates that not only the mesityl electron density increases in intensity, but also a change in alignment with respect to the porphyrinic core can be observed. For molecule 3 alignment to the methine bridges exists, whereas for molecule 2 alignment to both tilted upward pyrrole groups is preferred. This implicates that rotation of the mesityl groups occurs upon adsorption of a Cu-atom. It is expected that Cu-absorption is completed for molecule 3, whereas for molecule 2 a transition state exists. The absorbed Cu atom is not imaged on Cu(110) at these imaging conditions. This in contrast to cobalt porphyrins, that show a bright protrusion via the half filled Co  $d_{z^2}$  orbital that mediates tunneling at small negative bias'.<sup>[47]</sup>

In order to achieve core planarity by the absorption of a copper atom adjustment of opposite pyrrole units is essential. Both tilted downward pyrrole groups elevate towards parallelism with the substrate plane, and both tilted upward pyrrole groups decrease their saddling angle to zero. The first situation cannot lead to pyrrole-mesityl interaction for the upper *ortho*(6)-methyl (Figure 1.1b and Appendix A) groups are rotated above the porphyrin, whereas for the other situation the down *ortho*(2)-methyl groups are in direct substrate contact.

In addition to this quantum mechanical calculations by Okuno *et al.*<sup>[32]</sup> have shown that the potential energy barrier at the transition state is relatively small i.e. for non-substituted phenyl rings  $2.09 \text{ kcal.mol}^{-1}$ . Addition of substitutional groups increase the potential barrier slightly. It is shown that the steric hindrance, which prevents aryl-ring rotation can be circumvented by considerable porphyrin ring deformation. When the potential-energy barrier is passed a phenyl ring can exist in the same plane as the core. The rigid phenyl ring does not deform upon rotation. Furthermore Jarzecki *et al.*<sup>[217]</sup> calculated that the methine bridges ( $C_\alpha-C_{meso}$ ) and the  $C_\alpha-N-C_\alpha$  angles are sensitive to



the core size. In contrast the  $C_\beta$ - $C_\beta$  bond does not alter its length similar to the pyrrole rings, that behave as rigid units for which no significant changes are noticed.

The bright protrusion in the first quadrant of molecule 3 disappeared for molecule 4, the next phase in the conformational change. Instead of a distortion an extension of the core electron density by the mesityl group is observed. Again the three protrusions, one per remaining mesityl unit, can be identified. In order to explain the change in electron distribution, interaction of the down *ortho* methyl groups and the copper substrate need to be considered. It has been shown by Grill *et al.*<sup>[218]</sup> that it is possible to connect TPP molecules via brominated TPP. Deposition of  $Br_4TPP$  on Au(111) and subsequent heating results in activated molecules upon the dissociation of Bromine atoms. These activated radical fragments combine to form agglomerates. However, loss of bromide atoms was also observed during evaporation resulting in pre-activated molecules, indicating that it is not only substrate but also temperature dependent. In contrast sublimated TM-TPP molecules remain intact and interaction with the substrate was already observed for the saddled phase at RT. It is, therefore, possible that a heated substrate induces interaction of *ortho* methylic hydrogen atoms with copper (ad)atoms similar to halide-copper interactions, which result in organo-copper species as proposed by Anisimov *et al.*<sup>[219]</sup> and hence selective deprotonation. Then an electrophilic substitution type reaction<sup>[220]</sup> at the pyrrole  $C_\beta$ -H located in proximity to the activated and rotated mesityl group could occur, possibly via a reaction intermediate (molecule 3, Figure 5.6).

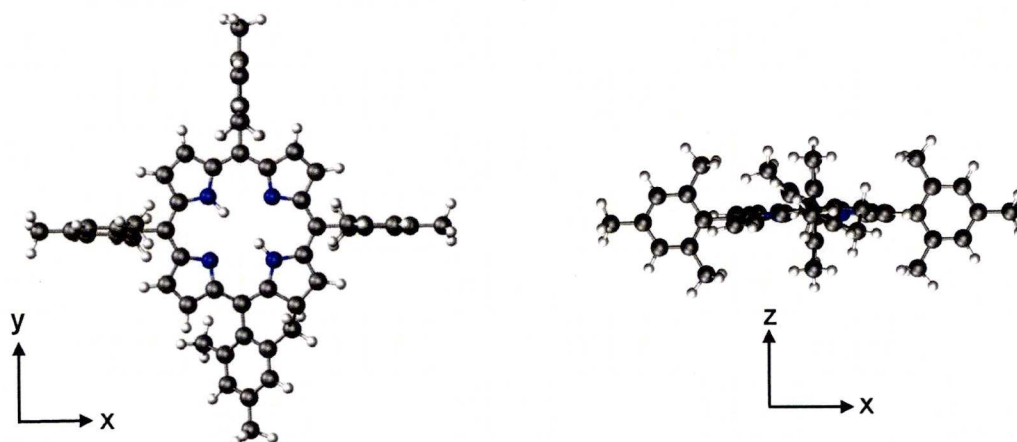


**Figure 5.7.** – VASP Calculations for another TM-TPP-radical (reaction intermediate) in vacuum with one hydrogen from an *ortho* methyl removed and a tilted mesityl ring.<sup>[72]</sup>



Figure 5.8 shows the interaction of a methyl-radical with the Cu(110) substrate based on theoretical calculations. It is visualised that elevation of substrate-atoms by methyl-radicals is possible, although the molecular conformation does neither represent the experimental results nor Cu absorption due to limitations in the method of calculation. Figure 5.7a is a reaction intermediate (molecule 3) calculated in vacuum, which is more stable than the former radical (I) without tilted ring in vacuum (-734.708 eV vs. -735.003 eV). It is, however, more stable (0.3 eV) to have radical I adsorbed than the reaction intermediate. Therefore it is expected that I is the precursor for the reaction intermediate. The other upper *ortho* methyl group, that in the saddled phase already points into the vacuum and hence has never been in direct contact with the substrate cannot undergo a similar reaction. Therefore only one *ortho* methyl group binds to the core. The other, unconnected, accounts for the asymmetric electron density profile.

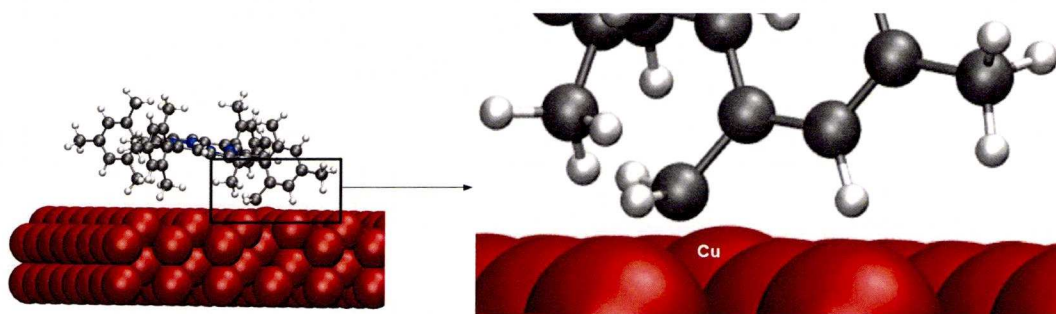


**Figure 5.8.** – VASP Calculations for a TM-TPP-radical (I) with a deprotonated *ortho*-methyl group pointing at the surface. A Cu atom is lifted from the substrate by  $\approx 0.16$  Å.<sup>[72]</sup>

The TPD-profile (Figure 5.5) confirms the gradual evolution of hydrogen atoms. Absorption of individual hydrogen atoms on Cu(110) cannot occur for this phase, for the desorption of hydrogen from Cu(110) is known to occur at temperatures  $\approx 340$  K.<sup>[221]</sup>

A similar sequence is observed for the third quadrant of molecule 4. Molecule 5 in frame C is almost identical to 4 apart from the protrusion associated with the pyrrole ring opposite to the protrusion in molecule 3. Molecule 5 in frame B however lacks electron density on a mesityl group. This suggests rotation of an additional mesityl group (frame C) and connection to a pyrrole unit with a deprotonated *ortho* methyl group.

Returning to the results presented in and Figure 5.2 and Figure 5.3 a confirmation of a sequential lighting up is found. It was found that quadrants 1 and 3 protrude significantly more frequent than the other two quadrants, for which no protrusions were

observed at relatively lower temperatures. It is expected that the ‘off’ molecules have completed the reaction sequence.

5.2. Intermediate: substrate-molecule interaction

RAIRS data for the intermediate phase of TM-TPP when absorbed on a substrate kept at 423 K is presented in (Figure 5.9). It has to be noted that the absorption peaks present in the low wavenumber ( $<1000\text{ cm}^{-1}$  region) are relatively difficult to assign correctly as a result of the elevated temperatures baseline correction in that region is unreliable. The spectra obtained are similar to the RT metastable phase. This suggests that the molecule absorbs planar, which is supported by the the ip mesityl absorption bands H and I (see also Section 4.1) and the relatively weak absorption bands P that belong to methyl-absorption modes. Mode L (see page 66) originates from  $\text{CH}_3$  and ip/oop ph vibrational modes. It can be extracted from the spectrum that the substrate and mesityl groups interact by band-broadening.

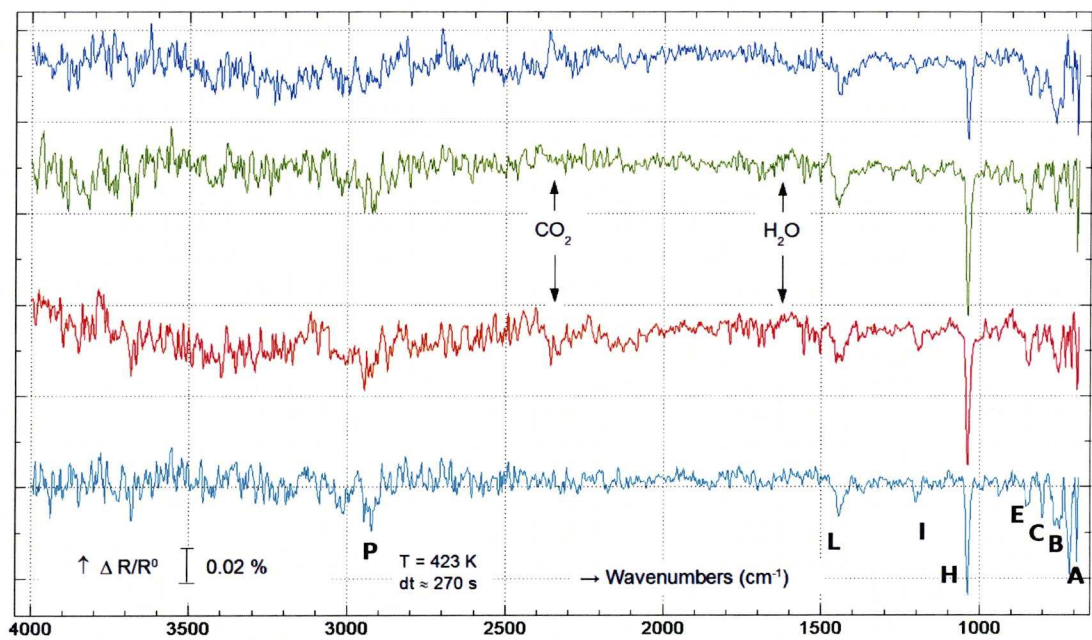
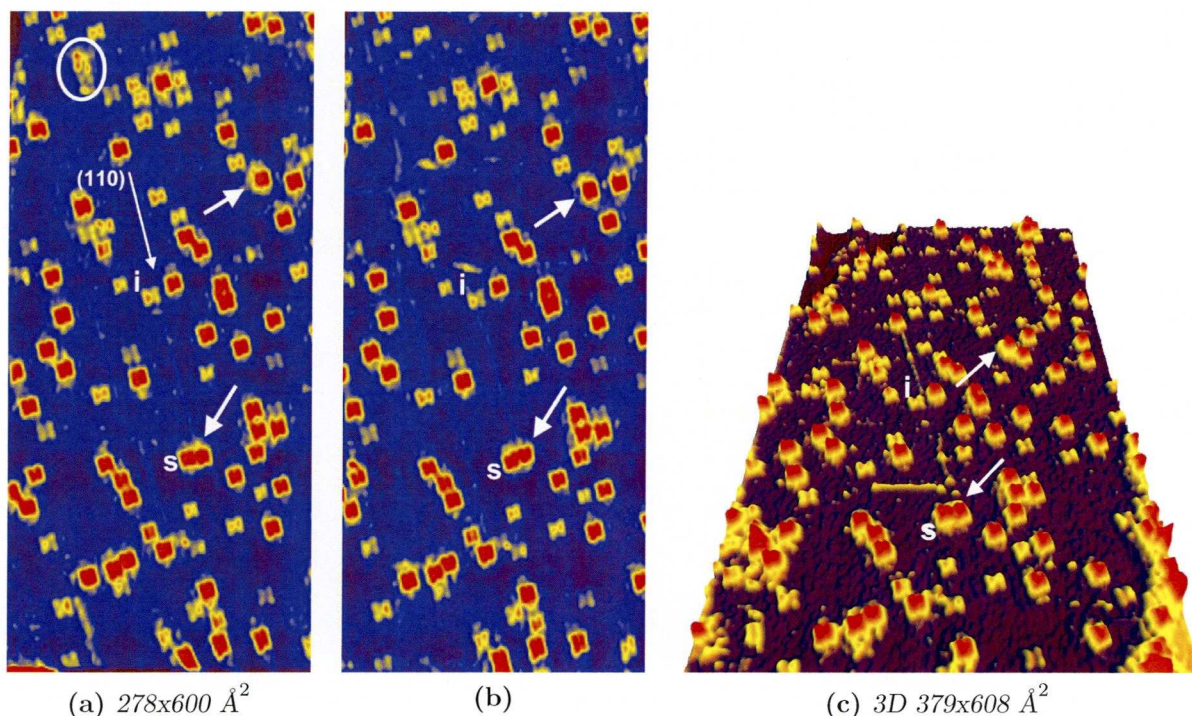


Figure 5.9. – TM-TPP RAIRS spectra obtained while depositing TM-TPP keeping the substrate at a constant temperature of 423K. Low to medium coverage.

A multi-step deposition on the copper substrate resulted in a co-existence of molecular conformations on the substrate. Figure 5.10 shows the simultaneous surface occupa-



tion for the intermediate and the RT phase. The first is represented by molecules that have a smaller apparent height. Saddled (RT) molecules are the bright protruded areas.



**Figure 5.10.** – STM images ( $\delta t=60s$ ) indicating the dynamic substrate behaviour ( $s$ =saddled,  $i$ =intermediate,  $V=-267$  mV,  $I=-330$  nA).

Self-assembly or self-organisation is not observed when both the intermediate (planar) and RT (saddled) conformation are mixed. However a difference with respect to a uniform molecular distribution at RT was noticed. This is indicated by white arrows, that point to two separate saddled TM-TPP molecules that diffuse in the  $\langle 110 \rangle$  direction. This is attributed to movement of substrate atoms. It is shown (circle) that reorientation of copper (ad)atom chains occurs frequently. A special example is the ad-atom trail, parallel to  $\langle 110 \rangle$ , that runs from two saddled molecules ( $s$ ) to a reaction intermediate ( $i$ ). In frame B some distortions appear and within a minute another ad-atom chain formed on a different substrate region. The original cluster disappeared. Molecular translation occurred simultaneously.

At the start of this chapter Figure 5.1 was presented. Figure 5.11a was obtained after  $\approx 230$  minutes of HT-STM at  $\approx 383$  K followed by a extended cooling period of sample and STM ( $\approx 780$  minutes) in which the temperature dropped from 383 K to 323 K. This resulted in a higher degree of self-organisation (cf. Figure 5.11b) after a moderate anneal (fifteen minutes) by resistive heating. Aligned rows of molecules extended in both



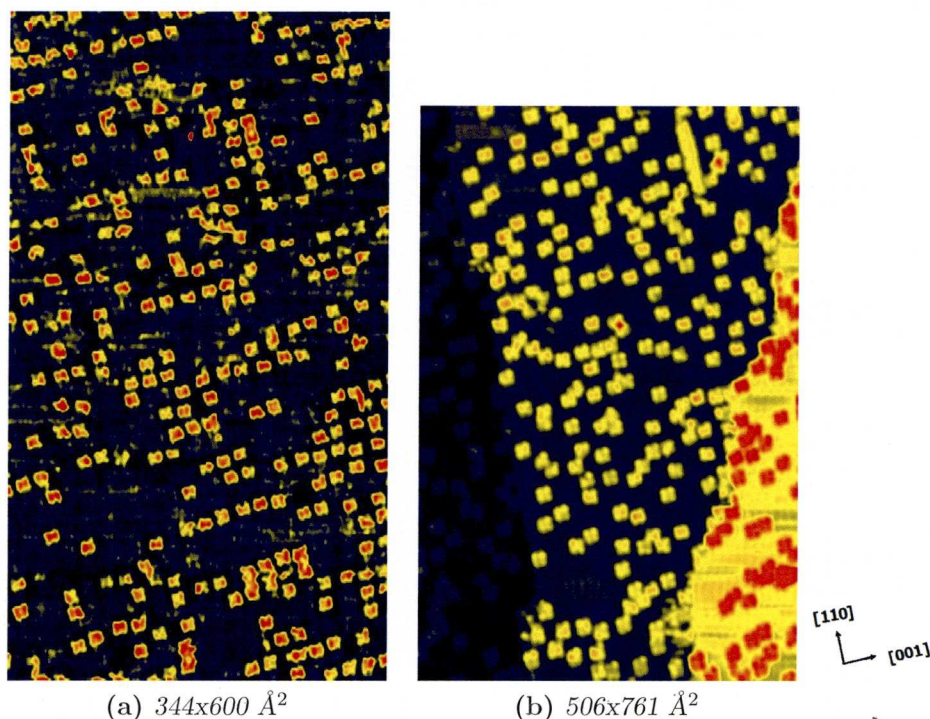


**Figure 5.11.** – **a)** STM topographical image visualising limited self-organisation after repeated mild heating.  $V=610\text{mV}$ ,  $I=0.320\text{ nA}$ ,  $T_{STM}=323\text{K}$  and **b)** a moderate anneal by resistive heating,  $V=-761\text{mV}$ ,  $I=-0.470\text{ nA}$ .

main copper directions are introduced, emphasising the influence of a gradual increase or decrease in temperature on the substrate properties (see also Chapter 7). It is, therefore, concluded that the absorption of TM-TPP at elevated substrate temperatures does not occur via a metastable phase and hence is dissimilar to RT absorption. Moreover a transition temperature ( $T < \text{RT}$ ) exists for which the metastable conformation found at RT is the preferred thermodynamical stable molecule.

### 5.3. Maximised activation: STM

Figure 5.12a summarises the conformational change discussed in the previous sections. A non-standard tip-state enables distinction of three methyl groups in a saddled configuration. These are marked by black dots. Tilted upward pyrrole groups are represented by purple dots. The depression near molecule A is caused by substrate rearrangement as a result of mesityl group rotation. This is visible for molecule C of which a mesityl protrusion associated with an upper ortho methyl disappeared. A rotation that adjusts one of the mesityl legs. For the reaction intermediate a single black dot is the mesityl

group and a green dot represents a lighting up event, described previously. The leg closest to B images significantly smaller than the other leg visible, suggesting different conformations. It shows that diametrically opposite legs image similar.

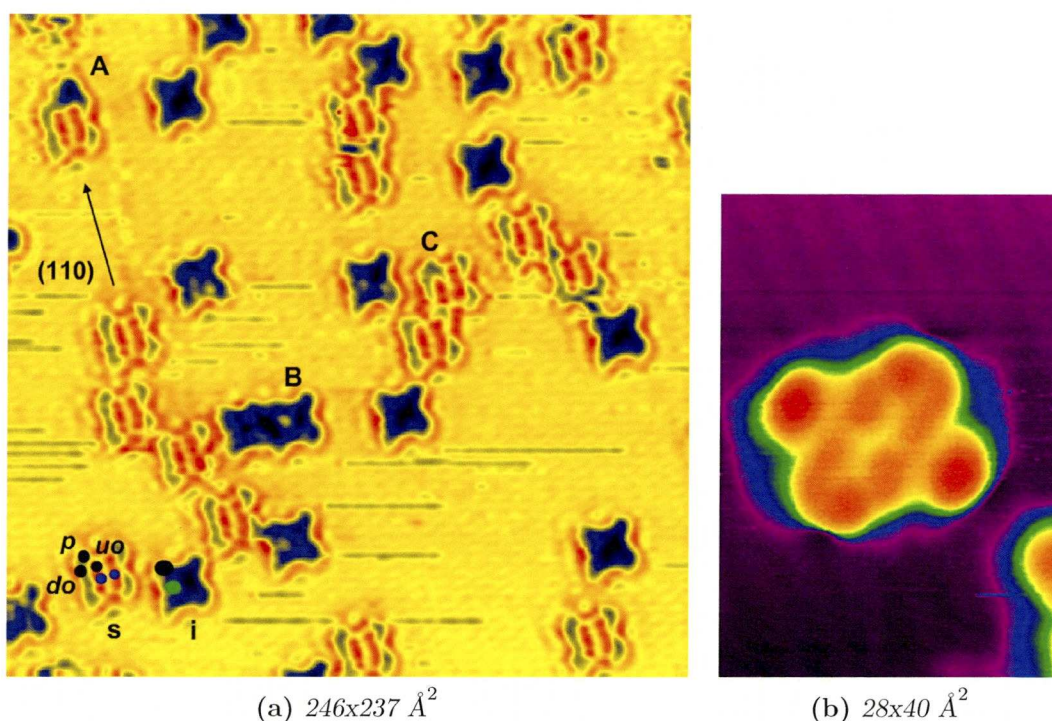


**Figure 5.12.** – **a)** STM image, acquired with an unusual tip state, that shows the molecular temperature dependent conformational change. ( $V=-267$  mV,  $I=-0.320$  nA,  $p$ =para,  $uo$ =upper ortho,  $do$ =down ortho,  $s$ =saddled,  $i$ =intermediate) **b)** A molecule imaged after a maximised anneal. The copper corrugation is visible ( $V=-423$  mV,  $I=-0.230$  nA).

Further conformational changes occur when the sample is heated to maximised temperatures i.e.  $\approx 500$  K (Figure 5.12b). An extended period at temperatures between 450 and  $\approx 500$  K gives nano-structures shown in Figure 5.13a. A variety of di,tri and multi-functional (branched) networks co-exist at the substrate. Monomers represent the minority. Dimers were already signalled for the intermediate phase (Figure 5.2). The majority of the surface coverage was, however, attributed to monomers. A gradual decrease of monomers is observed as function of time and thermal energy. Control of the reaction at the nanoscale turned out to be exceptionally difficult. Repeated dosing and annealing of a low coverage results in connection of, and to branched structures obtained in the previous heating cycle. Figure 5.13b presents the result of such a sequence. Multiple grids, which consist of four to eight fragments are connected by rows and branched networks. The molecules have four possibilities to connect to another molecule viz. via *para* methyl groups to form covalently linked networks. Also observed by Grill *et al.*



and discussed previously on page 79. It is, therefore expected that the bond that is created is covalent of nature. Usually weak intermolecular forces are the driving force of self-assembled systems. These consist of non-covalent interactions ( $5\text{--}40\text{ kJmol}^{-1}$ ), that are reversible and weaker than covalent bonds ( $>200\text{ kJmol}^{-1}$ )<sup>[2]</sup>. Reversibility is not present in self-organised systems, that often require an external energy source and hence is dissipative.<sup>[222]</sup>

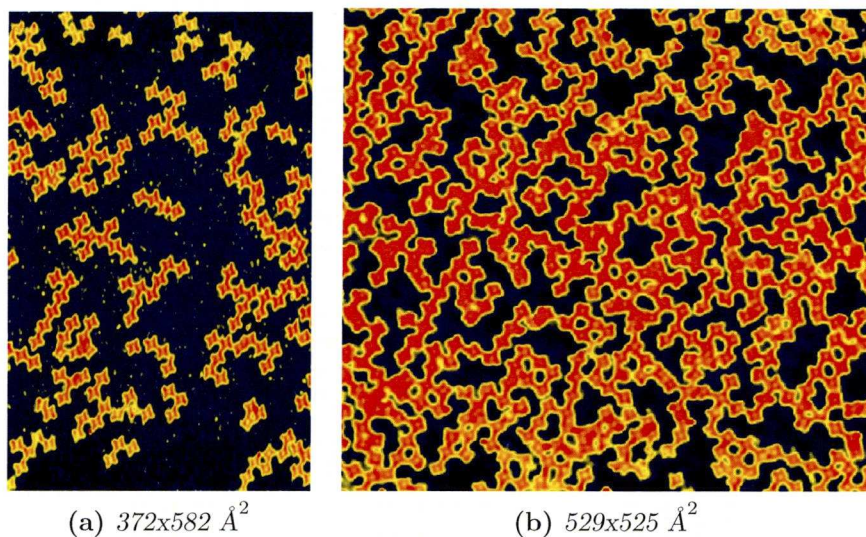


**Figure 5.13.** – High coverage topographical image showing connected grids and branched networks obtained after repeated dosing and an extended anneal for an hour.  $I \approx -160\text{ nA}$ ,  $V \approx -593\text{ mV}$ ,

In order to test this hypothesis a sample was investigated with HT-STM at  $\approx 400\text{ K}$  (Figure 5.14). If non-covalently bonded i.e. weak bond strengths, networks separate in individual TM-TPP molecules, then the sequence of images confirms the opposite. The trimer indicated by the white arrow, supposedly intermolecular covalently bonded, diffuses over the substrate along  $\langle 110 \rangle$ . In image (c) the top molecule deviates from the others to interact with one of TM-TPP fragments in the J-shaped network next to it, which shows the flexible nature of the bond. An ethylene linkage (single bond), which offsets the diagonal axes of joined molecules in contrast to a linear ethyne bridge. The last frame (e) shows that the trimer returned intact. Not only the molecules in the blue circle but also the single fragments in proximity of the trimer diffuse at higher speeds and over larger distances. Diffusion of branched molecular aggregates was never observed at these temperatures.

A similar situation was observed for another linear molecule built with four TM-TPP molecules Figure 5.15. No relocation was observed between frame (a) and (b) despite a



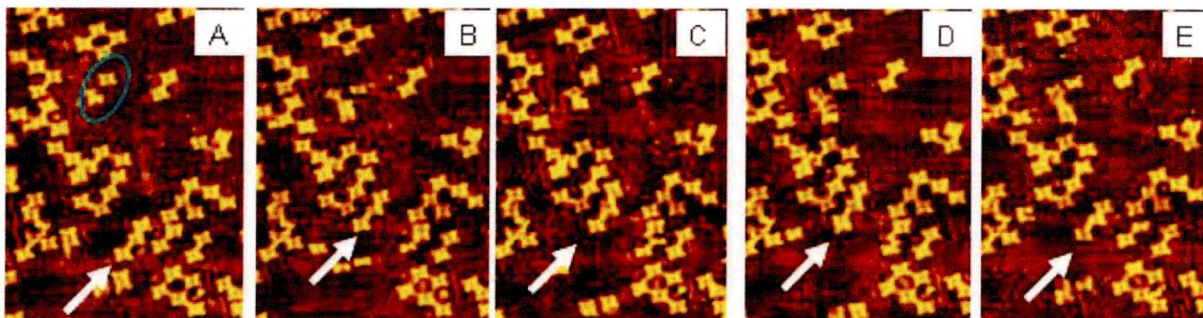


**Figure 5.14.** – Time resolved STM images of annealed TM-TPP on Cu(110) at 393K. Timespan 200 s. Mobile trimers (indicated by white arrow) and monomers (blue circle in A)

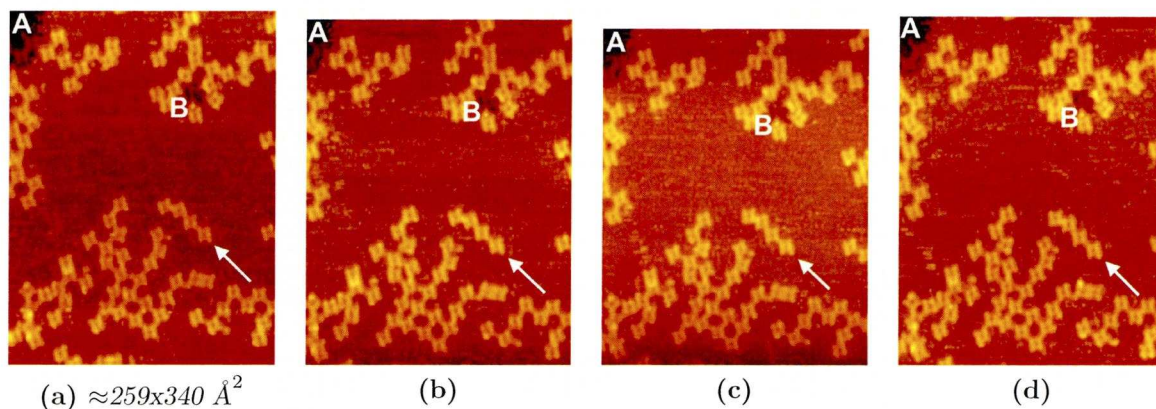


**Figure 5.15.** – A mobile tetramer (white arrow),  $dt \approx 60s$ ,  $V = 707 \text{ mV}$ ,  $I \approx 0.150 \text{ nA}$ .

dynamic substrate visualised by A (step edge) and B. In frame (c) the molecule moves as a complete unit in the direction of B, during which the linearity increases. The diffusion and linearisation becomes apparent by increased distance between the two most left fragments and one of the ‘arms’ of the grid below. A frame later (d) this distance is decreased while the molecule remains its shape. The displacement of the complete tetramer is perpendicular to that of the trimer and is significantly smaller in amplitude. Again one of the fragments exposed its flexibility.

The influence of the substrate is amplified by another experiment. Figure 5.16 presents time resolved images. Translation of a dimeric unit was followed. The white arrow indicates the dimer, which oscillates along  $\langle 110 \rangle$ , similar in magnitude and along the same main copper axis previously discussed for the trimer. A variety of events is notable at the substrate, indicated by A to D. A designates a monomer that, if followed from frame j to l shifts back and forth under the influence of substrate rearrangement at the righthand-side. Another occurrence of a dynamic substrate is visualised by B. The space



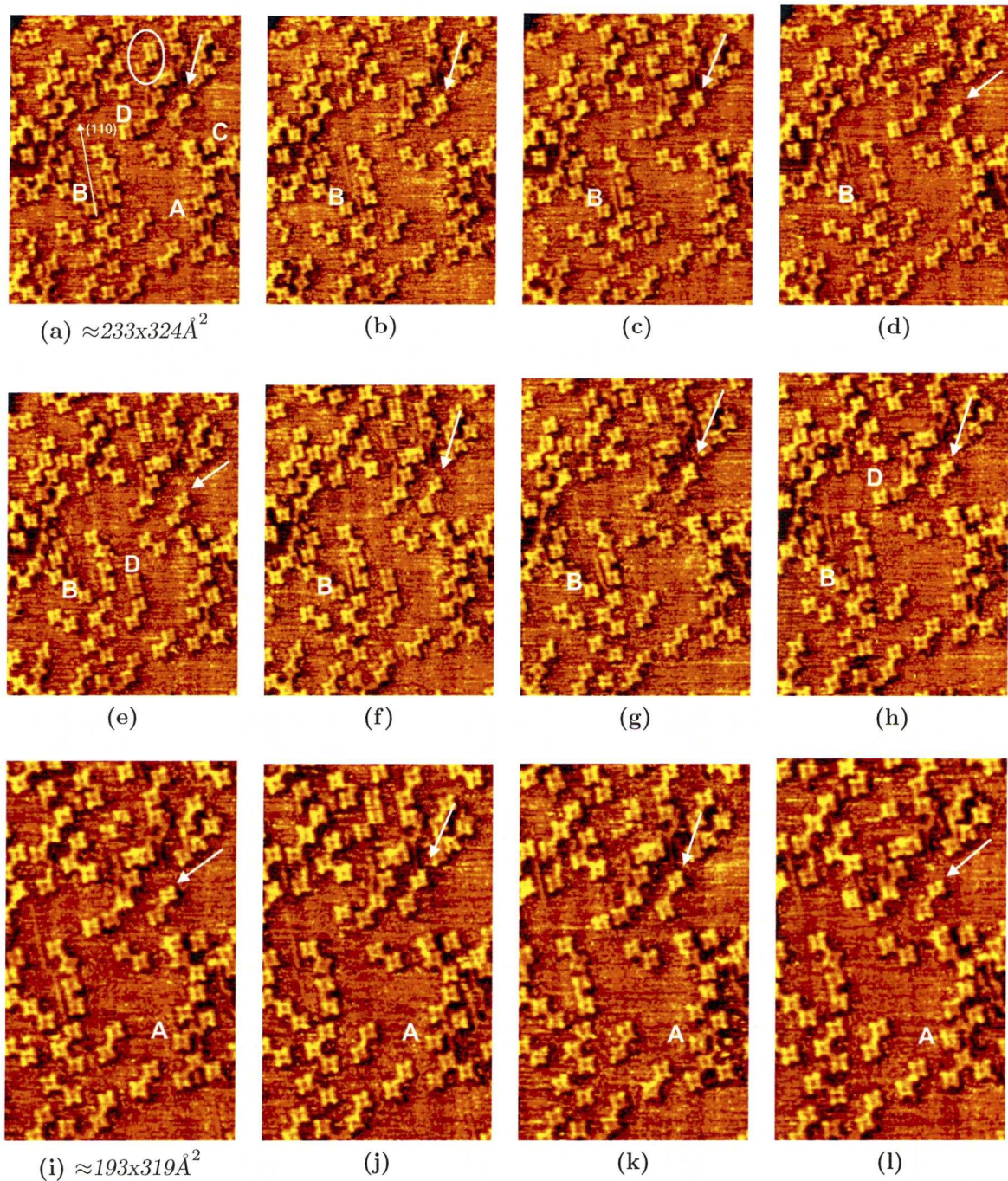


**Figure 5.16.** – A mobile dimer (arrow),  $dt_{a-l} \approx 1020 \text{ s}$ ,  $dt_{a-h} \approx 320 \text{ s}$ ,  $dt_{i-l} \approx 700 \text{ s}$ ,  $V = 493 \text{ mV}$ ,  $I \approx 0.220 \text{ nA}$

not occupied by molecules contain ad-atom chains parallel to  $[110]$  that relocate (frame a to h, see also patch C for atomic resolution). D indicates a monomer that traverses the substrate guided by a copper row only limited by presence of other molecules. Moreover other and similar dimer configurations are located at the substrate. These, however, are



immobile suggesting that for diffusion of linear polymers a typical atomic and molecular environment is required. Furthermore at these experimental conditions branched structures remain fixed at their position also indicating that molecule-substrate interaction steer diffusion. The circle indicates two molecules that also move. It has to be noted that imaging of these molecules is relatively difficult (cf. D image e) therefore higher diffusion speed is expected and hence these are considered monomeric.

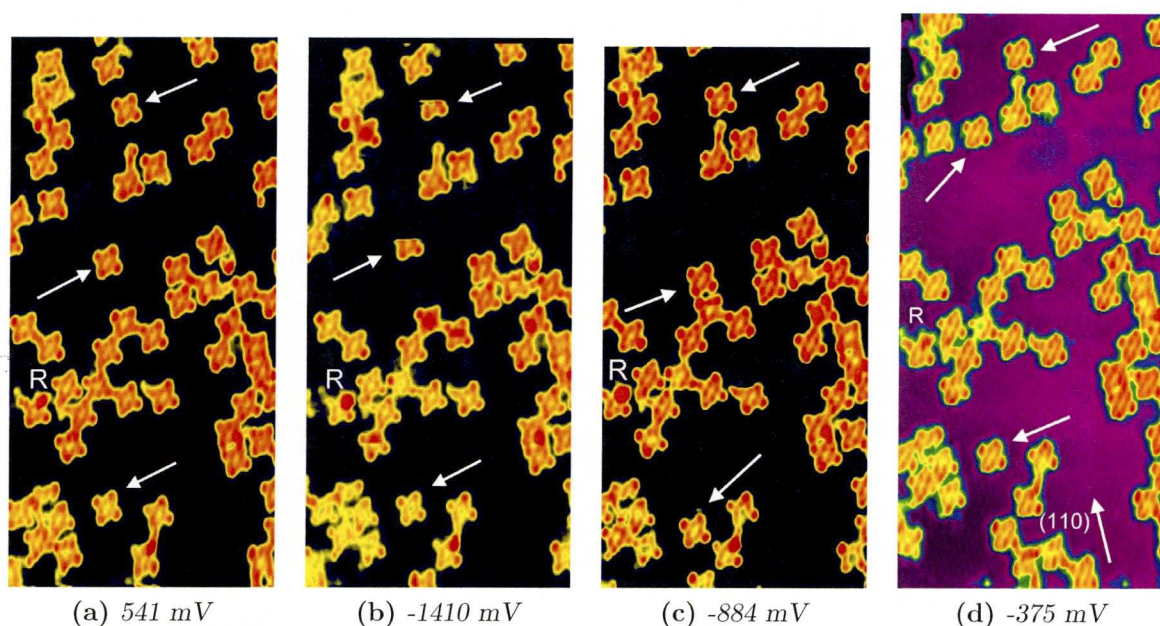


**Figure 5.17.** – Tip induced molecular motion. The images are selected from a sequence and therefore separated multiple frames apart. Image size  $\approx 150 \times 300 \text{ \AA}^2$   $I \approx 0.250 \text{ nA}$

A different tip-induced type of diffusion was observed for monomers (Figure 5.17). A positive bias did not result in any molecular ‘jumps’, scanning at negative bias  $< 1000 \text{ mV}$  induced molecular movement along  $\langle 110 \rangle$ . The white arrows in image (a) point at three different monomers fixed at their position. A bias and polarisation change introduce relocation of all these molecules (image b). By applying  $-2000 \text{ mV}$  a few frames before image (c) was scanned at  $-884 \text{ mV}$  molecular diffusion reoccurred. All three molecules move in the same direction towards the nearest polymers that rest on the substrate at these bias conditions. Generating a translation in the opposite direction (image d) was accomplished by another scan at  $-2000 \text{ mV}$ . The copper corrugation is visible in the last image (see also Figure 5.12b). R denotes a molecule of which the para methyl group is expected to interact with the substrate.

Figure 5.18 gives the LDOS for both individual molecules and polymerised branched networks. It is a magnification of the central area of Figure 5.17. Again tip induced



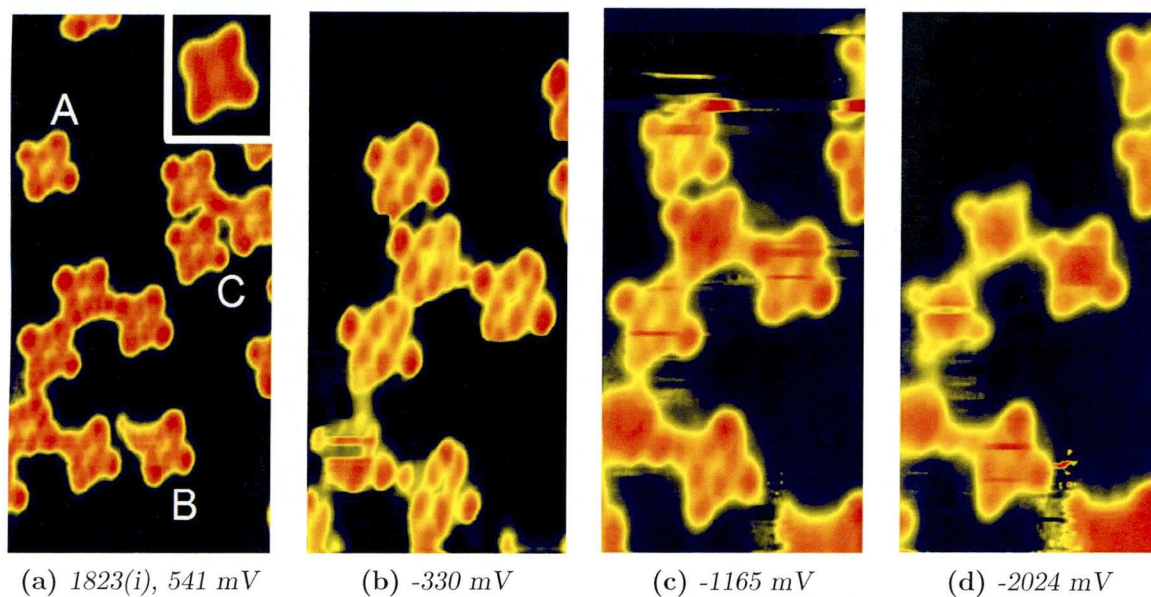


**Figure 5.18.** – High temperature phase of TM-TPP on Cu(110), occupied and unoccupied states. Inset(i)  $22 \times 27 \text{ \AA}^2$  (a)  $76 \times 155 \text{ \AA}^2$  (b-d)  $52 \times 108 \text{ \AA}^2$   $I \approx 0.250 \text{ nA}$ . (image c and d are successive frames)

diffusion of molecule A was observed. For standard scanning conditions, applying a negative voltage of  $\approx 330 \text{ mV}$  probing the occupied states of the sample, the two largest and most bright protrusions are associated with diametrical opposite mesityl rings, which due to planarity couple with the substrate.<sup>[196]</sup> Molecule B relocates towards one of the mesityl groups of the branched molecule next to it. One of the mesityl groups images atypically suggesting a different conformation. Based on Figure 5.17d in which the same molecule is imaged at submolecular resolution, it is proposed that substrate rearrangement decouples it. Therefore the occupied states of the mesityl group are visualised. Several theoretical studies were devoted to the interaction of benzene with metal atoms. In 1999 Dargel *et al.*<sup>[223]</sup> performed HF, MP2 and DFT calculations from which it was concluded that the  $\text{Cu}^+$  preferred binding site is six-coordinated. The  $\pi_{\text{off}}$  and  $\sigma$  coordination were found stable with DFT (B3LYP and BLYP) functionals (Figure 5.19).

More recently Yi *et al.*<sup>[224]</sup> performed calculations which show that the  $\pi_{\text{cen}} \eta^6$  with  $C_{6v}$  symmetry is preferred (MP2, QCISD), although localisation of the cation over the other coordination sites was also possible (DFT B3LYP, PBE). For a  $C_{6v}$  configuration, the binding interaction between the benzene ring and the cation are considered to be purely electrostatic and inductive due to a relatively large separation in ionisation energies. The  $\pi_c$  configuration however shows an increase in covalent contributions by

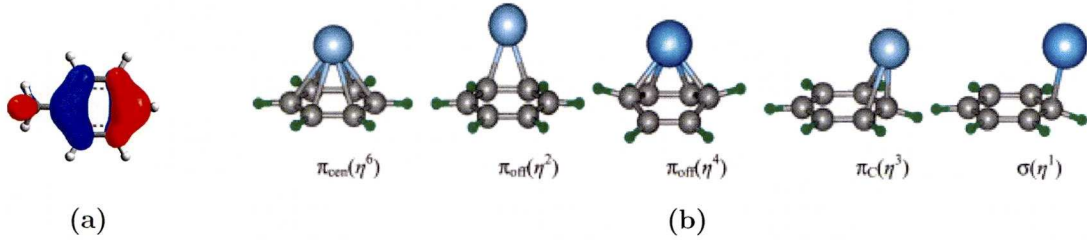


**Figure 5.19.** – a) HOMO orbital configuration of toluene based on Arguslab AM1 calculations<sup>[180]</sup> b) Transition metal ( $M^{n+}$ ) binding sites for benzene with  $\eta^n$  the coordination number.<sup>[224]</sup>

s-occupations. It is expected that a  $\pi_{cen}$  coordination is the origin of the bright protrusions for the two diametrically opposite mesityl groups. Contrast enhancement is possibly caused by s or d-wave surface states and the mesityl  $\pi$ -system overlap. The other mesityl groups, show asymmetric brightening and are therefore uncoupled and at an angle with respect to the substrate. The four protrusions at the centre of the molecule are attributed to electron density states on the four pyrrole units.

The most pronounced change in LDOS occurs when  $V < -1500$  mV. For these bias conditions the contribution of the porphyrinic core to the electron density increases, which has its origin in an absorbed Cu-atom. Interestingly, equivalent bias settings also induced the molecular motion known as electric field manipulation.<sup>[225]</sup> It is therefore expected that tunneling into the occupied copper orbitals probably also mediates substrate bonding. Lu *et al.*,<sup>[50]</sup> who carried out experiments on ad-layers of CoPc and CuPc, showed that the  $d_{z^2}$ ,  $d_{xz}$  and  $d_{yz}$  orbitals of Cu in contrast to Co are situated  $< 2$  eV below the HOMO. These orbitals have the largest out of plane projection and are therefore thought to participate in coupling to the substrate. Although Appendix E presents frontier orbital calculations for planar TM-(Cu)-TPP in vacuum. It is expected that the orbital configuration of the central atom approaches the situation on the surface. Also supported by Rosa *et al.*<sup>[226]</sup>, who calculated that a change of ligand-framework from Pc to P does not alter the metal macrocycle interactions drastically. It is therefore proposed that in spite of the molecule's conformational change, metal orbital configurations can be compared to those in the appendix. This also shows an energy difference of  $\approx 2$  eV between the SOMO (Single Occupied Molecular Orbital), which is the anti-bonding combination of the Cu  $d_{x^2-y^2}$  and N lone pair orbitals, and the two degenerate metal molecular orbitals ( $-4.99$  eV) for which  $d_{xz}$  and  $d_{yz}$  contribute. This also implicates that the SOMO does not couple with the substrate and therefore does not contribute to the LDOS profile.



A typical aspect of image (d) is that not all the molecules of the network possess a bright core. This is attributed to a different adsorption site. Furthermore frame (c) shows two molecules that participate in the grid and that have increased core brightening. This is attributed to pyrrole groups that temporarily couple with the substrate as a result of molecular and atomic movements induced by the applied bias.

Finally molecule C interacts with a polymer and remains fixed when the bias is increased. It is assumed that although the molecule appears monomeric creation of another covalent bond cannot be ruled out. This is however not frequently observed.

## 5.4. Maximised activation: RAIRS

Figure 5.20 presents RAIRS spectra for the high temperature TM-TPP phase at different substrate temperatures. Again it has to be noted that the absorption peaks that are present in the low wave-number  $<1000\text{cm}^{-1}$  region are unassigned as a result of the elevated temperatures and baseline drift. The results are the continuation of the substrate kept at 423 K (Figure 5.9). The infra-red results will be discussed in three stages. First the low wave-number region that extends to  $\approx 1600\text{ cm}^{-1}$  after which the high wave-number absorption bands ( $>2500\text{ cm}^{-1}$ ) are explained. Finally the changes that occur in the mid wave-number region ( $1600\text{-}2500\text{ cm}^{-1}$ ) will be outlined.

Increasing the temperature with 45 K to 468 K introduces changes in the spectrum. Many vibrational modes that were not active appear indicating symmetry and conformational changes. Band H is now accompanied by a small shoulder ( $I^*$ ). Upon addition of thermal energy to 483 K and subsequent temperature decrease to RT this absorption band at  $1038\text{ cm}^{-1}$  disappears and the shoulder becomes a broad band at  $\approx 1066\text{ cm}^{-1}$ . This is an oop ph mode perpendicular to the  $C_{meso}$  bond  $\Psi_8''$  and therefore, whereas H was associated with an ip ph and  $\text{CH}_3$  rocking modes.  $L_1/L_2$  show similar behaviour to H and are also related to mesityl asymmetric vibrational modes (see page 67). Therefore rotation is inevitable. However, with respect to the infra red absorption spectra of both TM-TPP and TM-Co-TPP (Section 6.2) a difference can be noticed. In these cases band L remains of similar strength. Therefore it can also be concluded that the number of methyl groups decrease or that these are parallel to the substrate (surface selection rule). On the other hand one would expect a similar change for the vibrational modes K and J, which are also of methyl origin (symmetric). Mode I, a single absorption peak at 423K, initially transforms in a broad band that extends from  $1140\text{-}1250\text{ cm}^{-1}$ . It,



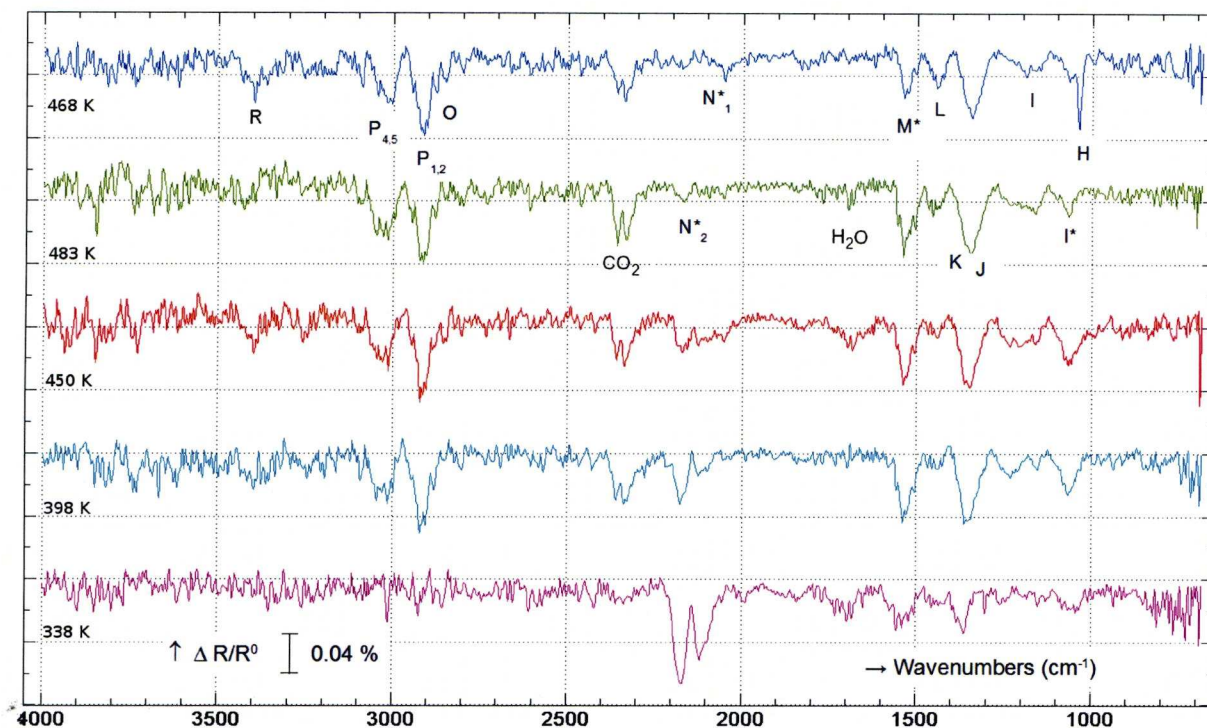


**Figure 5.20.** – RAIRS spectra acquired at different temperatures for the TM-TPP high temperature phase. Total acquisition time  $\approx$  22 minutes

however, diminishes when cooling down and two new vibrational modes (1151 and 1224 cm<sup>-1</sup>) appear that have maximum intensity at 398 K and are still visible at RT. The first mode originates from an oop ph  $\Psi_7''$ , whereas the assignment of the other mode is not exactly clear.

Furthermore the absorption bands O and P, that are associated with CH<sub>2</sub> and CH<sub>3</sub> modes decrease after cooling down. Similar to the intermediate state a the lack of amplitude between 2950 and 3000 cm<sup>-1</sup> is visible, which, in the RT phase, was assigned to P<sub>3</sub> being a CH<sub>3</sub> stretching mode. This is also confirmed by the change in aromatic C-H peak sharpness  $P_4/P_5$ . A relatively broad absorption range is present at higher temperatures, whereas at temperatures approaching RT a sharp band remains. Another sharp band that is possibly augmented by J|K at elevated temperatures becomes visible at  $\approx$ 1300 cm<sup>-1</sup> due to a small shift of J|K. This band is assigned an aromatic C-H oop bending mode.

Interestingly at 468 K the mid wave-number region shows absorption bands in a region normally associated with carbon dioxide and water from the external auxiliary optics. These were not present at 423 K. Also a vibrational mode N<sub>1</sub><sup>\*</sup> at  $\approx$  2050 cm<sup>-1</sup> is visible. None of these modes are porphyrinic of origin and are due to in situ CO<sub>2</sub>(g),

$\text{H}_2\text{O}(\text{g})$  and  $\text{CO}(\text{g})$  [227]. This indicates that as a result of elevated temperatures decomposition products from the sample surroundings exist. It is expected that the origin of the contamination can be related to tartaric acid Figure 5.21. This molecule is known to sublime at 370K. Moreover the spectrum obtained at 338K shows unambiguously absorption modes situated around  $1700\text{ cm}^{-1}$ . No porphyrinic modes are known to exist in this region. Also  $\text{H}_2\text{O}$  vibrational modes can be excluded for  $\text{CO}_2$  disappeared. It is therefore assigned to  $\text{C}=\text{O}$  stretching modes that originate from  $\text{COOH}$  groups. Furthermore at 468 K bands (R) exist around  $3400\text{ cm}^{-1}$  and  $3200\text{ cm}^{-1}$  that are alcoholic OH and acid OH vibrations respectively. [228] Based on this the bands that exist in the wave-number region that surround J and K are attributed to vibrational modes which originate from alcoholic OH groups (J) and the symmetric  $\text{COO}$  stretch (K). Especially since these modes are strong similar to band  $\text{M}^*$ , the asymmetrical carboxylate stretch.

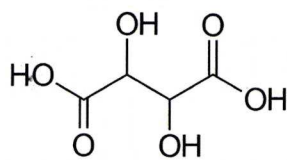


Figure 5.21. – Tartaric Acid

The absorption bands  $N_2^*$  that gradually increase after the maximum substrate temperature is passed are found in the region where  $\text{C}\equiv\text{C}$  [174] and  $\text{Cu-CO}$  [227] vibrations exist. As a result of the surface selection rule the presence of a triple bond absorption mode seems unfavourable. Hence it is assigned to a  $\text{CO}$  vibrational mode perpendicular to the substrate. After the substrate has reached RT these are relatively strong and broad absorption bands, which suggests participation in a network. The mode at  $2172\text{ cm}^{-1}$  is already visible at 483 K, whereas the other mode ( $2117\text{ cm}^{-1}$ ) appears while cooling down ( $<450\text{K}$ ). It initially spans a broad absorption region attributed to a dynamic substrate at elevated temperatures.

The desorption temperature of individual  $\text{CO}$  molecules on  $\text{Cu}(110)$  is  $\approx 220\text{ K}$  [229]. Therefore adsorption cannot occur for  $T > 338\text{K}$ . Also reception of a  $\text{CO}$  molecule on the central  $\text{Cu}$ -atom of TM-Cu-TPP seems impossible, although the desorption temperature of  $\text{CO}$  is increased when adsorbed on  $\text{Ni}(110)$  (450K) [120] and on 0.30-nm-thick-Pd-deposited  $\text{Cu}(110)$  (390K) [229]. It is assumed that if  $\text{CO}$  reception on the porphyrinic network occurs its absorption properties are reflected by the absorption band at  $2117\text{ cm}^{-1}$ . It is, however, more likely that a reaction between tartaric acid (fragments) and the methyl-groups of the porphyrin took place. Presumably via deprotonated hydroxyl



groups that create a covalent bond. As a result of mesityl ring planarity it is expected that the resulting  $\text{-C-O-C-}$  bond is parallel to the substrate. This automatically expects the carbonyl group perpendicular after rotation and interaction with the substrate. The earlier contribution of mode  $2172\text{ cm}^{-1}$  to the spectrum is possibly caused by a connection for which the carbonyl group already is oriented perpendicular to the substrate showing limited substrate-molecule interactions.

Most studies of CO interaction and Cu-substrates find adsorption for the wave-number region that extends from  $\approx 2000$  to  $2090\text{ cm}^{-1}$  associated with on top absorption. However if CO adsorbs on stepped surfaces<sup>[230]</sup> and copper clusters<sup>[229]</sup> this wave-number exceeds  $2100\text{ cm}^{-1}$ . Moreover Bobrov *et al.*<sup>[227]</sup> report that absorption bands are dependent on the amount of copper in a sample. Therefore it is proposed that the original copper corrugation is disturbed and absorption occurs on a locally disordered (cluster-like) substrate.

It has to be noted that the presence of tartaric acid at the substrate resulted in unexpected reactions and interactions, which subsequently increase the complexity of the absorption spectrum. It is however possible to confirm the existence of networks and the accompanying conformational change of the original TM-TPP molecule.

## 5.5. Model of covalently linked TM-Cu-TPP on Cu(110)

From the previous sections a relatively accurate model of the chiral molecules and chiral nano-structures can be extracted. It has to be noted that the model shown in Figure 5.13 is a prediction instead of calculated results. Presented is a heptameric grid, with four molecules that create a chiral cavity. One of the molecules (numbered) is, upon linkage, situated above the second substrate layer. The porphyrinic central copper atoms adsorb at the long-bridge site. This is based on the enhanced tunneling pathway observed previously. However occasionally adsorption on the 4-fold hollow site was observed, which results in a dim core. These properties result in translation of monomeric and linear polymeric units connected via A over significantly larger distances along the close packed substrate rows than in the other corrugated direction. Diffusion of branched molecules was not observed, which is attributed to substrate interaction when bond B is introduced to a linear network.



Moreover the space-filled atoms on the porphyrin fragment at the righthand-side of A (Figure 5.22) show the origin of the bright protrusions. It also highlights the origin of the other protrusions visible in the STM image(Figure 5.12)b i.e. the density of states on the pyrrole groups and those extended by phenyl contribution.

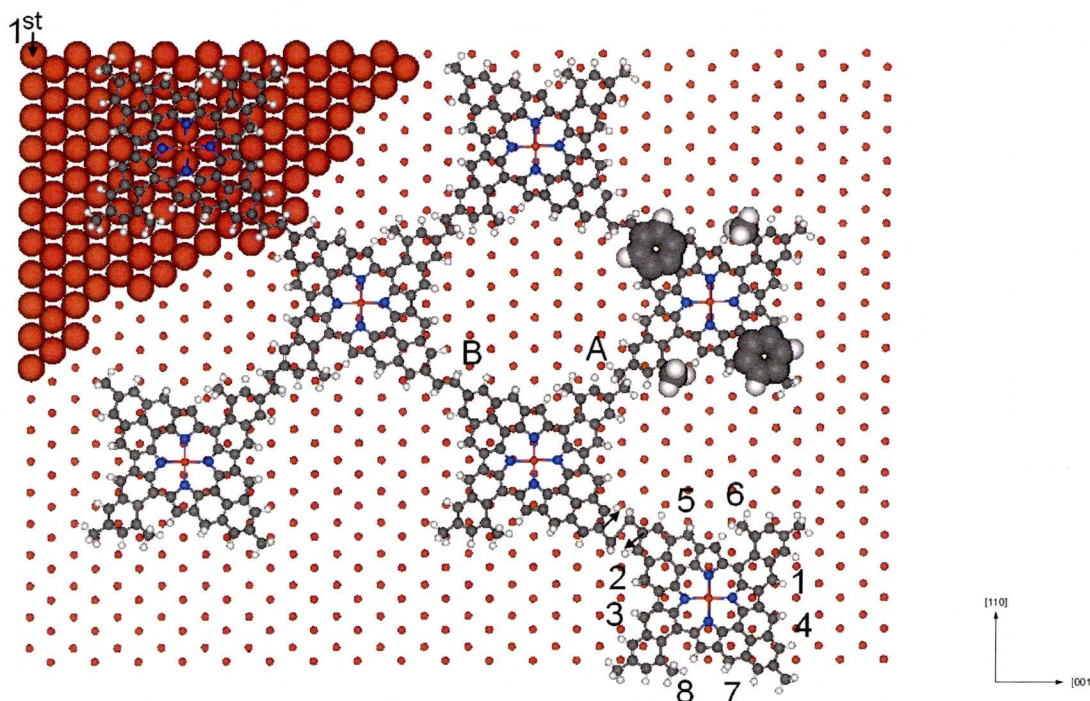


**Figure 5.22.** – Model of the nanostructures created by annealing TM-TPP on Cu(110) to 500 K for >30 minutes.

All the molecules that compose the network possess the same chirality. Based on the connection sequence between pyrrole and *ortho* methyl and nomenclature made for spiral galaxies<sup>[231]</sup> it is proposed that the individual molecules have trailing arms and therefore are left-helical. It can be derived from the STM experiments that the reaction starts in quadrant 4 and/or 2 (same numbers). During the reaction cycle the methyl groups originally present at place 1 to 5, and 7 react all, whereas the methyl groups present at place 6 and 8 do not connect. Due to the significantly more lightning up of quadrants 1 and 3, it is expected that the reaction terminates at these positions.

The existence of a saddled phase and subsequent copper incorporation appears to be essential for the chirality induced. Similar experiments carried out on TM-Co-TPP (Chapter 7), which is planar and pre-metallated yield a-chiral symmetric molecules in the networks formed.

## Chapter 6.

# Adsorption of TM-Co-TPP on Cu(110) at 298K

The former two chapters presented the interplay between Cu(110) substrate and the, thereby, adapted  $D_{2h}$  saddled free-base TM-TPP molecules. Copper atom incorporation was one of the most profound conclusions and essential for the change to a chiral  $D_{2h}$  flat geometry. In order to study the effect of a pre-bound metal-atom, a metallated (cobalt) version of TM-TPP was synthesised by Amabilino *et al.*<sup>[178]</sup> TM-Co-TPP exhibits core-planarity<sup>[84]</sup> and is therefore classified  $D_{4h}$ . This chapter and the next chapter present the results obtained for TM-Co-TPP at RT, intermediate and high temperature conditions, respectively.<sup>1</sup> The current chapter starts by explanation of STM results after which RAIRS data will be clarified.

### 6.1. STM

TM-Co-TPP deposition on Cu(110) analysed by STM for a coverage of  $\approx 1$  ML is presented in Figure 6.1a. No long range self-assembly is observed. The broad bright protrusions visible, are associated with several molecules adsorbed on the first layer. Moreover dark patches are visible (black circles), which contain molecules of different geometry. The top left region of the image shows a step edge. Similar to TM-TPP, TM-Co-TPP molecules do not have a preference for agglomeration at step edges.

---

<sup>1</sup> Unless otherwise stated all STM images and RAIRS Spectra presented are acquired at constant current (STM),  $T = 298$  K and a base pressure of  $\approx 5.0 \times 10^{-10}$  mbar and  $\approx 2.0 \times 10^{-9}$  mbar while dosing the molecules. Doser settings can be found in Section 3.6.1. Colourcodes on page 1.



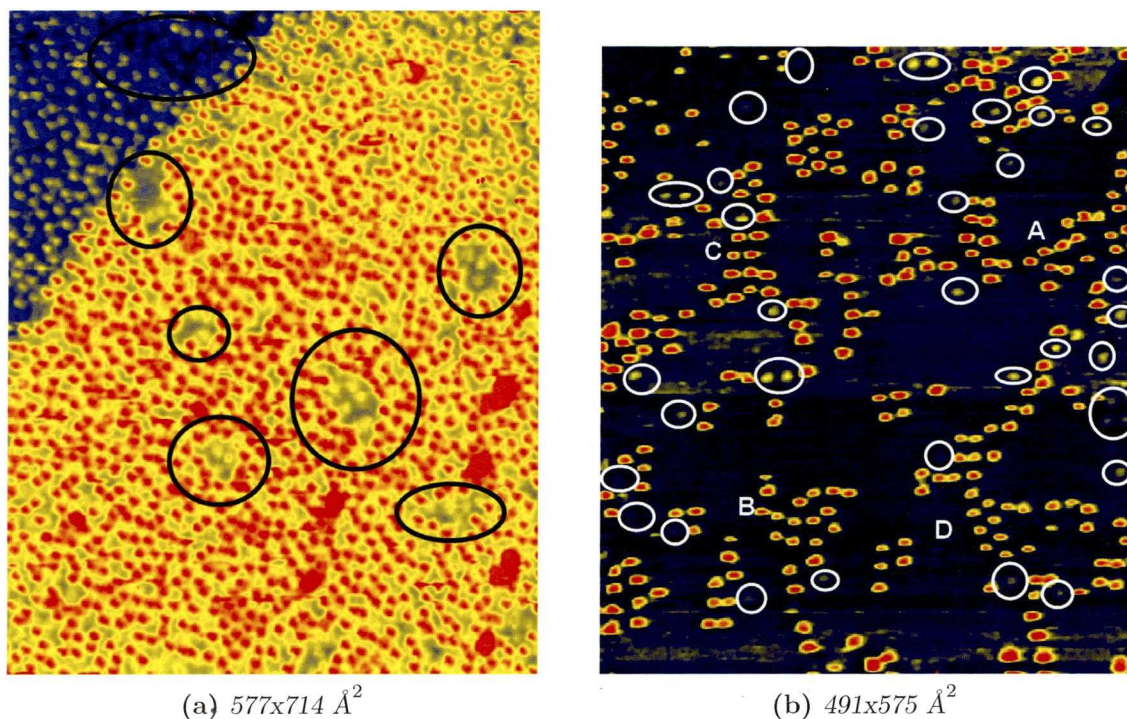


**Figure 6.1.** – a) High coverage  $V=1355$  mV,  $I=0.170$  nA b) low coverage image with TM-Co-TPP domains  $V=650$  mV,  $I=200$  nA.

Deposition of a low to medium coverage ( $\approx 0.35$  ML) also reveals two types of molecules that characterise the substrate (Figure 6.1b). The first type constitute bright protruded domains. The second type (white circles) are less protruded molecules that are significantly fewer in number i.e.  $\approx 15\%$  of the total number of molecules. These are the molecules that can be found in the dark patches of the high coverage phase. No self assembly is observed. The molecules that are in the majority create small domains (e.g. A-D) that vary in direction and size. Only a few individual protruded molecules can be found on the substrate.

Figure 6.2 are STM images in which one type of domain (A) is visualised. Both unprotruded and bright protruded molecules occupy the substrate. It now becomes apparent, at these bias settings, that dim molecules consist of two lobes. These are parallel to one of the main copper axes (001) and are attributed to the opposite pyrrole groups. The other main copper axis runs parallel to the depression that intersects the molecule. All are properties of a saddled shape. Furthermore, although faint, four mesityl groups can be distinguished, that as a result of the conformational changes of the core are rotated. The molecular arrangement of the domain is such that the domain itself is chiral with respect to the Cu(110) bulk. It is rotated by  $13^\circ \pm 1$  with respect to



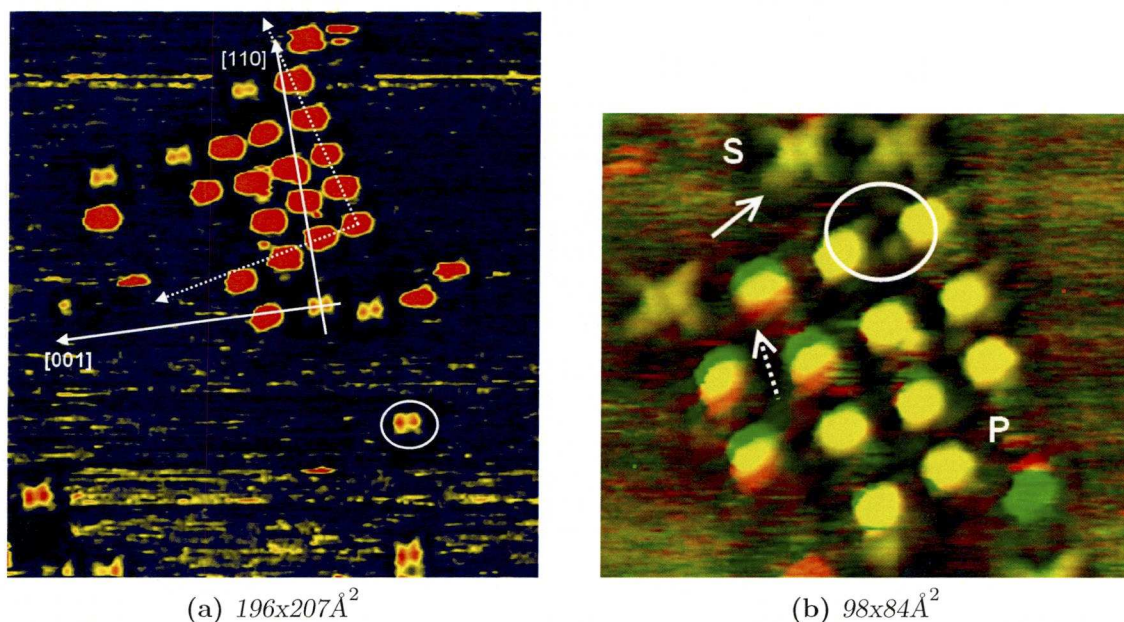


**Figure 6.2.** – a) TM-Co-TPP on Cu(110)  $V=-526$  mV  $I=-0.220$  nA b) TM-Co-TPP on Cu(110) image overlay indicating conformational changes and diffusion (green), ( $dt \approx 60$  s,  $V=-262.8$  mV,  $I=-0.220$  nA).

the [110] direction. Further explanation for this substrate directed rotation will be given in Section 6.3.

The mobility of several protruded molecules, which are not part of the domain, can be noticed by the LDOS elliptical shape Figure 6.2a. The LDOS of TM-Co-TPP molecules that do not diffuse appear circular. Some of the molecules in the domain possess small protrusions attached to the main lobe. These are related to the mesityl groups, visualised in Figure 6.2b, an image overlay of two subsequent STM images separated by sixty seconds. A saddled (S) molecule and planar (P) TM-Co-TPP molecule are indicated that are similar in size. The diametric mesityl groups are  $\approx 16.75 \text{ \AA}$  apart, which indicates that in spite of conformational change core rotation and significant size differences are not observed. The white arrow designates a rotated mesityl group of a saddled porphyrin. The circle denotes different imaging of three at different angles rotated mesityl groups. It is, therefore, concluded that the broader a mesitylic LDOS-profile the higher the degree of rotation and deviation from perpendicularity to the substrate. The mesityl groups rotation are the driving force for domain formation. It is however known from the TM-TPP molecule that the methyl groups generate strong interaction with the substrate.

A time-resolved sequence of STM data (Figure 6.3) amplify the dynamic substrate. It depicts another chiral domain rotated  $-13^\circ \pm 1$  with respect to the close packed copper



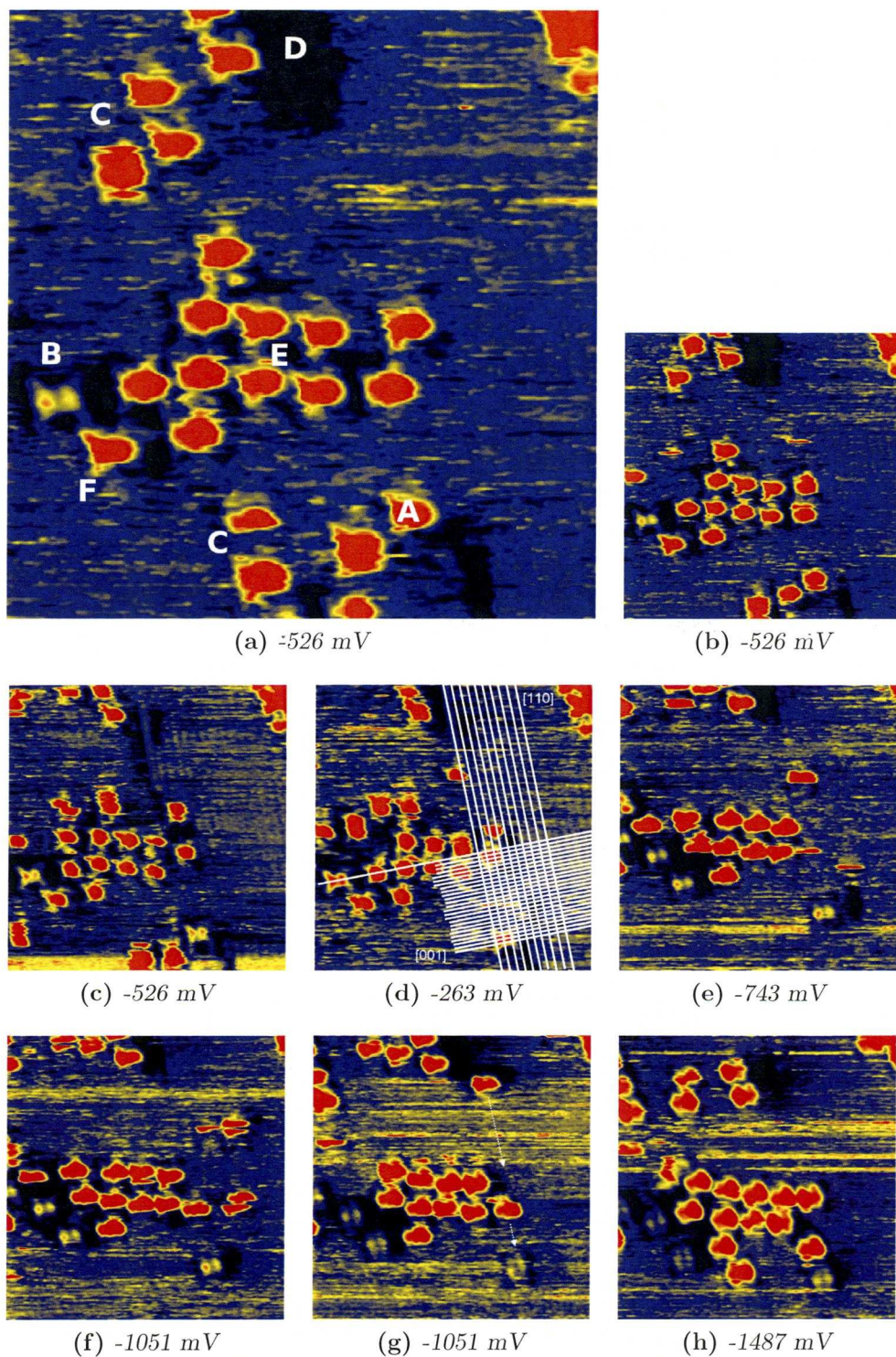


**Figure 6.3.** – Time resolved STM experiments,  $150 \times 150 \text{ \AA}^2$ ,  $I \approx -0.200$ ,  $dt \approx 480 \text{ s}$ .

rows. Designated are a planar (A), saddled (B) and a mobile planar (C) molecule. It has to be noted that a change in bias settings starting from image e, gave a LDOS profile that can be compared to that of molecule C. Therefore distinction between mobile



and immobile molecules is less straightforward and must be carried out by comparing subsequent images. Furthermore patch (D) is shown, which is an exposed second layer due to a locally disordered surface. In other areas of the image similar patches are present. The appearance of patch D changes in time and is occupied by copper chains (image c), that re-assemble top copper rows. A grid in image d represents the bulk (not the surface) copper structure derived from the molecular orientation and the partial atomic resolution achieved.

Two initially planar molecules (A and F, Figure 6.3) changed conformation to saddled (image b,c and d,e). The conformational change is substrate induced. It has to be noted, however, that it is possible to induce conformational changes in cobalt-porphyrins by voltage pulses.<sup>[232]</sup> The height of the voltage pulses ( $\approx 2-3V$ ) exclude a similar mechanism for TM-Co-TPP. The final images (f),(g) and (h) present further changes not only of patch D, but also around molecule A, that seems to be incorporated in the first substrate layer (image f-g) until one of the molecules diffuses from patch D to domain E and a molecule is repelled from the domain towards A (image g-h).

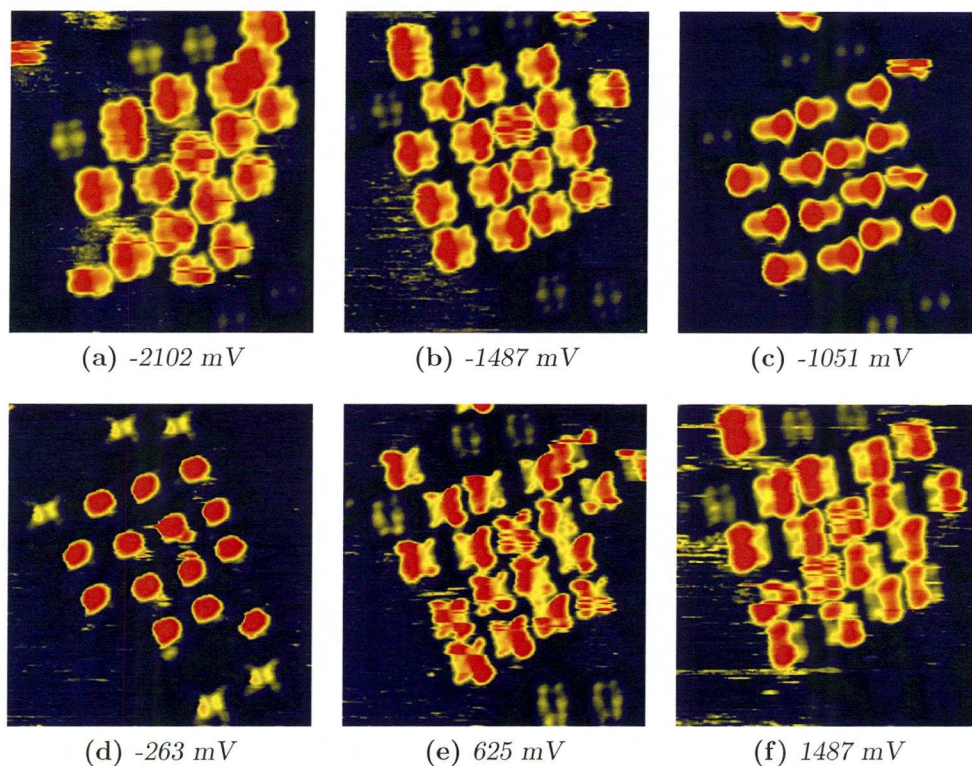


**Figure 6.4.** – Occupied and unoccupied states, image size  $99 \times 105 \text{ \AA}^2$ ,  $I \approx -0.220$ .



A chiral domain probed at different bias' conditions is shown in Figure 6.4. Altering the standard conditions (image d) to lower or higher voltages not only induces changes in the LDOS, but also molecular re-ordering. The domain in image(a) possesses different interactions and a domain angle shift compared to the images acquired at the other bias settings. The main difference between image a,b and c is the lack of electron density on the mesityl group in image c. If the frontier orbitals are examined (Appendix F) it is visible that for the MOs directly below the SOMO no mesityl contribution can be found. Only at more negative energies mesityl contribution occurs cf. image (a,c). The calculated orbital profiles are considered to be indicative for those of the molecule on the substrate, although the orbital profile can undergo changes, leading to substantially lower energies for the electronic states,<sup>[233]</sup> which may lead to combinations of orbitals that are close in energy.

It is known that around the Fermi level transition metals have a high density of d-states. For bcc metals these states are localised and mostly of  $d_{z^2}$  origin. Delocalised states are found for fcc metals due to the higher number of nearest neighbours. Hence the LDOS is a broad single peak.<sup>[234]</sup> Adatom chains, however, reveal above-chain localisation. DFT calculations suggest an along-chain linking of atomic orbitals that have a significant amount of  $p_z$  character.<sup>[235]</sup> Isolated adatoms present on a Cu(111) surface possess localised surface states that are of  $d_{z^2}$  and  $sp_z$  orbitals.<sup>[236]</sup> On Au(111) atoms have only s-wave states near the Fermi level.<sup>[122]</sup> In addition to this it has been shown by Buchner *et al.*<sup>[237]</sup> that the Cobalt  $d_{z^2}$  orbital of CoTPP has constructive overlap with the silver 5s band. Other STM studies have investigated cobalt-porphyrins and proposed that the electronic states of the protruding  $d_{z^2}$  orbital are less pronounced for CoTPP than for CoPc if the orbital lies physically further from the Au surface.<sup>[55]</sup> From DFT calculations<sup>[48]</sup> it is concluded that upon adsorption of CoTPP on Cu(110) the SOMO (Appendix F)  $d_{z^2}$  MO becomes fully occupied and therefore enhanced tunneling leading to the bright protrusions is not possible, suggesting that the cobalt atom participates in the delocalised surface states. It is also revealed that absorption preferentially occurs at a short bridge site. The Co porphyrinic macrocycle-Cu distance is calculated 2.1 Å. It is expected that for TM-Co-TPP the Cu-Co distance is significantly larger, which limits the possibility of a filled SOMO and hence an enhanced tunneling pathway exists for short bridge site and a top configurations. However the bright protrusion associated with  $d_{z^2}$  and surface state hybridisation almost completely dominates the topographical profile for an individual TM-Co-TPP molecule. It is therefore expected that, due to ad-island formation the surface states are more localised and not of s character but mainly

$d_{z^2}$  or  $p_z$  origin that protrude further from the substrate than s-wave functions, which results in stronger coupling to the substrate.

Also concluded from the orbital configuration at increased negative bias', for which the bright circular protrusion associated with the cobalt  $d_{z^2}$  orbital disappears and is replaced by an ellipsoid. It can be extracted from (Appendix F) that two degenerate orbitals exist at energy levels which are  $\approx -0.5\text{eV}$  away from the HOMO/SOMO. These consist of pyrrole contributions and the cobalt  $d_{z^2}$  orbital is replaced by  $d_{xz}$  and  $d_{yz}$  orbitals. It is, therefore, proposed that upon substrate contact a non-degenerate orbital exist for which coupling of the [001] aligned pyrrole groups occurs. Interestingly asymmetric core brightening occurs at both positive (e,f) and negative (a-c) bias conditions for the planar, more mobile molecule. Both orbital configurations appear equally on the substrate. Moreover switching occurs while scanning the next frame at similar bias conditions. Not all the molecules show changes in the density of states. The switching occurs in groups of molecules that are directly interacting with or at the edge of the domain. It is, therefore, proposed that the asymmetric core brightening is caused by the substrate rows in combination with pyrrole or mesityl groups.

The absorption site for the saddled configuration is different. The cobalt  $d_{z^2}$  bright protrusion is invisible. Instead two protruded areas related to tilted upward pyrrole units appear. This implies that either the cobalt centre is elevated from the substrate so that no wavefunction overlap can occur or the Co-Cu distance is decreased so that the single occupied SOMO becomes occupied by participation in the delocalised surface states. The saddled configuration can only be achieved via mesityl rotation and the subsequent downshift of the core. Therefore it is expected that adsorption takes place at the four fold hollow site.

The switching is induced by diffusion of molecules that are not part of the domain (Figure 6.5.) At the bias conditions for image (a) the central protrusions start to be observed as asymmetric shapes. Molecule (D) is indicated as is a copper substrate spot (E). The next image shows diffusion of D and simultaneous switching of the complete bottom row. Moreover molecules above E move also. This, however, does not introduce changes to the domain. The saddled molecule close to E blocks diffusion i.e. initiation of switching from that side of the assembly is suspended. The next image(c) shows subsequent protrusion change in the same area, while molecule D diffuses further away. The switching of the molecule in the top right part of the domain is also due to small displacement (cf. image b with c).



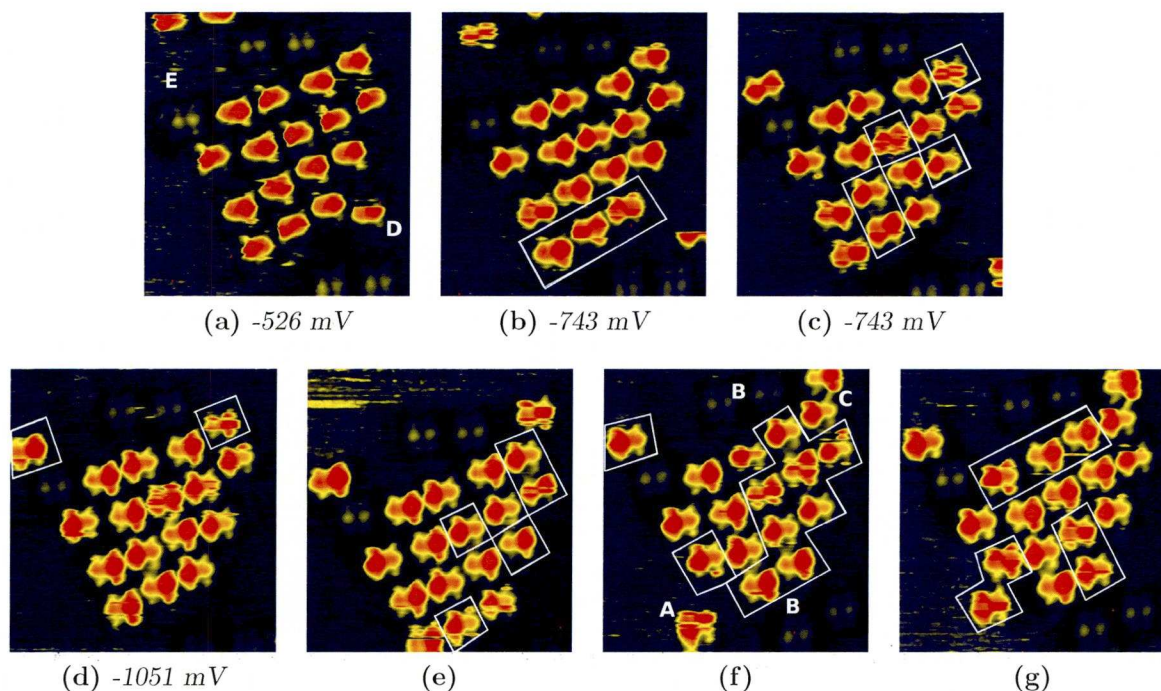


**Figure 6.5.** – STM images ( $99 \times 105 \text{ \AA}^2$ ) showing local symmetry change,  $dt \approx 45\text{-}45\text{-}90\text{-}480\text{-}90\text{-}45 \text{ s}$ ,  $I \approx -220 \text{ nA}$ .

A relatively stable situation is found for image d. The formerly mentioned molecule translates in the  $[110]$  direction away from the domain. Molecule C (image f) not visible in image (d) appears in image (e), inducing switching of molecules in proximity. Molecule A leaves the assembly, possibly as a result of the approach of C. This porphyrin binds to the assembly via  $\pi$ - $\pi$  stacking between phenyl groups. Finally the saddled molecules B (image g) also show limited diffusion towards the domain causing local switching. Molecule A returned.

The existence of the domains is determined by  $\pi$ - $\pi$  interactions. Figure 6.6 emphasizes the importance of these interactions. The images, that are sixty seconds apart and that precede Figure 6.5a, show two different situations. The arrow that points at an interaction ( $\alpha$ ) at the end of row A. And another arrow at the end of row B that indicates the start of a  $\pi$ - $\pi$  interaction ( $\beta$ ). In contrast to the first interaction which does not create significant conformational changes in row A induced by movement of a peripheral molecule, a conformational change in row B is observed. The local symmetry changes and a switch of molecular chirality ( $f$ ) is observed via the rotation of mesityl groups. The global chirality of the domain is maintained.



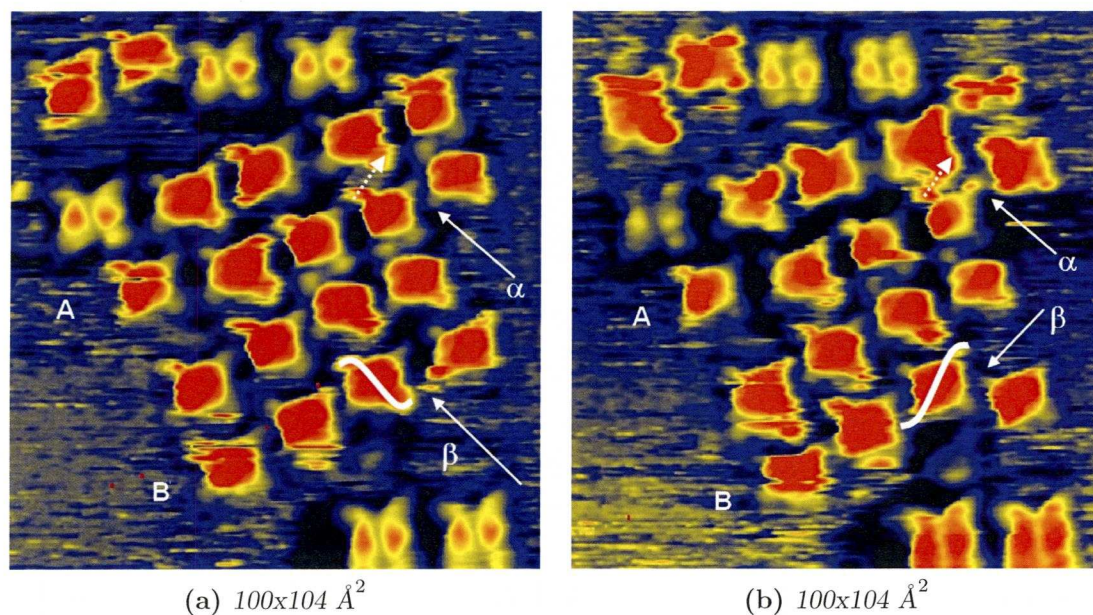


**Figure 6.6.** – *Change of molecular chirality by mesityl group interaction,  $V=262.8$  mV,  $I=220$  nA.*

## 6.2. RAIRS

Figure 6.7 show spectra of TM-Co-TPP deposition monitored by RAIRS. Not only the higher symmetry of the molecule but also the planarity results in a fewer number of vibrations visible in the spectrum, especially many skeletal modes do not appear. To maintain clarity the same letters proposed in the previous chapters are used. It has to be noted that baseline correction for the wavenumber region  $650\text{--}750\text{ cm}^{-1}$  is subjected to variations and hence conclusions from this part (A to C\*) of the spectrum cannot be drawn.

However, the RAIRS results show a spectrum that does not change upon increased coverage and that is very similar to the metastable TM-TPP results (Figure 4.2). Moreover the STM-results confirm that most of the TM-Co-TPP molecules exhibit mesityl groups that are not deviated significantly from perpendicularity to the substrate. Therefore assignment of vibrational modes is similar and further detail can be found in Chapter 4. A very weak absorption band exists around  $1550\text{ cm}^{-1}$  (spectrum 3 to 5). The presence of this (oop ph) mode is attributed to the existence of a small number of saddled molecules at the substrate.

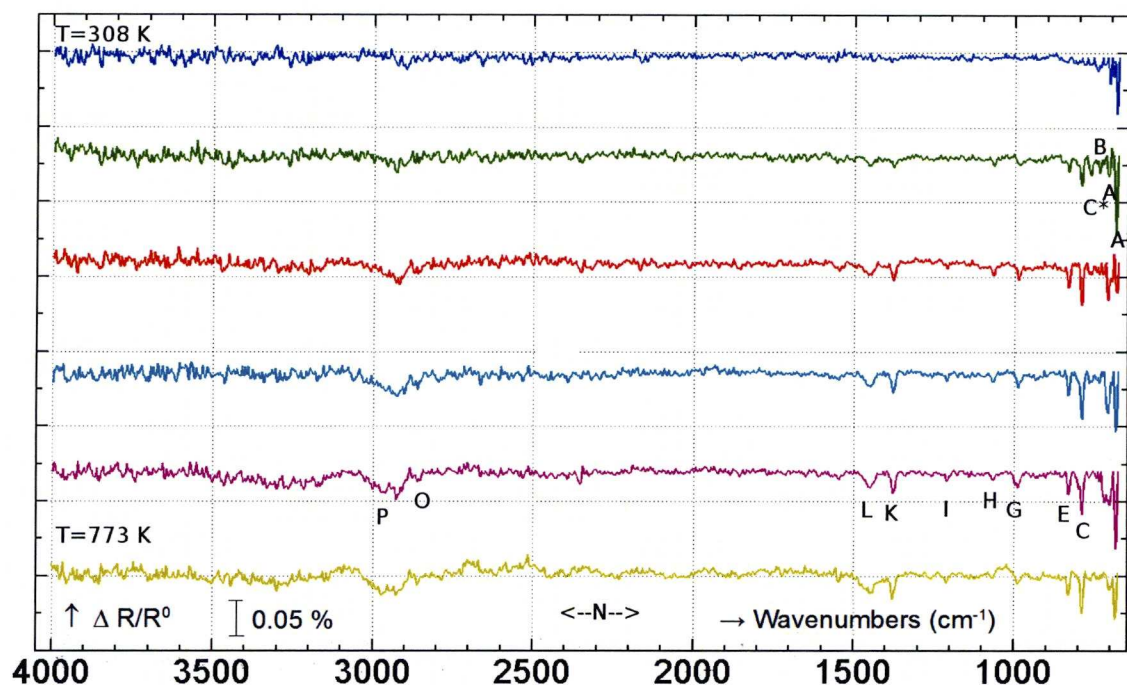


**Figure 6.7.** – RAIRS spectra of TM-Co-TM-TPP acquired at different temperatures during a time interval of  $\approx 900$  s for the first four graphs increasing the coverage at RT after which the substrate was heated for respectively  $\approx 300$  and  $\approx 1200$  s

Main conclusions from the above RAIRS data are that in contrast to TM-TPP no metastable phase exists for TM-Co-TM-TPP. It is however possible to consider the planar conformation metastable for it changes to a saddled configuration. This confirms the planar metastable phase of TM-TPP, which due to its free-base configuration lacks metal-metal interactions and hence has a significantly shorter metastable period at RT conditions.

A gradual anneal of the substrate during 15 minutes to 773 K did not give modifications in the spectrum, therefore no conformational changes occurred for these timescales and temperatures.

### 6.3. Model of TM-Co-TPP on Cu(110)

It can be concluded from the previous sections that, similar to the interaction of TM-TPP with the Cu(110) substrate, TM-Co-TPP deposited at RT also interact strongly with the substrate, hence disordered substrate areas exist. This limits the accuracy of the models presented in Figure 6.8. Moreover all mesityl groups presented in the



model are perpendicular to the substrate, which is also a simplification. It is, however, sufficient to create an understanding of the variety of events both intermolecularly and interatomic. The model is based on Figure 6.2b.

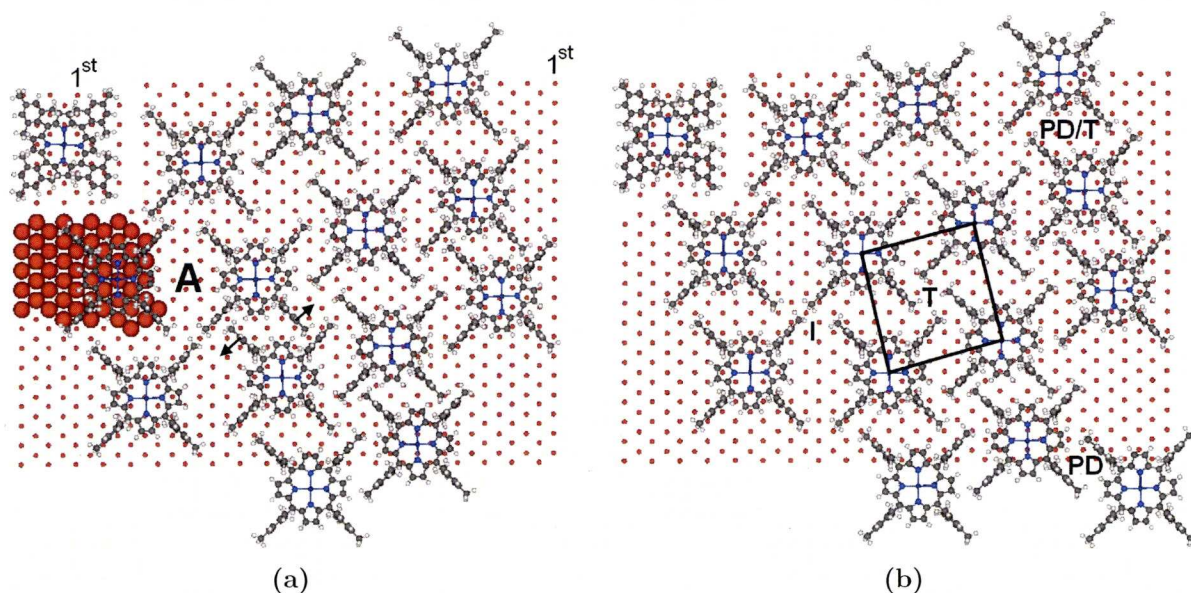


**Figure 6.8.** – **a)** Model of Figure 6.2b, **b)** Model after diffusion (Figure 6.2b, dashed arrow)

Based on the calculations different attractive  $\pi$ - $\pi$  interactions between phenyl groups are proposed. Parallel displaced (PD), T interactions and a combination of both.<sup>[48]</sup> I-interactions are mesityl groups of different TM-Co-TPP molecules that are situated exactly in line and not rotated, hence perpendicular to the substrate. The small black arrows indicate the expected direction of rotation with respect to the porphyrinic core as a result of minimised intermolecular distances. Four molecules, that surround A, show a concerted movement of 2.55 Å along  $\langle 110 \rangle$ . This is exactly one lattice space. The molecule at the core of the domain form a unit cell for which the rotation from the close packed copper rows is 13.3°.

Furthermore a saddled molecule occupies the top left corner of the domain. Significantly smaller diffusion magnitudes are observed for the saddled configuration. If the copper corrugation under the molecules was regular this molecule would adsorb on a top copper row. However, core debrightening suggest adsorption at the 4-fold hollow site. This is induced when the top copper layer relocates upon conformational change from planar to saddled and adsorption at the second layer becomes possible.

Finally it can be concluded that, based on core to core distances derived from the STM images planar molecules adsorb either Atop or short-bridged. A preference is given



to Atop adsorption based on frequently observed pyrrole-substrate coupling (spacefilled region image a). This assumption is valid if the copper arrangement under planar TM-Co-TPP molecules follows the bulk corrugation. Due to the dynamic nature of the domain and the inherent mesitylic rotations it is assumed that copper rearrangement only takes place at the periphery leaving the Co-Cu interaction intact.

The variety of interactions possible, the mobility of individual molecules not restricted by main copper axes and the influence of the substrate, limit formation of large assemblies.

## Chapter 7.

# Thermal activation of TM-Co-TPP on Cu(110)

RT deposition of TM-Co-TPP molecules at Cu(110) results in small domains of flat molecules and a limited amount of saddled unassembled molecules at the surface. This chapter describes STM results obtained after extended moderate and maximized post-anneals.<sup>1</sup>

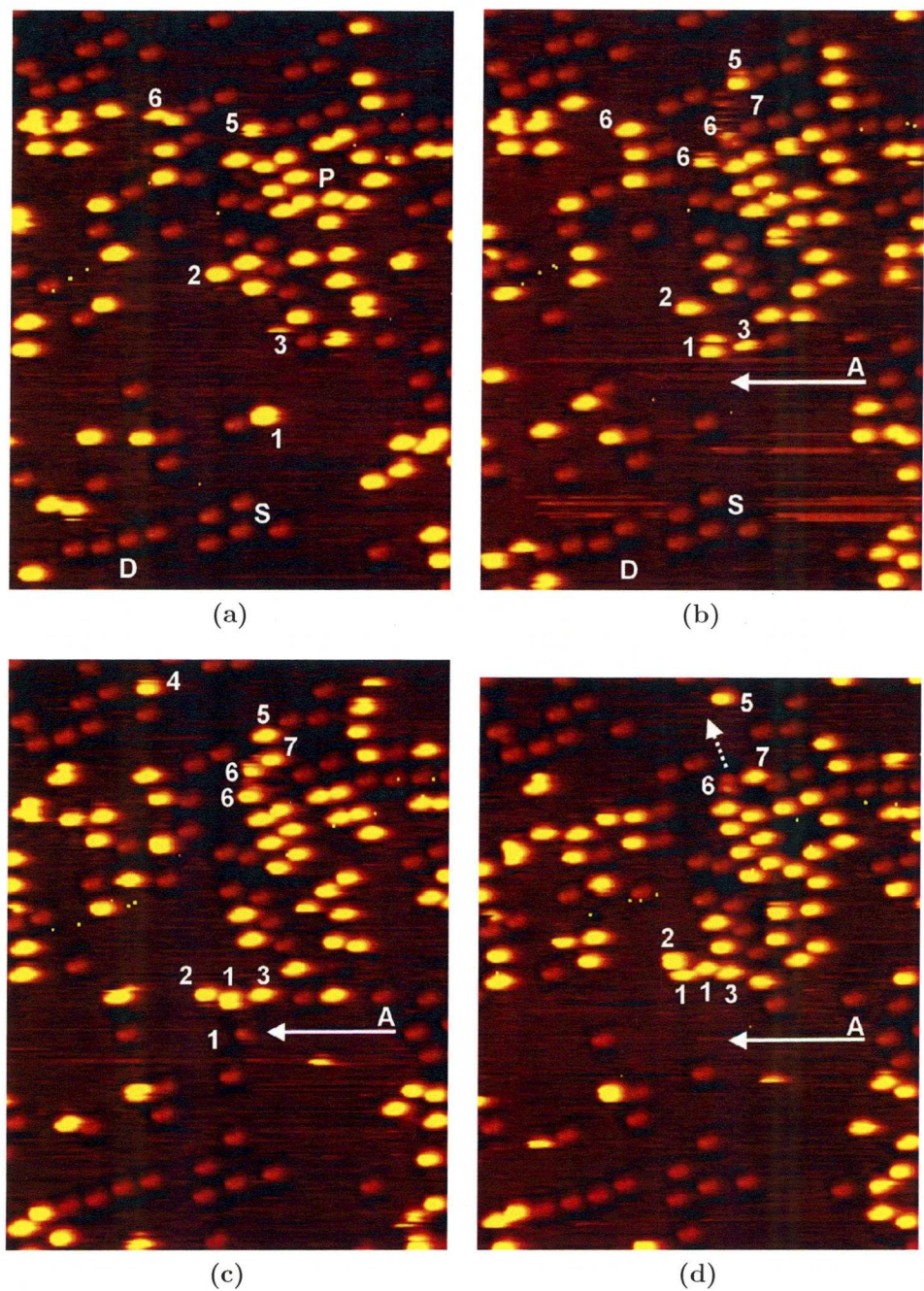
### 7.1. Intermediate activation: STM

Figure 7.1 and Figure 7.2 present a sequence of seven images acquired after heating the substrate ( $\approx 0.4$  ML) to 373 K for 30 minutes. The molecules P (bright) and S,D (dim) are respectively planar and saddled molecules. The addition of thermal energy changes the percentage of planar conformations from  $85\pm 5\%$  (RT) to  $50\pm 5\%$ , a confirmation of a temperature dependent metastable configuration. Many changes can be noticed as a function of time, therefore the discussion of these images is split.

In Figure 7.1a the molecules numbered 1,2,3,5 and 6 are bright planar TM-Co-TPP molecules. This confirms the presence of a cobalt atom in the core similar to the RT-phase. D marks four saddled molecules that due to their adsorption site are equally separated in the [001] direction. Also on other regions of the substrate saddled molecule alignment exist. Self-organisation in the direction of the close-packed copper rows is

---

<sup>1</sup> Unless otherwise stated all STM images and RAIRS Spectra presented are acquired at constant current (STM),  $T = 298$  K and a base pressure of  $\approx 5.0 \times 10^{-10}$  mbar and  $\approx 2.0 \times 10^{-9}$  mbar while dosing the molecules. Doser settings can be found in Section 3.6.1. Colourcodes on page 1.



**Figure 7.1.** – *TM-Co-TM-TPP* on *Cu(110)* after heating at  $\approx 373$  K for 30 minutes  $281 \times 312 \text{ \AA}^2$ ,  $I \approx -0.200$ ,  $V = -1250 \text{ mV}$   $dt \approx 67 \text{ s}$  (the small yellow dots in the STM images are noise).

not observed. When examining the next image (Figure 7.1b) it becomes apparent that planar molecules possess significantly higher anisotropic diffusion magnitudes in contrast to the dim counterparts (S,D). This is due to the difference in conformation and adsorption site (see also Section 7.3). The saddled molecules are restricted to relatively

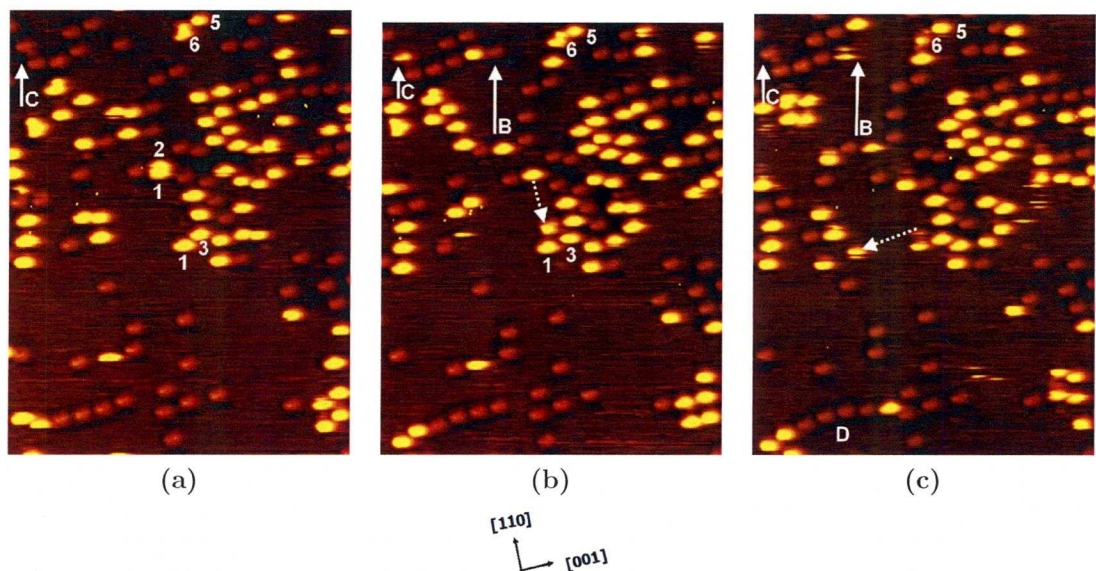


limited translations of a few lattice spaces along the “diffusion lanes” in the close packed direction (cf. D Figure 7.1a and b).

Interestingly translation of molecule 1 towards molecule 3, that is now imaged completely (Figure 7.1b), reveals the presence of possibly two bright molecules in proximity either for molecule 3 or molecule 1 (the mobility can result in differences in imaging, 3 image(a)). Figure 7.1c and Figure 7.1d confirm this. Arrow A points at a substrate spot where suddenly a dim molecule appears, whereas the bright molecules 1,2 and 3 can still be found in proximity. Molecule 4 will be of relevance later during the discussion of the next series of images. A frame later (image (d)) the dim molecule reconfigured to a bright molecule and four molecules exist in the region above the end cap of arrow A.

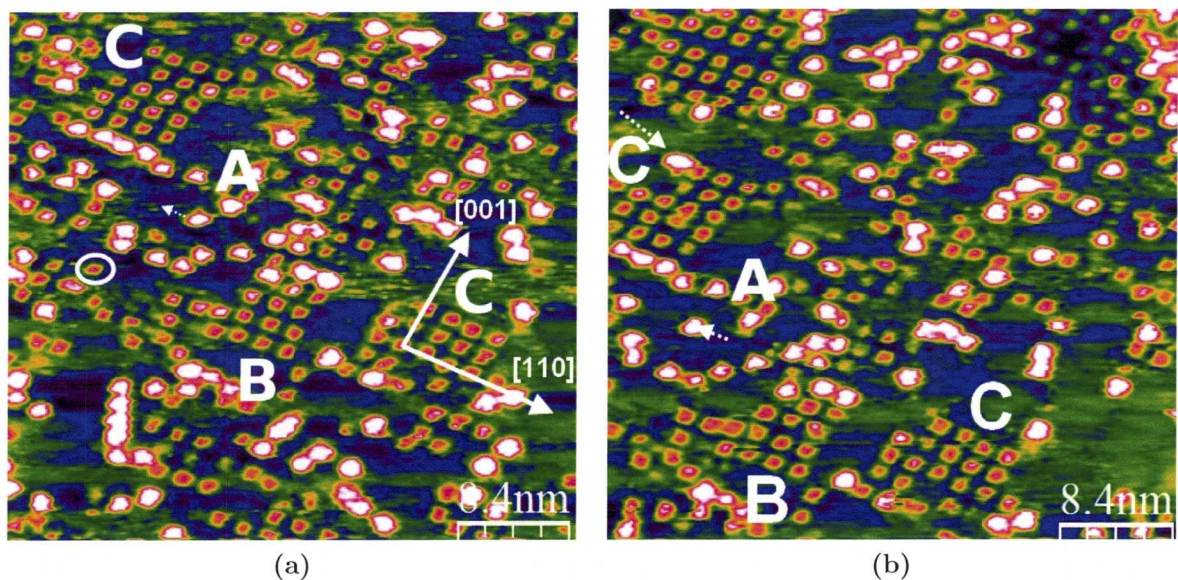
A similar situation can be noticed for molecule 6. In image (a) there are two bright protrusions next to each other. A frame (b) later, after diffusion of molecule 5, three blobs can originate from the molecules 6 in (a). First the bright protrusion that remains localised and two of the molecules indicated by 6 in image (b), one of which relocated from 6 in image (a). A preference is given to the molecule next to 7, which is in a transition state between dim and bright. Again a frame (c) later transformation of molecule 7 is observed, while simultaneously the neighbouring molecule 6 also increases its brightness, suggesting a different preceding conformation. In addition to this another diffusion step of molecule 5 can be noticed from image (c) to image (d), meanwhile the previously transformed molecule 6 reverts to a dim molecule that appears slightly rotated. The dotted arrow in Figure 7.1d indicates subsequent movement of 6 towards 5 as is visualised in the next Figure 7.2.

Figure 7.2a confirms the presence of 6 next to 5, and again a transition from dim to bright occurred. Furthermore one of the molecules 1 and molecule 2 diffused simultaneously and image as a single bright protrusion. A frame later (Figure 7.2b) a molecule has returned towards 1 and 3 (dotted arrow) and continues to move (dotted arrows, Figure 7.2c). The other bright protrusion remains relatively localised. The arrows B and C denote two other different occurrences of molecular transformation. B indicates a dim saddled molecule that changes to the bright blob above B in Figure 7.2c. This is not molecule 4 that diffused away in another direction earlier (Figure 7.1c,d). Molecule C experiences a dim-bright-dim or saddled-planar-saddled transformation. Figure 7.2c also shows that the alignment of saddled molecules (D) to the substrate rows can be disturbed by interaction of a diffusing planar molecule. Moreover interaction of 6 with 5 and another molecule makes the core brightening of 6 less intense, suggesting different interaction with the substrate. From the multiple existence of molecular transformations



**Figure 7.2.** – Figure 7.1 continued,  $281 \times 312 \text{ \AA}^2$ ,  $I \approx -0.200$ ,  $V = -1250 \text{ mV}$ ,  $dt \approx 67 \text{ s}$ .

it is concluded that Co is present in the porphyrinic core for both the bright and dim conformation. Modifications in the substrate, mesityl rotation, mesityl-mesityl ( $\pi$ - $\pi$ ) interaction and conformational changes determine diffusion.



**Figure 7.3.** – TM-Co-TM-TPP on Cu(110) after a gradual anneal to  $T \approx 393 \text{ K}$  for  $\approx 60$  minutes. Experiments were carried out on an Omicron Variable Temperature SPM. Data analysis was performed by the use of WSxM 4.0 Develop 12.0<sup>[238]</sup>,  $V = 1423 \text{ mV}$ ,  $I = 0.189 \text{ nA}$ ,  $dt \approx 300 \text{ s}$  (It has to be noted that the sample was subjected to baseline drift).



The saddled/planar ratio can be controlled by thermal energy. Figure 7.3 shows STM results obtained with a different instrument (Omicron VT-STM). The addition of thermal energy was regulated. Therefore a higher degree of control was achieved. Again both conformations are found on the copper surface covered by  $\approx 0.5$  ML. The white protrusions (A) are flat molecules. Saddled configurations are indicated by a circle. The ratio is approximately 1:1. In comparison to the RT results phase inversion occurs. Self-organised domains (B,C) now consist of saddled molecules, most of the planar molecules do not self-organise. Domains C are aligned according both main copper axes, while domain B is  $9\pm 1^\circ$  offset from the close packed copper rows and therefore chiral. The mobility of flat porphyrins is relatively low. Diffusion of a molecule can be found near A. The bright protrusion found at C (image b, dotted arrows) is a conformational reversion.

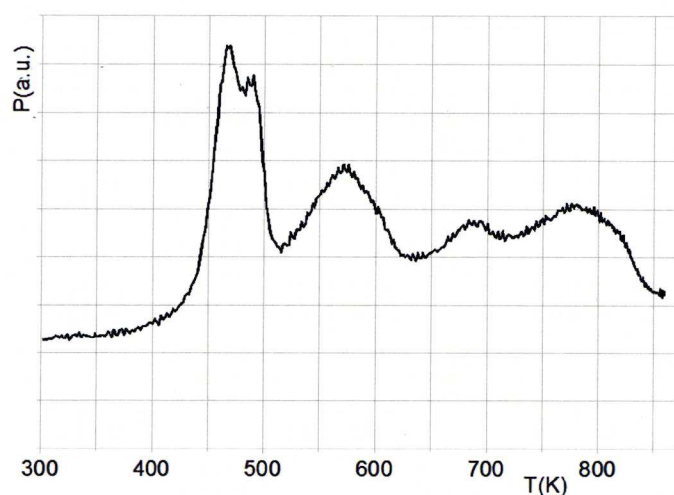


**Figure 7.4.** – TM-Co-TPP on Cu(110) TPD profile monitoring the evolution of hydrogen into the vacuum,  $dt \approx 400$ s.

Similar to TM-TPP an anneal generates hydrogen evolution (Figure 7.4). The plot shows two desorption maxima at  $\approx 460$  K and  $\approx 580$  K. These are related to different absorption sites and hence the desorption of the planar and saddled configuration of which the ratio is approximately 4:3. Due to decreased mobility and stronger substrate interaction, it is expected that the desorption peak at 490 K belongs to the saddled conformation. This maximum consists of two smaller peaks, probably due to intermolecular interactions described previously. In contrast to the desorption profile of TM-TPP no desorption tail is visible. This is ascribed to pre-metallation of the porphyrin. The desorption peaks  $> 550$  K are a result of either gas desorption from the sample holder or more stable decomposition products.



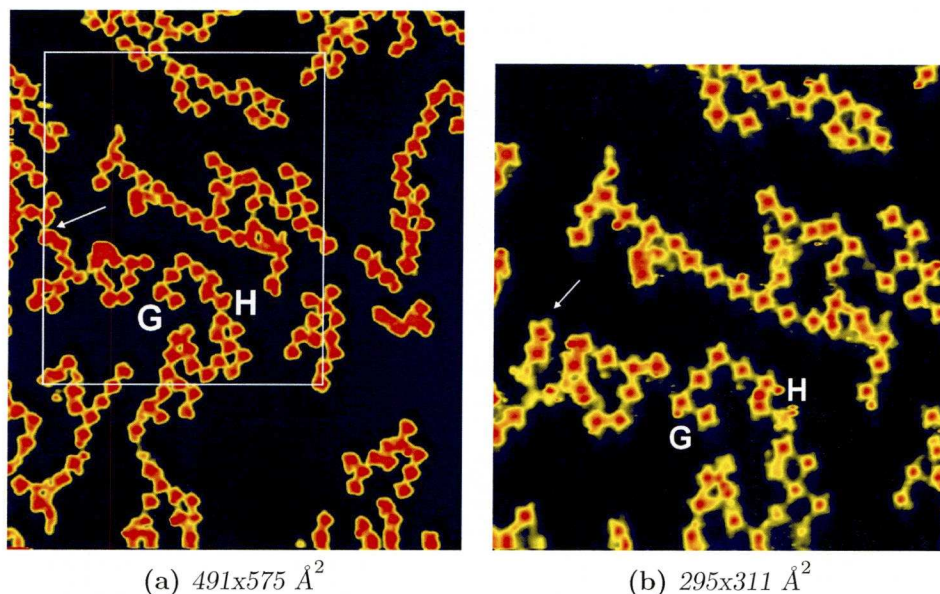


**Figure 7.5.** – TM-Co-TPP on Cu(110) after a maximised anneal,  $V_a = -930 \text{ mV}$ ,  $V_b = -1105 \text{ mV}$ ,  $I \approx 0.200 \text{ nA}$ , (Image b was acquired before a).

## 7.2. Maximised activation: STM

Heating a TM-Co-TPP covered Cu(110) substrate to  $\approx 470 \text{ K}$  for 30 minutes gives, similar to TM-TPP, a variety of flat covalent poly-molecular networks (Figure 7.5a). The rectangle marks the magnified area presented in Figure 7.5b. The arrow denotes a pair of molecules that rotate  $\approx 45^\circ$  anticlockwise, which is an indication of a flexible ethylene linkage similar to polymerised TM-TPP. The decreased activation barrier with respect to TM-TPP can be explained in terms of adsorption site.

Figure 7.6 presents an overview of the occupied and unoccupied states after applying a maximised anneal at  $\approx 470 \text{ K}$  for 30 minutes. Image a and b are a magnification of the central area of Figure 7.6b. The major difference between scanning at positive or negative voltages are the cobalt- $d_{z^2}$  and mesityl contribution. These do not contribute to the LDOS at positive bias' and therefore the LDOS appear squared, unless coupling of a mesityl group with the substrate exists (G,D). H designates a different type of interaction resulting in a bright protrusion between two mesityl groups, attributed to *para* methyl-substrate interaction.

The images c,e,f,...,i are part of a time-resolved sequence ( $dt \approx 50 \text{ s}$ ) and magnifications of the central molecule in image d. It has to be noted that the dynamic nature of the substrate influences the imaging conditions. A denotes a mesityl group that as a result

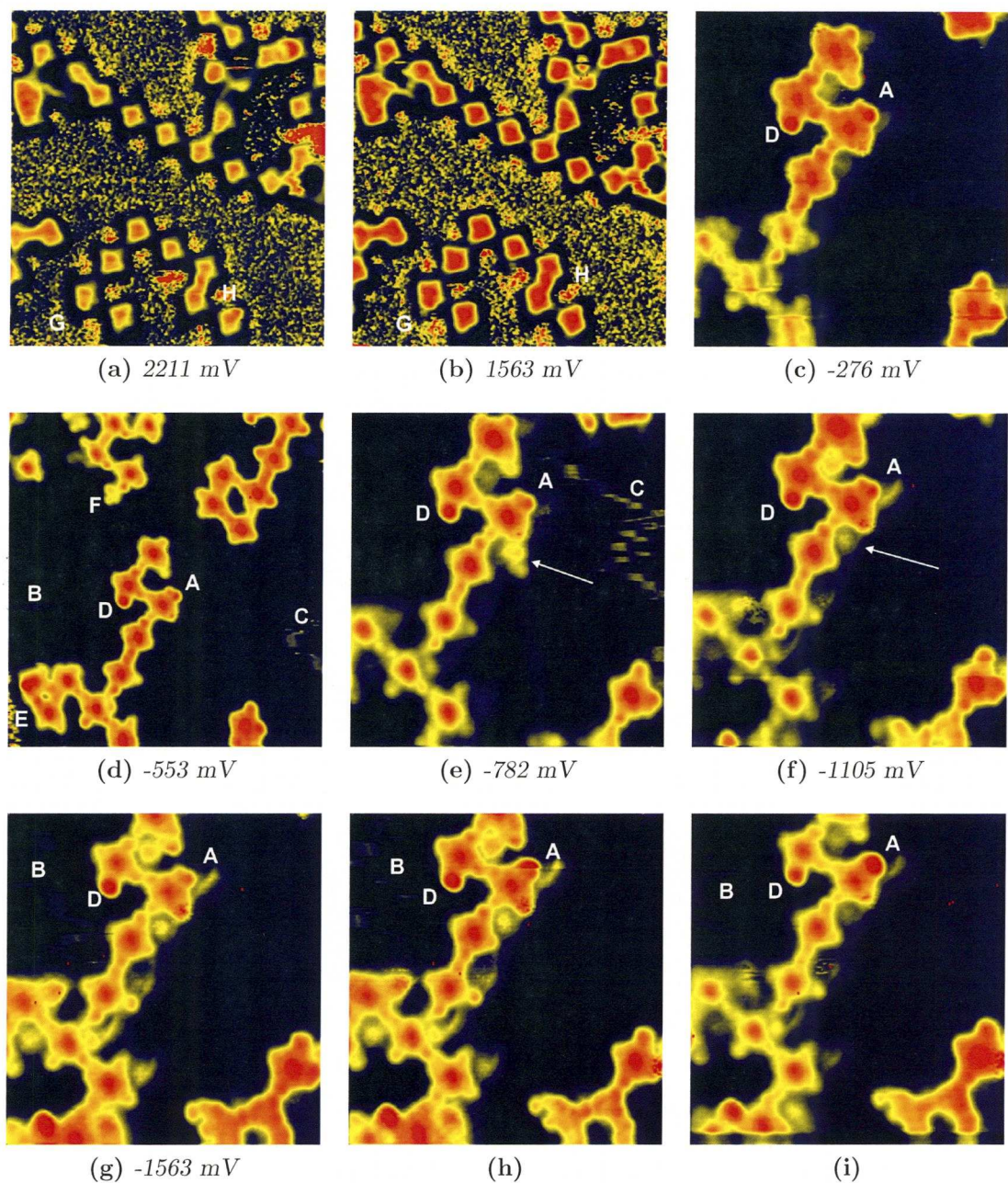


**Figure 7.6.** – *TM-Co-TPP networks, occupied and unoccupied states,  $98 \times 104 \text{ \AA}^2$ ,  $147 \times 156 \text{ \AA}^2$  (a,b,d)  $I=0.200 \text{ nA}$*

of substrate rearrangement (B,C) couples with the substrate (i). The arrow in image (e) indicates a copper cluster, that diffuses in the direction of the mesityl-group next to it. It can be concluded from image (f,g) and (h), that temporary electronic coupling to the substrate exist. This in contrast to TM-TPP, where molecule substrate coupling is



a common event. In spite of the fact that two extra possibilities exist coupling is rarely observed for TM-Co-TPP. Therefore a different adsorption site is expected.

E denote a group of three molecules of which one of the molecules exhibits two bright protrusions. This is thought to have reacted in an unconventional way possibly *ortho* mediated which limited the interaction of the other *ortho* group with a pyrrole group and therefore points into the vacuum. F is either a TM-Co-TPP fragment or another copper cluster.

### 7.3. Model of covalently linked TM-Co-TPP on Cu(110)

Figure 7.7a presents domain B of the saddled molecules observed in Figure 7.3. It has to be noted that the model is indicative. However, core-core distances closely resemble those of the real separation in the STM image. Therefore it is concluded that similar to saddled RT adsorption at the 4-fold hollow site is favoured. For a-chiral domain C (Figure 7.3) the molecules are aligned to both main copper directions. If a saddled molecule shifts a lattice space in the close packed direction domain B is obtained.

The model in Figure 7.7b shows a hexameric grid composed of TM-Co-TPP molecules. Two adsorption sites exist for the central cobalt atom. Short-bridged and Atop. The rotated ( $19.5^\circ$  with respect to the close packed copper rows) part of the grid (spacefilled region) is equivalent to the molecule in the network next to A in Figure 7.6. The other side of the grid resembles aligned molecules that cover the substrate similar to the molecule next to D in the same figure. Whereas for poly-TM-Cu-TPP the connections were situated above the trenches, for poly-TM-Co-TPP these are expected above the first substrate layers (A,B). The arrow denotes a bond between molecules that have a different adsorption site. Due to the dynamic nature of the substrate applicability of the model is limited.



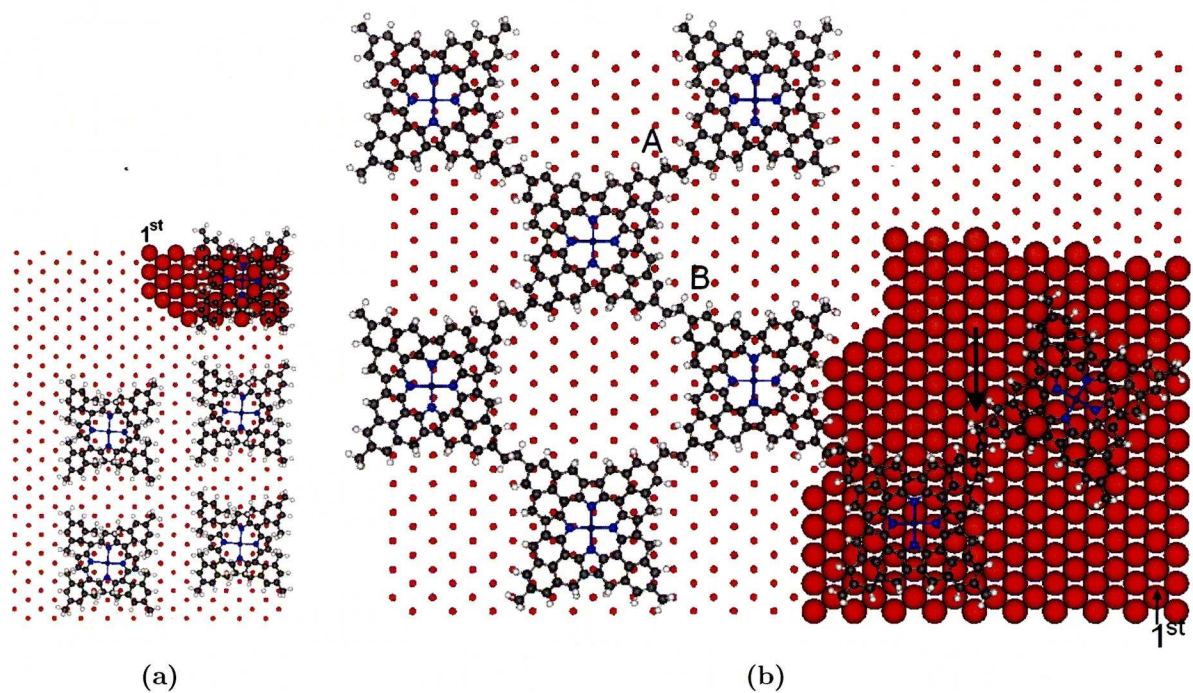


**Figure 7.7.** – Models of annealed TM-Co-TPP on Cu(110) *a)* Intermediate activation *b)* Maximised activation (The Cu main axes are similar as previously stated page 106)

## Chapter 8.

# Co-deposition of methyl- $\alpha$ -D-Glucopyranoside and TM-TPP

*“The amino acids found in meteorites do show some signatures that suggest an interstellar connection. This connection, combined with our finding that amino acids can be made in interstellar clouds suggests that the Earth may have been seeded with amino acids from space in its earliest days.”*

— Dr. Scott Sandford of Ames

If everything happens at once time would not exist, according to Albert Einstein. His quote was the start of this thesis. If everything happened at once the Earth and life would not exist. Fortunately nothing happens at once. From chemical reactions that occur at femtosecond timescales, to Earth's rotation around the sun in  $\approx 365$  days, to the many galaxies that are lightyears apart and which give shape to the universe  $\approx 14$  billion years of age. The early Earth was formed  $\approx 5$  billion years ago and, as the above quote suggests, prebiotic molecules could have landed on earth i.e. via carbonaceous chondrites. Recently the Stardust program<sup>[239]</sup> confirmed the presence of the amino acid Glycine, a building block of proteins, in comet 81P/Wild 2 which orbits in our solar system.

It is proposed<sup>[240]</sup> that before DNA and proteins existed an RNA world was the foundation  $\approx 4$  billion years ago preceded by a glyco-world for ribose is the carbohydrate



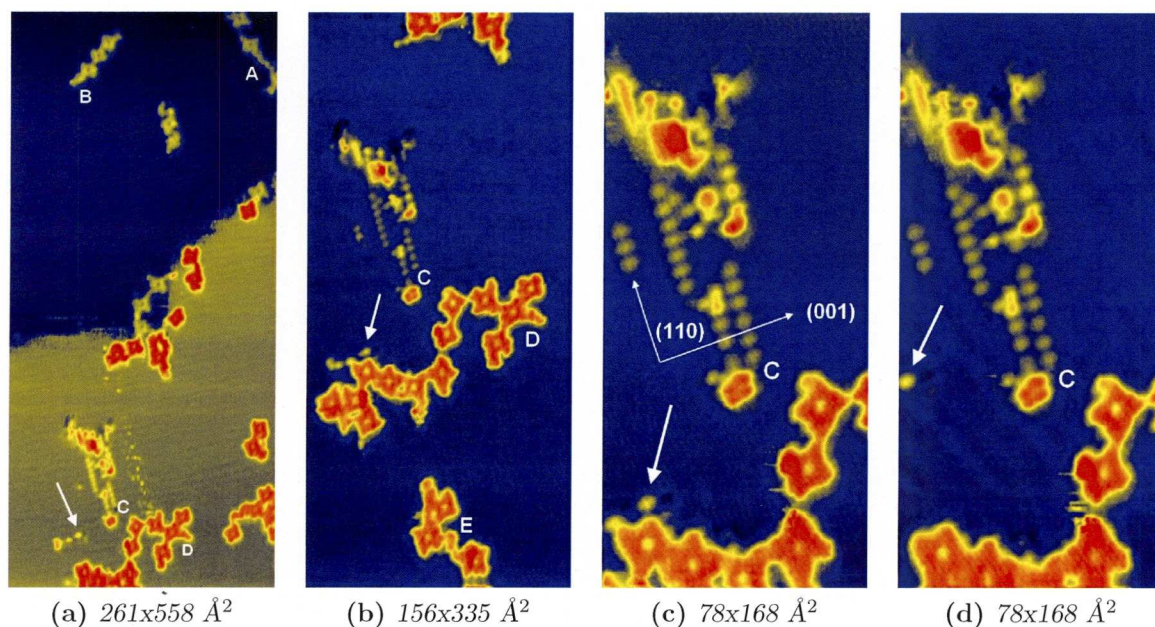


**Figure 8.2.** –  $I=0.200$  nA,  $V=267,0$  mV,  $dt_{ab} \approx 200$  s,  $dt_{bcd} \approx 60$  s (The substrate corrugational amplitudes visible in the images a,c and d is attributed to noise)

B and D in Figure 8.2 indicate extensions to the corners of porphyrin units that are part of (branched) networks. These supposedly sugar units do not diffuse at RT. It is therefore assumed that a covalent bond between the mesitylic *para* methyl and MDG is created. Connection at the the *para* group seems preferential. However, it cannot be excluded that *ortho* methyl groups participate in reactions. An example are molecules located near E (Figure 8.2)b. Sugar connection seems to have occurred via *ortho* mediation. Furthermore a different appearance of the TM-TPP networks with respect to deposition and annealing of homogenous TM-TPP can be noticed. No specific alignment is found in contrast to the high temperature phase of TM-TPP, where the porphyrin units of the polymeric networks align to the main copper axes. Therefore, it is concluded that by the connection of MDG to TM-TPP changes in the network orientation are introduced.

A special situation, connection of multiple sugar units (A), was found at the lower terrace of image Figure 8.2a. Porphyrinic molecules are connected to each-other via a strand of four to five MDG molecules, that are presumably covalently bonded. Observation of such chains suggests not only methyl mediated bonds, but also methyl-oxygen interactions. Support for sugar-sugar bonding is found in the group of four protrusions below C, which are probably four MDG molecules, that have reacted to form a polysaccharide.



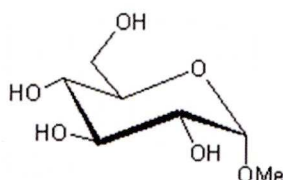


Figure 8.1. – methyl- $\alpha$ -D-glucopyranoside

used by RNA. The existence of life depends on a way to transfer catalytic information (RNA) and although synthesis of small prebiotic molecules has been proven, a higher level of self-organisation in oligomers and subsequent self-replication was required.<sup>[6]</sup> Carbohydrates are not only important in DNA, but also serve as energy storage ( $\alpha$ -linked-poly-sacharides), and are the building blocks for poly- $\beta$ -1,4-D-glucose (cellulose) in plants.

The former chapters show that it is possible to create a distribution of sizes and shapes of oligomeric molecules for both free-base TM-TPP and TM-Cobalt-TPP. Furthermore, the alignment of the central pyrrole ring along the high-symmetry axes of the Cu(110) surface means the connections mediated via the *para*-methyl groups occur along non-symmetry directions. This methyl group is essential for the polymerisation reaction. Therefore co-deposition of methyl- $\alpha$ -D-glucopyranoside (MDG), an acetal of D-glucose (Figure 8.1), and TM-TPP was studied.<sup>1</sup>

Figure 8.2 presents a sequence of STM-images after annealing the substrate with a low coverage of both sugar and TM-TPP molecules to  $\approx 473\text{K}$ . The MDG molecules (C) self-assemble in small domains, which is similar to adsorption at RT. Therefore total decomposition does not occur. A specific example of this self-assembly can be noticed in the four images. In image (a) only one MDG molecule is adsorbed at the righthand side of the arrow that indicates another MDG molecule in proximity of a porphyrinic macrocycle. The next image (b), acquired 200 seconds later, a second MDG molecule moved towards it. Simultaneously two sugar-molecules (arrow) approach the nearby oligomeric network. Spot on the porphyrinic *para* methyl groups. In the following image (dt=60 seconds) the dimolecular assembly is extended to three. The molecules align along [110]. The molecules that interacted with the porphyrinic structure diffuse away within a minute (image (d) arrow). Substrate rearrangement (dark patches next to (C), the mobile sugar and above the assemblies) is also observed.

<sup>1</sup> Unless otherwise stated all STM images presented are acquired at constant current,  $T = 298\text{ K}$  and a base pressure of  $\approx 5.0 \times 10^{-10}\text{ mbar}$  and  $\approx 2.0 \times 10^{-9}\text{ mbar}$  while dosing the molecules. Doser settings can be found in Section 3.6.1. Colourcodes on page 1.

## Chapter 9.

### Conclusions

Temperature dependent (298 to 500 K) interaction of (free base) 2,4,6-trimethyl-5,10,15,20-tetraphenyl-(Co)-porphyrin (TM-(Co)-TPP) with a corrugated Cu(110) substrate in ultra high vacuum was the main focus of research presented in this thesis. Besides the heterogenic systems methyl- $\alpha$ -D-glucopyranoside/TM-TPP and tartaric acid/TM-TPP co-deposited on Cu(110) were investigated as function of similar substrate temperatures. The most important conclusion is valid for all:

*Addition of sufficient thermal energy results in the copper substrate catalysed creation of inter-molecular para methyl mediated covalent linkage and subsequent oligomers.*

Another observation for the porphyrins studied by STM and RAIRS is the introduction of intra-molecular bonds between *ortho* methyl and pyrrole groups. The total number of connections is dependent on the substrate temperature conditions, but also on the type of molecule. It turned out that for pre-metallated TM-Co-TPP all eight *ortho* methyl substituents can interact after which a new achiral molecule is formed. A different situation arose for the free-base version. That molecule only allows a maximum of six *ortho* methyl groups to intra-molecularly bind, which yields a new chiral molecule. This chirality is induced by the absorption of a Cu-atom in the porphyrinic core. Conformational changes that are not possible for the metallated porphyrin result in a sequential linkage. Only one handedness (trailing left-helical) is observed. This possibly originates from magnetic effects in combination with core deprotonation for which the nitrogen atoms are not identical. The incorporation of a Cu-atom on its turn is initiated by a change in conformation upon substrate contact at RT and the addition of thermal energy. A conclusion drawn for both porphyrins is:

*Upon adsorption of the  $D_{4h}$  gas phase conformation a temperature dependent precursor planar configuration exists, that alters its conformation to a  $D_{2h}$  saddled shape on Cu(110).*

Self-assembly at RT is not observed for free-base TM-TPP at any coverage. It is, however, possible to introduce a small degree of self-organisation by the gradual addition and release of thermal energy. In contrast pre-metallated TM-Co-TPP forms small chiral domains at RT. These domains are comprised of planar molecules that have their adsorption site on ad-islands generated by substrate interaction of mesityl groups that rotate and form different types of intermolecular  $\pi$ - $\pi$  bonds. Pheriperic interaction of molecules that diffused towards a domain can induce local conformational changes passed on by other molecules in the agglomeration. The global orientation is not modified. It is possible to transform these into domains of saddled molecules via regulated addition of thermal energy. Another general conclusion derived from the experiments is:

*Molecular translation on Cu(110) at temperatures between 298 and 500 K occurs via substrate surface ad-atom clusters that transport molecules while diffusing. This is steered by the bulk atoms and dependent on the surface roughness, molecular conformation and adsorption site.*

Can the conclusions presented above provide an answer to the following question? Interstellar connection? This question is twofold viz. the intermolecular bonds created at interstellar conditions, and the interstellar connection to life on Earth. There is no easy answer to this question. It is however possible to put forward the following hypothesis:

*Recently Sanders et al.<sup>[241]</sup> posed that different planetesimals and their meteorite fragments have recorded an overlapping series of events melting, collisions, accretion of nebula and interstellar material and hydrothermal action. Furthermore the smallest engines of creation,<sup>[242]</sup> RNA molecules, consist of a polymer (phosphate-ribose) backbone. Moreover cellulose is a polymer that consist solely of linked glucose molecules (polysacharide). Covalent connection (polymerisation) catalysed by a substrate at interstellar conditions could have emerged after heating of organic self-assembled or self-organised systems on a metal.*



## Appendix A.

### Saddled TM-TPP Orbital configuration

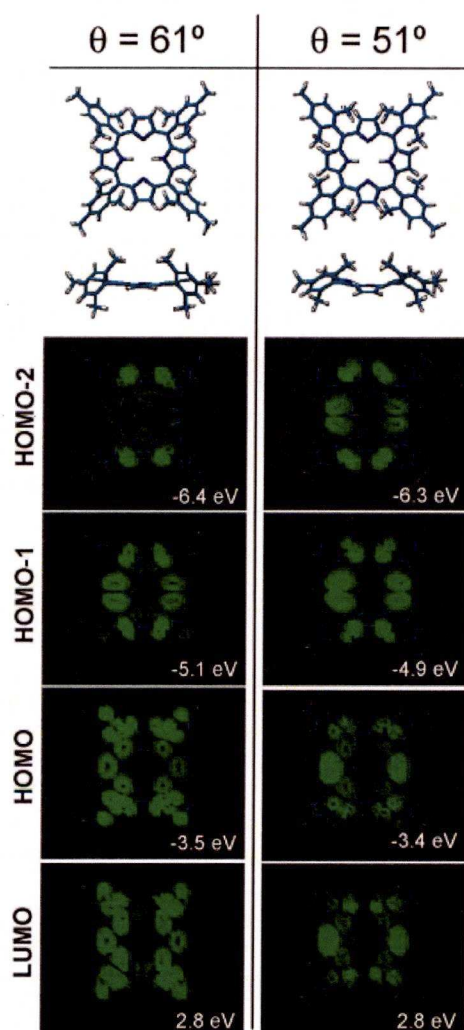


**Figure A.1.** – Molecular structure (top and side view), and calculated charge density contours and binding energy relative to the Fermi level for frontier orbitals measured at a height of 2 Å above the mean porphyrin plane. (Extended Hückel and *ab initio* methods)<sup>[181]</sup>

## Appendix B.

### Local coordinates skeletal modes of (metallo)porhyrins

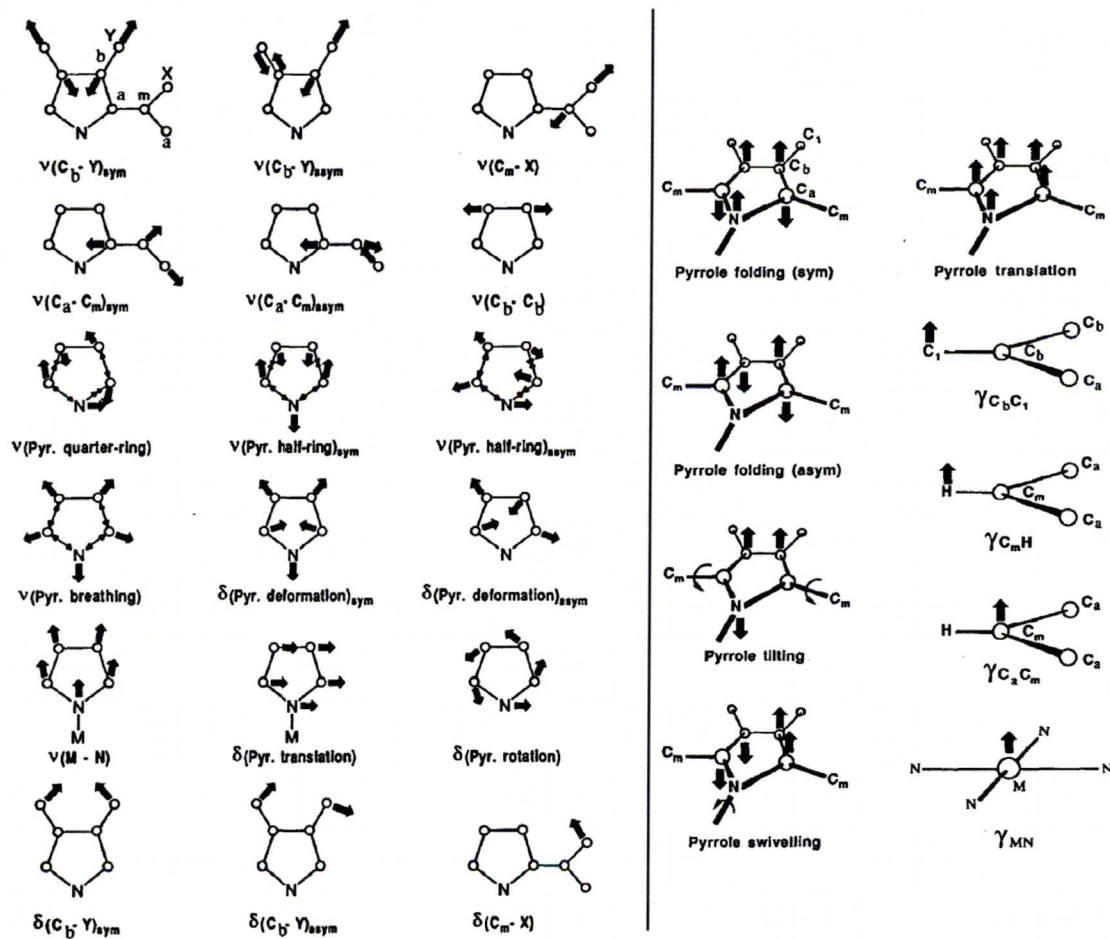


Figure B.1. – In-plane porphyrinic modes (left). Out-of-plane modes (right).<sup>[243]</sup>



# Appendix C.

## RAIRS mesitylene

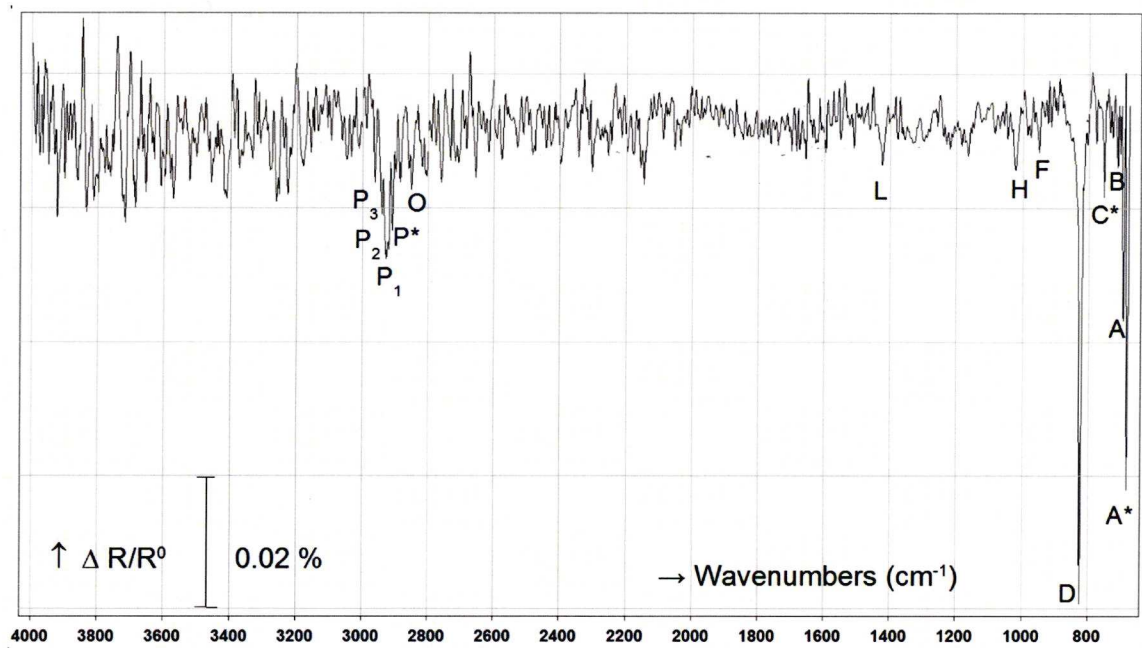


Figure C.1. – Low coverage spectrum of Mesitylene ( $D_{3h}$  Framework).

Table C.1a. – Low wavenumber region assignment of mesitylene<sup>[198]</sup>

Peak	A*	A	B	C*	D	F	H
$\bar{\nu} \text{ (cm}^{-1}\text{)}$	684	697	716	754	826	951	1020
$\frac{\Delta R}{R^0} \times 10^{-2}$	6	3	1	1	7	1	1
Assignment	$\chi$ ring ph	$\chi$ ring ph	ip ph	oop CH3	oop ph	ip/oop ph	CH <sub>3</sub> rock

Table C.1b. – Mid and High wavenumber region				
Peak	<i>L</i>	<i>O</i>	<i>P</i> *   <i>P</i> <sub>1</sub> / <i>P</i> <sub>2</sub>	<i>P</i> <sub>3</sub>
$\bar{\nu}$ (cm <sup>−1</sup> )	1424	2850/2859	2899-2941	2963
$\frac{\Delta R}{R^0} \times 10^{-2}$	1	2/2	var	2
Assignment	ip CH <sub>3</sub>	CH <sub>2</sub>	CH <sub>2</sub> / CH <sub>3</sub>	CH <sub>3</sub>

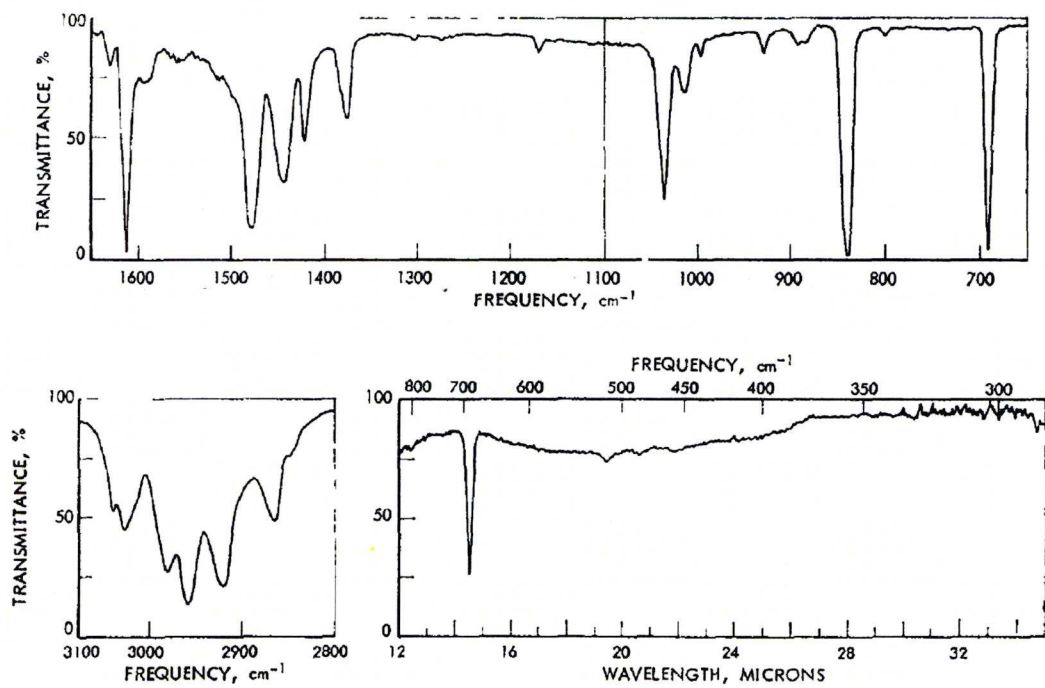


Figure C.2. – IR reference spectrum at 77K (crystal)<sup>[244]</sup>

Table C.2. – Various Phenyl IR vibrational shifts induced by addition of functional groups.

Compound <sup>[245]</sup>	Methyl groups	oop ph C-H b	ip C=C ph str
Benzene	0	674	1478
Phenol	0	752/810	1595
Toluene	1	729	1605
m-Xylene	2	769	1614
p-Xylene	2	795	1630
1,3,5-Mesitylene	3	837	1610
1,2,3,5-tetramethylbenzene	4	859	1615

## Appendix D.

LDI-TOF MS TM-TPP in positive  
mode



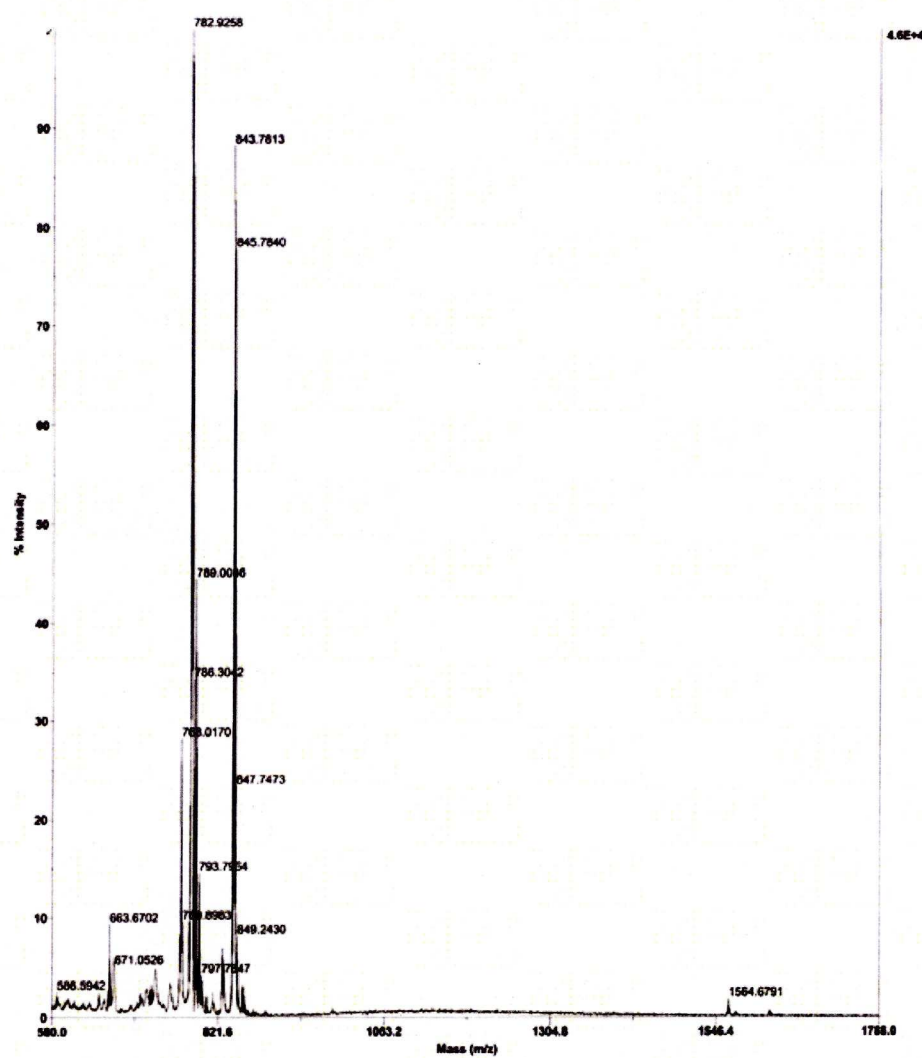
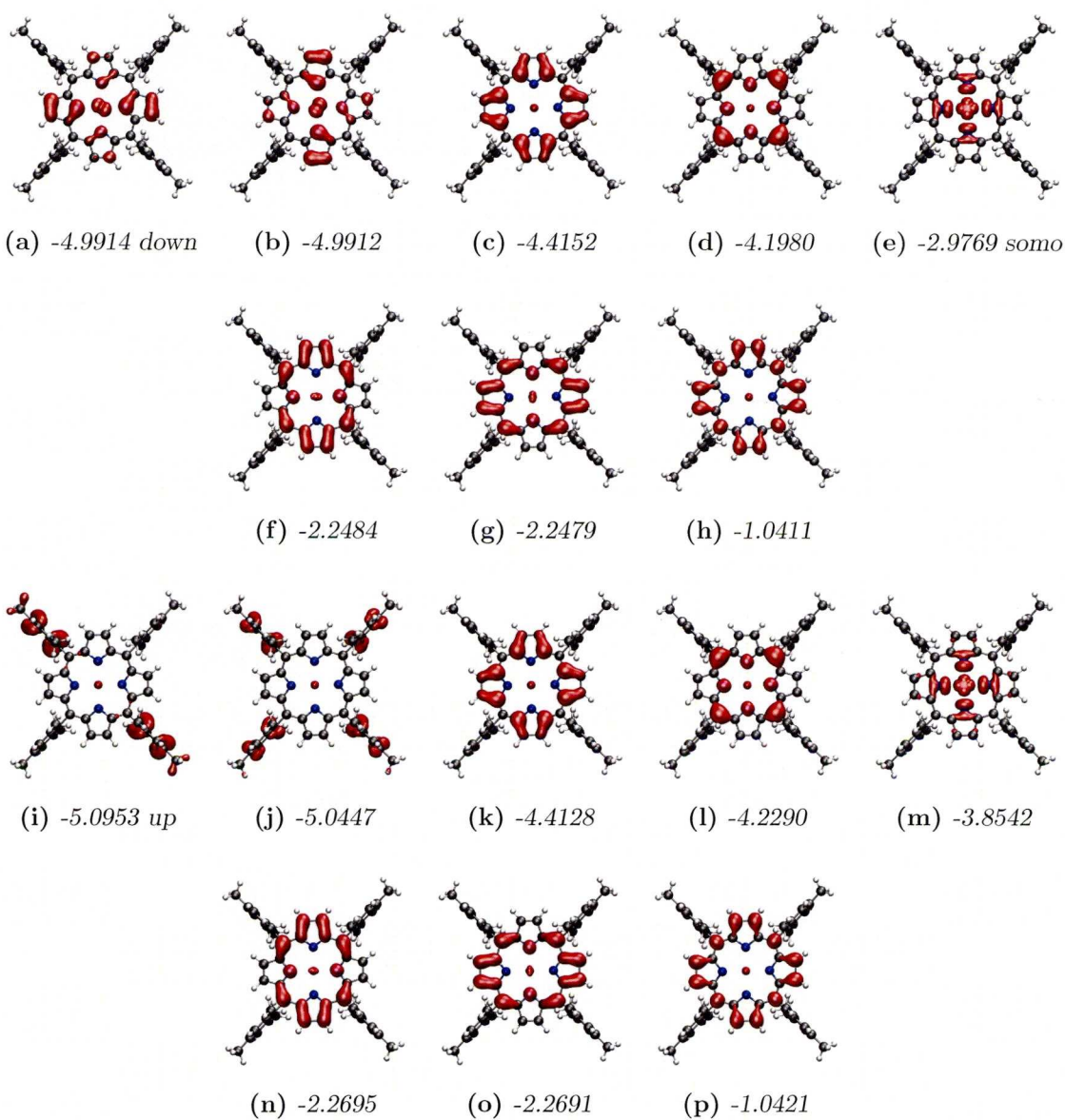


Figure D.1. – TM-TPP heated with a large excess of copper turnings at 353 K,  $C_{56}H_{54}N_4$  (783.05 au),  $C_{56}H_{52}CuN_4$  (844.58 au)<sup>[178]</sup>

## Appendix E.

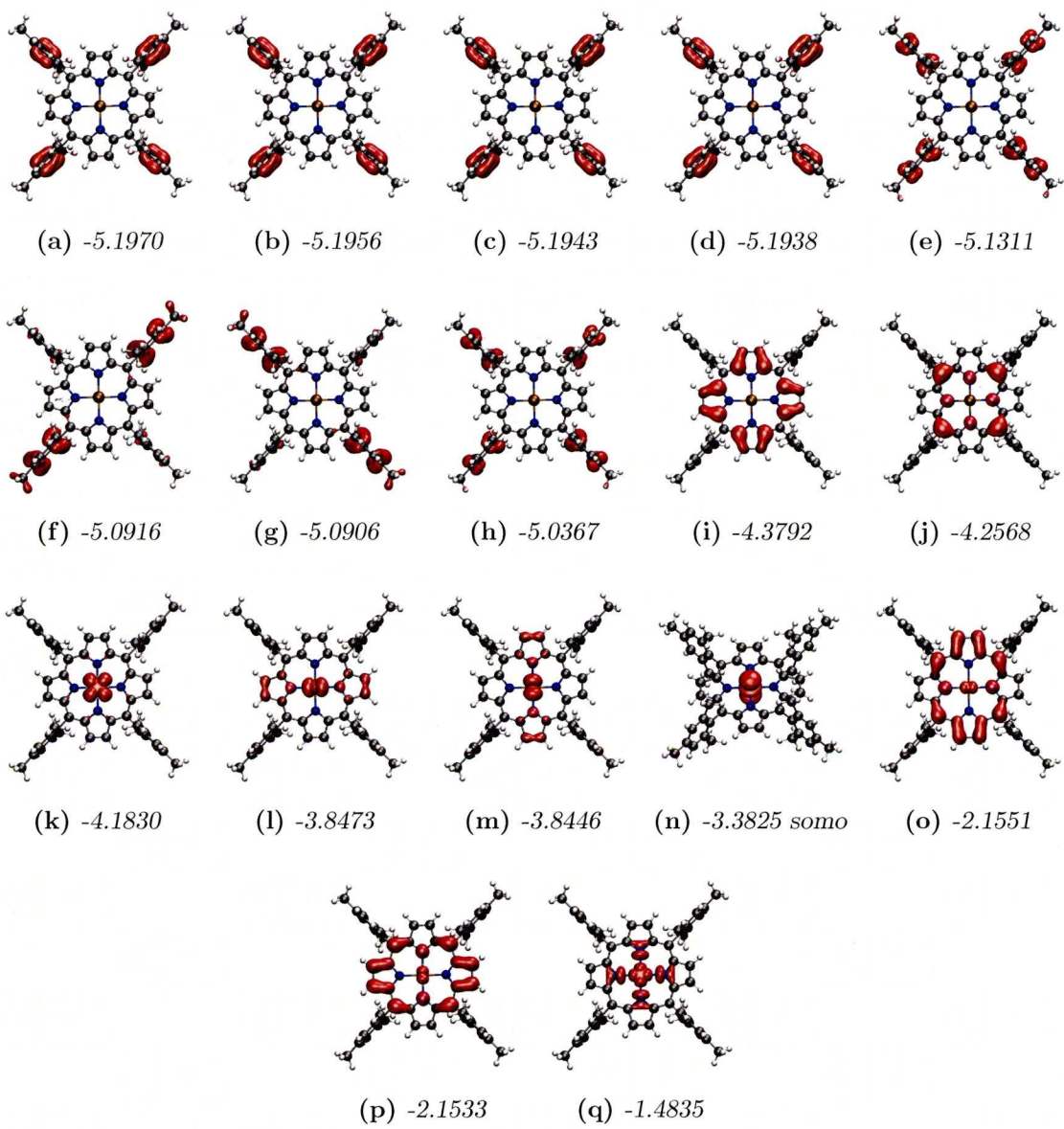
### VASP-DFT Molecular Orbitals TM-(Cu)-TPP





## **Appendix F.**

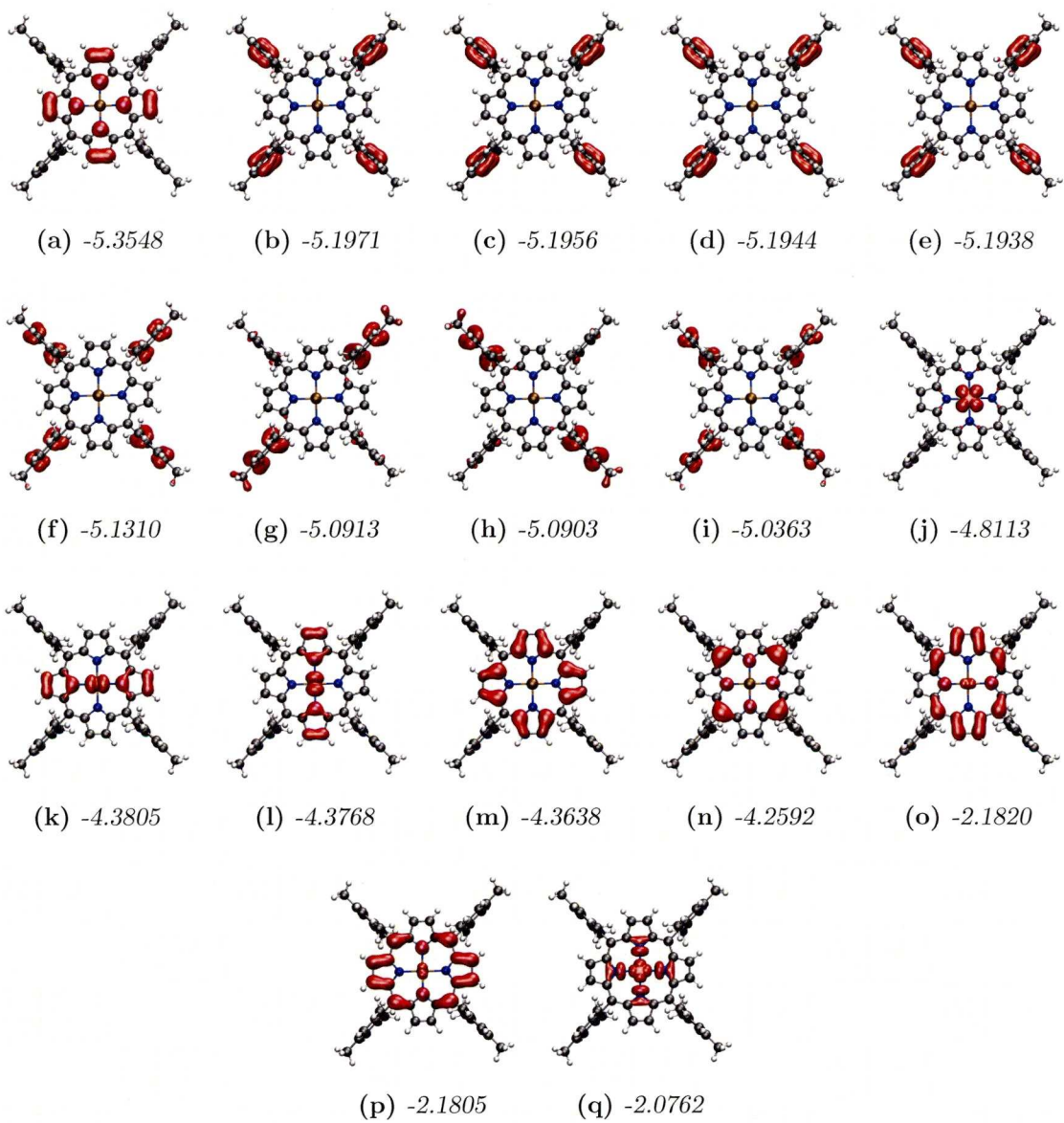
### **VASP-DFT Molecular Orbitals TM-(Co)-TPP minority spins**



## **Appendix G.**

**VASP-DFT Molecular Orbitals  
TM-(Co)-TPP majority spins**





# Bibliography

- [1] G. Somorjai, *Chem. Rev.* **96**, 1223 (1996).
- [2] W. Goddard, D. Brenner, S. Lyshevski, G. Lafrate, *Handbook of Nanoscience, Engineering and Technology* (CRC Press, 2007).
- [3] K. Kolasinski, *Surface Science -Foundations of Catalysis and Nanoscience* (John Wiley & Sons, LTD, 2002).
- [4] S. Barlow, R. Raval, *Surf. Sci. Rep.* **50**, 201 (2003).
- [5] P. Thaddeus, *Phil. Trans. R. Soc. B* **361**, 1681 (2006).
- [6] P. Ehrenfreund, *Oratie* (2003).
- [7] A. Battersby, *Nat. Prod. Rep.* **17**, 507 (2000).
- [8] A. Tohara, M. Sato, *Chem. Pharm. Bull* **56**, 1041 (2008).
- [9] P. Pelletier, J. Caventou, *Ann. Chim. et Phys.* **9**, 194 (1818).
- [10] G. Mulder, *J. Prakt. Chem* **33**, 478 (1844).
- [11] M. Nencki, *Ber. Deut. Chem. Ges.* **29**, 2877 (1896).
- [12] W. Küster, *Z. Physiol. Chem.* **82**, 463 (1913).
- [13] H. Fischer, H. Wenderoth, *Annalen der Chemie* **537**, 171 (1939).
- [14] H. Fischer, B. Walach, *Liebig's Annalen der Chemie* **450**, 164 (1926).
- [15] J.-H. Chou, M. Kosal, H. S. Nalwa, N. Rakow, K. Suslick, *The Porphyrin Handbook* **6**, 43 (2000).
- [16] E. Hao, Syntheses and evaluation of porphyrin derivatives for applications in medicine and in material science, Ph.D. thesis, Louisiana State University -Agricultural and Mechanical College (2007).
- [17] J. Reimers, N. Hush, M. Crossley, *J. Porphyrins Phthalocyanines* **6**, 795 (2002).
- [18] T. A. Jung, R. R. Schlittler, J. K. Gimzewski, H. Tang, C. Joachim, *Science* **271**, 181 (1996).
- [19] V. Langlais, *et al.*, *Phys. Rev. Lett.* **83**, 2809 (1999).
- [20] T. Jung, R. Schittler, J. Gimzewski, *Nature* **386**, 696 (1997).
- [21] J. Gimzewski, T. Jung, M. Cuberes, R. Schlittler, *Surf. Sci.* **386**, 101 (1997).

- [22] D. Fujita, *et al.*, *Surf. Sci.* **454-456**, 1021 (2000).
- [23] T. Kamikado, T. Sekiguchi, S. Yokoyama, Y. Wakayama, S. Mashiko, *Thin Solid Films* **499**, 329 (2006).
- [24] T. Terui, *et al.*, *Thin Solid Films* **499**, 157 (2006).
- [25] T. Sekiguchi, Y. Wakayama, S. Yokoyama, T. Kamikado, S. Mashiko, *Thin Solid Films* **464-465**, 393 (2004).
- [26] T. Terui, T. Kamikado, Y. Okuno, H. Suzuki, S. Mashiko, *Current Applied Physics* **4**, 148 (2004).
- [27] T. Terui, T. Sekiguchi, Y. Wakayama, T. Kamikado, S. Mashiko, *Thin Solid Films* **464-465**, 384 (2004).
- [28] T. Yokoyama, T. Kamikado, S. Yokoyama, S. Mashiko, *J. Chem. Phys.* **121**, 11993 (2004).
- [29] Y. Okuno, T. Terui, S. Tanaka, T. Kamikado, S. Mashiko, *Journal of Molecular Structure (Theochem)* **676**, 141 (2004).
- [30] H. Suzuki, H. Miki, S. Yokoyama, S. Mashiko, *J. Phys. Chem. B* **107**, 3659 (2003).
- [31] W. Deng, *et al.*, *J. Chem. Phys.* **117**, 4995 (2002).
- [32] Y. Okuno, T. Kamikado, S. Yokoyama, S. Mashiko, *Journal of Molecular Structure (Theochem)* **594**, 55 (2002).
- [33] T. Yokoyama, S. Yokoyama, T. Kamikado, S. Mashiko, *J. Chem. Phys.* **115**, 3814 (2001).
- [34] T. Yokoyama, S. Yokoyama, T. Kamikado, Y. Okuno, S. Mashiko, *Nature* **413**, 619 (2001).
- [35] Z.-C. Dong, *et al.*, *Jpn. J. Appl. Phys.* **41**, 4898 (2002).
- [36] Z.-C. Dong, *et al.*, *Thin Solid Films* **438-439**, 262 (2003).
- [37] H. Suzuki, *et al.*, *Thin Solid Films* **393**, 325 (2001).
- [38] F. Moresco, *Physics Reports* **399**, 175 (2004).
- [39] F. Moresco, G. Meyer, H. Tang, C. Joachim, K. Rieder, *J. Electron Spectrosc. Relat. Phenom.* **129**, 149 (2003).
- [40] F. Moresco, *et al.*, *Surf. Sci.* **499**, 94 (2002).
- [41] F. Moresco, *et al.*, *Phys. Rev. Lett.* **86**, 672 (2001).
- [42] F. Moresco, *et al.*, *Phys. Rev. Lett.* **87**, 088302 (2001).
- [43] F. Moresco, *et al.*, *Appl. Phys. Lett.* **78**, 306 (2001).
- [44] W. Deng, K. Hipps, *J. Phys. Chem. B* **107**, 10736 (2003).
- [45] L. Scudiero, D. Barlow, U. Mazur, K. Hipps, *J. Am. Chem. Soc.* **123**, 4073 (2001).



- [46] L. Scudiero, D. Barlow, K. Hipps, *J. Phys. Chem. B* **104**, 11899 (2000).
- [47] V. Smith, Ph.D. thesis, The University of Liverpool -Surface Science Research Centre (2007).
- [48] P. Donovan, A. Robin, M. Dyer, M. Persson, R. Raval (2009).
- [49] A. Weber-Bargioni, *et al.*, *ChemPhysChem* **9**, 89 (2008).
- [50] X. Lu, K. Hipps, X. Wang, U. Mazur, *J. Am. Chem. Soc.* **118**, 7197 (1996).
- [51] D. Jones, A. Hinman, *J. Chem. Soc. Dalton Trans.* pp. 1503–1509 (1992).
- [52] P. Sautet, C. Joachim, *Surf. Sci.* **271**, 387 (1992).
- [53] H. Yanagi, M. Ashida, Y. Harima, K. Yamashita, *Chem. Lett.* pp. 385–388 (1990).
- [54] P. Lippel, R. Wilson, M. Miller, C. Wöll, S. Chiang, *Phys. Rev. Lett.* **62**, 171 (1989).
- [55] D. Barlow, L. Scudiero, K. Hipps, *Langmuir* **20**, 4413 (2004).
- [56] L. Scudiero, K. Hipps, D. Barlow, *J. Phys. Chem. B* **107**, 2903 (2003).
- [57] T. Shubina, *et al.*, *J. Am. Chem. Soc.* **129**, 9476 (2007).
- [58] F. Buchner, V. Schwald, K. Comanici, H.-P. Steinrück, H. Marbach, *ChemPhysChem* **8**, 241 (2007).
- [59] F. Buchner, *et al.*, *J. Phys. Chem. C* **112**, 15458 (2008).
- [60] W. Auwärter, *et al.*, *J. Am. Chem. Soc.* **129**, 11279 (2007).
- [61] X. Guo, Z. Dong, D. Fujita, *Thin Solid Films* **516**, 2407 (2008).
- [62] L. Grill, *et al.*, *Nature Nanotechnology -Supplementary Information* **2**, S1 (2007).
- [63] D. Bonifazi, *et al.*, *Adv. Funct. Mater.* **37**, 1051 (2007).
- [64] K. Rim, *et al.*, *Angew. Chem. Int. Ed.* **46**, 7891 (2007).
- [65] M. Hodgson, Preparation, structure and spectra of meso-metalloporphyrins, Ph.D. thesis, Queensland University of Technology -School of Physical and Chemical Sciences (2005).
- [66] M. Gouterman, *The Journal of Chemical Physics* **30**, 1139 (1959).
- [67] T. Hashimoto, Y.-K. Choe, H. Nakano, K. Hirao, *J. Phys. Chem. A* **103**, 1894 (1999).
- [68] P. Atkins, J. de Paula, *Physical Chemistry* (Oxford University Press, 2002), 7th edn.
- [69] L. Jiao, Synthesis and functionalizations of tetrapyrrole derivatives, Ph.D. thesis, Louisiana State University -Agricultural and Mechanical College (2007).
- [70] E. Baerends, G. Ricciardi, A. Rosa, S. van Gisbergen, *Coord. Chem. Rev.* **230**, 5 (2002).
- [71] M.-S. Liao, S. Scheiner, *J. Chem. Phys.* **117**, 205 (2002).
- [72] M. Dyer, M. Persson, Personal communication.

- [73] M.-S. Liao, P. Bonifassi, J. Leszczynski, M.-J. Huang, *Mol. Phys.* **106**, 147 (2008).
- [74] P. Hambright, *Coordination Chemistry Reviews* **6**, 247 (1971).
- [75] B. Erler, W. Scholz, Y. J. Lee, W. Scheidt, C. Reed, *J. Am. Chem. Soc.* **109**, 2644 (1987).
- [76] H. Song, C. Reed, W. Scheidt, *J. Am. Chem. Soc.* **111**, 6865 (1989).
- [77] D. Nurco, C. Medforth, T. Forsyth, M. Olmstead, K. Smith, *J. Am. Chem. Soc.* **118**, 10918 (1996).
- [78] W. Jentzen, *et al.*, *J. Am. Chem. Soc.* **117**, 11085 (1995).
- [79] W. Jentzen, X.-Z. Song, J. Shelnutt, *J. Phys. Chem. B* **101**, 1684 (1997).
- [80] W. Jentzen, I. Tutowska-Tyrk, W. Scheidt, J. Shelnutt, *Inorg. Chem.* **35**, 3559 (1996).
- [81] W. Jentzen, *et al.*, *J. Phys. Chem. A* **101**, 5789 (1997).
- [82] J. Shelnutt, *J. Porphyrins Phthalocyanines* **5**, 300 (2001).
- [83] X.-Z. Song, *et al.*, *J. Am. Chem. Soc.* **118**, 12975 (1996).
- [84] L. Sparks, *et al.*, *J. Am. Chem. Soc.* **115**, 581 (1993).
- [85] Y.-H. Zhang, W.-J. Ruan, Z.-Y. Li, Y. Wu, J.-Y. Zheng, *Chem. Phys.* **315**, 201 (2005).
- [86] J. Hill, *et al.*, *Chem. Comm* pp. 2320–2322 (2006).
- [87] J. Hill, Y. Wakayama, K. Ariga, *PCCP* **8**, 5034 (2006).
- [88] B. Cheng, O. Munro, H. Marques, W. Scheidt, *J. Am. Chem. Soc.* **119**, 10732 (1997).
- [89] A. Rosa, G. Ricciardi, E.-J. Baerends, *J. Phys. Chem. A* **110**, 5180 (2006).
- [90] J. Shao, E. Steene, B. Hoffman, A. Ghosh, *Eur. J. Inorg. Chem* pp. 1609–1615 (2005).
- [91] M. Faraday, *Experimental Researches in electricity* (J.M. Dent&Sons LTD, 1922).
- [92] D. McQuarrie, J. Simon, *Physical Chemistry, A molecular Approach* (University Science Books, 1997).
- [93] I. Langmuir, *The Journal of the American Chemical Society* **38**, 2221 (1916).
- [94] I. Langmuir, *Physical Review* **8**, 149 (1916).
- [95] I. Langmuir, *The Journal of the American Chemical Society* **40**, 1361 (1918).
- [96] S. Brunauer, P. Emmett, E. Teller, *J. Am. Chem. Soc.* **60**, 309 (1938).
- [97] R. Feynman, *Journal of microelectrochemical systems* **1**, 60 (1992).
- [98] G. Kellogg, *Surface Science Reports* **21**, 1 (1994).
- [99] Y. Shirai, *et al.*, *J. Am. Chem. Soc.* pp. 4854–4864 (2006).
- [100] D. Eigler, E. Schweizer, *Nature* **344**, 524 (1990).

- [101] J. Gimzewski, C. Joachim, *Science* **283**, 1683 (1999).
- [102] I. Langmuir, *J. Am. Chem. Soc.* **37**, 1139 (1915).
- [103] J. L. Jones, *Transactions of the Faraday Society* **28**, 333 (1932).
- [104] G. Ertl, *Langmuir* **3**, 4 (1987).
- [105] E. Zaremba, W. Kohn, *Physical Review B* **13**, 2270 (1976).
- [106] B. Dodson, *Phys. Rev. Lett.* **60**, 2288 (1988).
- [107] W. Burton, N. Cabrera, F. Frank, *Philosophical Transactions of the Royal Society of London. Series A, Mathematical and Physical Sciences* **243**, 40 (1950).
- [108] W. van Enkevort, *Fundamenten van de Kristalgroei: Een inleiding* (Radboud University Nijmegen, 1996).
- [109] A. Einstein, *Annalen der Physik* **19**, 371 (1906).
- [110] G. A. L. Barnes, *Surfaces* (Oxford Science Publications, 2004), fourth edn.
- [111] L. Barbosa, P. Sautet, *J. Am. Chem. Soc.* **123**, 6639 (2001).
- [112] D. Adams, *Surf. Sci.* **42**, 12 (1974).
- [113] L. Österlund, M. Ø. Pedersen, I. Stensgaard, E. Lægsgaard, F. Besenbacher, *Phys. Rev. Lett.* **83**, 4812 (1999).
- [114] S. Brunauer, L. Deming, W. Deming, E. Teller, *J. Am. Chem. Soc.* **62**, 1732 (1940).
- [115] J. Tully, G. Gilmer, M. Shugard, *J. Chem. Phys.* **71**, 1630 (1979).
- [116] S. Allen, G. McKayb, J. Porter, *J. Colloid Interface Sci.* **280**, 322 (2004).
- [117] A. Smith, S. Aranoff, *Journal of Physical Chemistry* **62**, 684 (1958).
- [118] G. Ehrlich, *J. Appl. Phys.* **32**, 4 (1961).
- [119] P. Redhead, *Vacuum* **12**, 203 (1962).
- [120] J. Falconer, R. Madix, *Surf. Sci.* **48**, 393 (1975).
- [121] F. Besenbacher, *Rep. Prog. Phys.* **59**, 1737 (1996).
- [122] C. Chen, *Introduction to Scanning Tunneling Microscopy* (Oxford University Press, 2008), second edn.
- [123] K. Hipps, *Scanning Tunneling Spectroscopy* (Springer Verlag, 2006).
- [124] D. Skoog, D. West, F. Holler, *Fundamentals of Analytical Chemistry* (Saunders College Publishing, 1996), 7th edn.
- [125] W. Heisenberg, *Zeitschrift für Physik A: Hadrons and Nuclei* **43**, 127 (1927).
- [126] D. Shriver, P. Atkins, C. Langford, *Inorganic Chemistry* (Oxford University Press, 1996), second edn.



- [127] J. Simmons, *J. Appl. Phys.* **34**, 1793 (1963).
- [128] R. Young, J. Ward, F. Scire, *Rev. Sci. Instrum.* **43**, 999 (1972).
- [129] R. Young, *Rev. Sci. Instrum.* **37**, 275 (1966).
- [130] H. Bourque, R. Leblanc, *Rev. Sci. Instrum.* **66**, 2695 (1995).
- [131] B. Rogers, J. Shapter, W. Skinner, K. Gascoigne, *Rev. Sci. Instrum.* **4**, 1702 (2000).
- [132] M. Watanabe, T. Kinno, *Appl. Surf. Sci.* **76/77**, 353 (1994).
- [133] H. Mamin, P. Guethner, D. Rugar, *Phys. Rev. Lett.* **19**, 2418 (1990).
- [134] G. Binnig, H. Rohrer, C. Gerber, E. Weibel, *Appl. Phys. Lett.* **40**, 178 (1981).
- [135] G. Binnig, H. Rohrer, *IBM Journal of Research and Development* **44**, 279 (2000).
- [136] G. Binnig, H. Rohrer, C. Gerber, E. Weibel, *Physica* **109 & 110B**, 2075 (1982).
- [137] G. Binnig, H. Rohrer, C. Gerber, E. Weibel, *Phys. Rev. Lett.* **49**, 57 (1982).
- [138] G. Binnig, H. Rohrer, C. Gerber, E. Weibel, *Phys. Rev. Lett.* **50**, 120 (1983).
- [139] P. Geng, *et al.*, *Rev. Sci. Instrum.* **71**, 504 (2000).
- [140] S. Ernst, S. Wirth, M. Rams, V. Dolocan, F. Steglich, *Science and Technology of Advanced Materials* **8**, 347 (2007).
- [141] G. Binnig, D. Smith, *Rev. Sci. Instrum.* **57**, 1688 (1986).
- [142] F. Besenbacher, E. Lægsgaard, K. Mortensen, U. Nielsen, I. Stensgaard, *Rev. Sci. Instrum.* **59**, 7 (1988).
- [143] Scanning tunneling microscope stm 150 aarhus technical data, *Tech. rep.*, SPECS GmbH, Surface Analysis and Computer Technology.
- [144] Specs 150 aarhus stm, produkt-info-05-2005, *Tech. rep.*.
- [145] F. Besenbacher, E. Lægsgaard, I. Stensgaard, *Microscopy and Analysis* **17** (1989).
- [146] T. Galante, *et al.*, *Journal of Intelligent Material Systems and Structures* **10**, 962 (1990).
- [147] F. Herschel, *Philosophical Transactions of the Royal Society of London* **90**, 284 (1800).
- [148] W. Coblentz, *The American Physical Society* **6**, 385 (1903).
- [149] W. Coblentz, *The Physical Review* **23**, 125 (1906).
- [150] W. Coblentz, *The Physical Review* **20**, 273 (1905).
- [151] E. Merritt, *The Physical Review* **2**, 424 (1895).
- [152] W. Heitler, G. Herzberg, *Zeitschrift für Physik A Hadrons and Nuclei* **53**, 52 (1929).
- [153] G. Herzberg, F. Patat, H. Verleger, *Journal of Physical Chemistry* **41**, 123 (1936).

- [154] R. Eischens, S. Francis, W. Pliskin, *Journal of Physical Chemistry* **60**, 194 (1956).
- [155] H. Pickering, H. Eckstrom, *Journal of Physical Chemistry* **63**, 512 (1959).
- [156] R. Greenler, *The Journal of Chemical Physics* **44**, 310 (1966).
- [157] R. Greenler, *The Journal of Chemical Physics* **50**, 1966 (1969).
- [158] J. McIntyre, D. Aspnes, *Surf. Sci.* **24**, 417 (1971).
- [159] S. A. Francis, A. H. Ellison, *J. Opt. Soc. Am.* **49**, 131 (1959).
- [160] R. Raval, *Surf. Sci.* **331-333**, 1 (1995).
- [161] J. Yates, R. Greenler, I. Ratajczykowa, D. King, *Surf. Sci.* **36**, 739 (1973).
- [162] R. Greenler, *J. Vac. Sci. Technol.* **12**, 1410 (1975).
- [163] Y. Chabal, *Surf. Sci. Rep.* **8**, 211 (1988).
- [164] P. Hollins, *Vacuum* **45**, 705 (1994).
- [165] P. Hollins, J. Pritchard, *Prog. Surf. Sci.* **19**, 275 (1985).
- [166] M. Chesters, *J. Mol. Struct.* **173**, 405 (1988).
- [167] M. Trenary, *Annu. Rev. Phys. Chem.* **51**, 381 (2000).
- [168] R. Raval, M. Harrison, D. King, *J. Vac. Sci. Technol. A* **9**, 345 (1991).
- [169] F. Hoffmann, *Surf. Sci. Rep.* **3**, 107 (1983).
- [170] E. Herceg, H. Celio, M. Trenary, *Rev. Sci. Instrum.* **75**, 2545 (2004).
- [171] H. Jenniskens, *et al.*, *Meas. Sci. Technol.* **8**, 1313 (1997).
- [172] M. Planck, *Annalen der Physik* **3**, 553 (1901).
- [173] M. Chesters, *J. Electron Spectrosc. Relat. Phenom.* **38**, 123 (1986).
- [174] R. Silverstein, F. X. Webster, *Spectrometric Identification of Organic Compounds* (John Wiley & Sons, Inc, 1998).
- [175] V. Harsch, *Aviation, Space, and Environmental Medicine* **78**, 1075 (2007).
- [176] N. Harris, *Modern Vacuum Practice* (McGraw-Hill, 1989).
- [177] *VT-SPM User's Guide, M110202 VT SPM Version 1.7.*
- [178] P. Iavicoli, D. Amabilino, Experiments carried out at icmab, barcelona.
- [179] P. S. S. Bermudez, Adsorption of complex organic molecules on metal single crystal surfaces, Ph.D. thesis, University of Liverpool (2005).
- [180] M. Thompson, Arguslab 4.0, Planaria Software LLC, Seattle, WA (2003).
- [181] D. Écija, *et al.*, *J. Phys. Chem. C* **112**, 8988 (2008).

- [182] J. Repp, G. Meyer, *Phys. Rev. Lett.* **94**, 026803 (2005).
- [183] P. Liljeroth, J. Repp, G. Meyer, *Science* **317**, 1203 (2007).
- [184] T. Rush, *et al.*, *J. Phys. Chem. B* **104**, 5020 (2000).
- [185] J. Alben, S. Choi, A. Adler, W. Caughey, *Annals New York Academy of Sciences* p. 278.
- [186] L. Krim, S. Sorgues, B. Soep, N. Shafizadeh, *J. Phys. Chem. A* **109**, 8268 (2005).
- [187] P. Kozlowski, *et al.*, *J. Phys. Chem. A* **103**, 1357 (1999).
- [188] A. Rosa, G. Ricciardi, E. Bearends, A. Romeo, L. M. Scolaro, *J. Phys. Chem. A* **107**, 11468 (2003).
- [189] A. Ghosh, *J. Phys. Chem. B* **101**, 3290 (1997).
- [190] M. in 't Veld, S. Haq, R. Raval, To be published.
- [191] E. Ferguson, I. Chang, *The Journal of Chemical Physics* **2**, 628 (1961).
- [192] J. Fajer, *J. Porphyrins Phthalocyanines* **4**, 382 (2000).
- [193] D. Futaba, S. Chiang, *Surf. Sci.* **448**, L175 (2000).
- [194] J. Lee, D. Dougherty, J. Yates, *The Journal of Physical Chemistry B* **110**, 15645 (2006).
- [195] J. Gaudioso, L. Lauhon, W. Ho, *Phys. Rev. Lett.* **85**, 1918 (2000).
- [196] W. Ho, *J. Chem. Phys.* **24**, 11033 (2002).
- [197] J. Lee, D. Dougherty, J. Yates, *J. Am. Chem. Soc.* **126**, 6008 (2006).
- [198] B. V. Lokshin, V. T. Aleksanyan, M. G. Ezernitskaya, *Russian Chemical Bulletin* **31**, 1995 (1982).
- [199] T. Beebe, J. Yates, *J. Phys. Chem.* **91**, 254 (1987).
- [200] E. Hommel, H. Allen, *Analyst* **128**, 750 (2003).
- [201] I. L. Tocón, M. Woolley, J. Otero, J. Marcos, *J. Mol. Struct.* **470**, 241 (1998).
- [202] R. Raval, M. Chesters, *Surface Science Letters* **219**, L505 (1989).
- [203] R. Raval, S. F. Parker, M. A. Chesters, *Surface Science* **289**, 227 (1993).
- [204] F. Moresco, *et al.*, *Appl. Phys. A* **80**, 913 (2005).
- [205] L. Gross, *et al.*, *Chemical Physics Letters* **371**, 750 (2003).
- [206] I. Stensgaard, F. Besenbacher, F. Jensen, E. Lægsgaard, L. Ruan, *Physica Scripta* **T39**, 314 (1991).
- [207] S. Titmuss, A. Wander, D. King, *Chem. Rev.* **96**, 1291 (1996).
- [208] F. Rosei, *et al.*, *Science* **296**, 328 (2002).



- [209] M. Schunack, *et al.*, *Physical Review Letters* **86**, 456 (2001).
- [210] T. Yokoyama, Y. Tomita, *The Journal of Chemical Physics* **129**, 164704 (2008).
- [211] L. Gross, *et al.*, *Nat. Mater.* **4**, 892 (2005).
- [212] J. Repp, G. Meyer, K.-H. Rieder, P. Hyldgaard, *Physical Review Letters* **91**, 206102 (2003).
- [213] G. Nazin, X. Qiu, W. Ho, *Science* **302**, 77 (2003).
- [214] C. Hirjibehedin, C. Lutz, A. Heinrich, *Science* **312**, 1021 (2006).
- [215] J. Gottfried, K. Flechtner, A. Kretschmann, T. Lukasczyk, H.-P. Steinrück, *J. Am. Chem. Soc.* **128**, 5644 (2006).
- [216] M. in 't Veld, P. Iavicoli, S. Haq, D. Amabilino, R. Raval, *Chem. Comm.* p. 1536–1538 (2008).
- [217] P. Kozłowski, J. Bingham, A. Jarzecki, *The Journal of Physical Chemistry A* **112**, 12781 (2008).
- [218] L. Grill, *et al.*, *Nature Nanotechnology* **2**, 687 (2007).
- [219] A. Egorov, S. Matyukhova, A. Anisimov, *Int. J. Chem. Kinet.* **37**, 296 (2005).
- [220] T. G. Solomons, *Solomons, Organic Chemistry* (John Wiley & Sons, Inc, 1996).
- [221] L. Österlund, *et al.*, *Phys. Rev. Lett.* **86**, 460 (2001).
- [222] J. Halley, D. Winkler, *Complexity* **14**, 10 (2008).
- [223] T. Dargel, R. Hertwig, W. Koch, *Molecular Physics* **96**, 583 (1999).
- [224] H.-B. Yi, H. M. Lee, K. S. Kim, *Journal of Chemical Theory and Computation* (2009).
- [225] S.-W. Hla, *J. Vac. Sci. Technol. B* **23**, 1351 (2005).
- [226] A. Rosa, E. J. Baerends, *Inorganic Chemistry* **33**, 584 (1994).
- [227] N. Bobrov, A. Davydov, N. Maksimov, K. Ione, V. Anufrienko, *Translated from Izvestiya Akademii Nauk SSSR* **4**, 748 (1975).
- [228] V. Humblot, M. O. Lorenzo, C. Baddeley, S. Haq, R. Raval, *J.A.C.S.* **126**, 6460 (2004).
- [229] T. Wadayama, H. Osano, H. Yoshida, S. Oda, N. Todoroki, *Applied Surf. Sci.* **254**, 5380 (2008).
- [230] K. P. de Jong, J. W. Geus, J. Joziassse, *Applications of Surface Science* **6**, 273 (1980).
- [231] S. Capozziello, A. Lattanzi, *Astrophysics and Space Science* **301**, 189 (2006).
- [232] V. Iancu, A. Deshpande, S.-W. Hla, *Nanoletters* **6**, 820 (2006).
- [233] H. Karacuban, *et al.*, *Surface Science* (2009).

- [234] M. Bischoff, Chemical identification in scanning tunneling microscopy by detection of element-specific localized surface states, Ph.D. thesis, Katholieke Universiteit Nijmegen (2002).
- [235] S. Fölsch, P. Hyldgaard, R. Koch, K. Ploog, *Physical Review Letters* **92**, 056803 (2004).
- [236] F. Olsson, *et al.*, *PRL* **93**, 206803 (2004).
- [237] F. Buchner, *et al.*, *The Journal of Physical Chemistry C* pp. – (2009).
- [238] I. Horcas, *et al.*, *Rev. Sci. Instrum.* **78**, 013705 (2007).
- [239] J. Elsila, D. Glavin, J. Dworkin, *Meteoritics and Planetary Science* **10-16**, 1323 (2009).
- [240] R. Stern, M. Jedrzejewski, *Chemical Reviews* **108**, 5061 (2008).
- [241] J. Bridges, J. Gilmore, I. Sanders, *A&G* **49**, 1.28 (2008).
- [242] K. Drexler, *Engines of creation 2.0 -the coming era of nanotechnology* (2006).
- [243] A. Procyk, D. Bocian, *Annu. Rev. Phys. Chem.* **43**, 465 (1992).
- [244] C. L. Lau, R. Snyder, *Spectrochimica Acta* **27A**, 2073 (1971).
- [245] T. Saito, *et al.*, Sdbweb: Spectral database for organic compounds (national institute of advanced industrial science and technology, japan), [riodb01.ibase.aist.go.jp/sdbs/](http://riodb01.ibase.aist.go.jp/sdbs/).
- [246] A. Buckley, *Hepthesis v1.4* (2007).
- [247] W. van Hirtum, *Latex voor beginners -deel 1 t/m 3* (2007).

# Colophon

This thesis was made in  $\text{\LaTeX} 2_{\epsilon}$   $\text{\BIBTeX}$  using the ‘hepthesis’ class.<sup>[246,247]</sup>, bibliography manager: JabRef v2.5 and Text Editor: WinEdt v5.5

© Mendel G.E. in 't Veld, 2010